To the Graduate Council:

I am submitting herewith a dissertation written by Mikhail Batygov entitled "Combined Study of Reactor and Terrestrial Antineutrinos with KamLAND". I have examined the final electronic copy of this dissertation for form and content and recommend that it be accepted in partial fulfillment of the requirements for the degree of Doctor of Philosophy, with a major in Physics.

Yuri Kamyshkov
Major Professor

We have read this dissertation
and recommend its acceptance:

William Bugg

Robert Compton

George Siopsis

Accepted for the Council:

Linda Painter
Interim Dean of Graduate Studies

(Original signatures are on file with official student records)

Combined Study of Reactor and Terrestrial Antineutrinos with KamLAND

A Dissertation
Presented for the
Doctor of Philosophy
Degree
The University of Tennessee, Knoxville

Mikhail Batygov
December 2006

Copyright © 2006 by Mikhail Batygov
All rights reserved.

Dedication

This dissertation is dedicated to my mother, Iraida Petrovna Vishnevskaya, and my father, Sergey Khachaturovih Batygov, who have always supported and encouraged me to stand up to the challenges of life.

Acknowledgements

This study is the result of the efforts of the whole KamLAND collaboration. I would like to thank every KamLAND collaborator for the contribution to the operation of the experiment which made the work presented here possible.

KamLAND is supported by the Center of Excellence program of the Japanese Ministry of Education, Culture, Sports, Science and Technology under grant 09CE2003, and by the United States Department of Energy under grant DE-FG02-91ER40627. The reactor data is provided courtesy of the following electric associations in Japan: Hokkaido, Tohoku, Tokyo, Hokuriku, Chubu, Kansai, Chugoku, Shikoku, and Kyushu Electric Power Companies, Japan Atomic Power Company, and the Japan Nuclear Cycle Development Institute. The Kamioka Mining and Smelting Company has provided service for the activities in the mine.

KamLAND was made possible by the scientific vision of Atsuto Suzuki whose ideas have led to the astounding success of KamLAND experiment.

Of all KamLAND collaborators I feel most indebted to my advisor Yuri Kamyshkov for his support and for his patience. His remarkable expertise in nearly all aspects of modern particle physics has been an essential resource without which this work could have never been done. Other University of Tennessee KamLAND group members helped me a lot as well. William Bugg and Yuri Efremenko shared their vast experience with me and helped to avoid many mistakes. I would like to thank Alexandre Kozlov for the simulation of energy deposition in scintillator and Oleg Perevozchikov for reactor data file format conversion which saved me a lot of efforts during the work on this thesis.

A significant part of my work in KamLAND has been done at RCNS of the Tohoku University in Sendai or in a close interaction with this institution. It was a real pleasure to work at RCNS and I would like to thank all people whom I dealt there with. Of crucial importance was the notably efficient organization of KamLAND data analysis by Kunio Inoue. The explanations of analysis techniques that I got from him were among the main factors that predetermined this study. I also feel very grateful to Sanshiro Enomoto for his explanations of the key methods for terrestrial antineutrino study, to Itaru Shimizu and Koichi Ichimura for their indispensable help with RCNS software and reactor data analysis methodology, to Yoshihito Gando and Kyo

Nakajima for the preparation of reactor data, to Tadao Mitsui and Yasuhiro Kishimoto for fruitful discussions and to Kyohei Nakajima for both interesting discussions and for his friendly help with everyday problems.

The help from the American part of KamLAND collaboration was essential as well, especially during the latest stage of my thesis work. The discussions with Glenn Horton-Smith, Patrick Decowski, Brian Fujikawa, Dan Dwyer and Kazumi Tolich helped me with data analysis and simulation software and clarified some complicated issues associated with the analysis itself. I feel very grateful to John Learned for his encouragement to carry out the directionality study. That study provided insights which later proved absolutely necessary for the main topic of this thesis.

I would like to thank all people who helped me during my stays in Mozumi, regardless whether this help was about technical aspects of KamLAND operation, solving everyday problems or just moral support. Of former and present KamLAND members, I feel most obliged to Evgueni Yakushev, Jason Detwiler, Mitsuko Murakami, Charles Lane, Masayuki Koga, Kengo Nakamura for the support I got from them in Mozumi. Last but not least I would like to express my deepest gratitude to Katsuko Shimizu for her kindness, hospitality and friendship.

Abstract

This dissertation presents a combined study of antineutrinos of terrestrial and reactor origin detected by Kamioka Liquid scintillator Anti-Neutrino Detector (KamLAND). Of special physical interest are neutrino oscillation parameters and the terrestrial antineutrino flux, the former being of a profound importance for new physics beyond the Standard Model, and the latter having significant implications for geophysics.

The analysis described here uses a comprehensive likelihood model to naturally combine terrestrial and reactor antineutrino studies within a single framework. The use of this likelihood model and better event reconstruction tools allowed to obtain narrower limits for the oscillation parameters and the terrestrial antineutrino fluxes than separate reactor and terrestrial antineutrino KamLAND studies had provided before.

Based on 944.4 days of exposure, neutrino oscillation parameters Δm^2_{12}, $sin^2 2\theta_{12}$ are obtained to be $7.52^{+0.19}_{-0.18} \times 10^{-5} eV^2$ and $0.916^{+0.084}_{-0.134}$, respectively, at 0.68 confidence level (CL).

The terrestrial antineutrino rate at KamLAND site is determined to be $46.6^{+19.9}_{-19.2}$ TNU (Terrestrial Neutrino Units, i.e. events per 10^{32} protons per year) at 0.68 CL.

Contents

1 Introduction **1**
- 1.1 Neutrinos: Prediction and Observation . . . 1
- 1.2 Neutrino Oscillations . . . 2
- 1.3 MSW matter effect . . . 6
- 1.4 Solar Neutrino Problem . . . 7
- 1.5 Atmospheric Neutrinos . . . 10
- 1.6 Accelerator Neutrinos . . . 12
- 1.7 Reactor Antineutrinos . . . 13
- 1.8 Terrestrial Antineutrinos . . . 15
- 1.9 Solar Neutrino Oscillation Landscape before KamLAND . . . 16

2 KamLAND **18**
- 2.1 Idea of the Experiment . . . 18
- 2.2 KamLAND Detector . . . 20
- 2.3 First Reactor Antineutrino Result . . . 23
- 2.4 Second Reactor Antineutrino Result . . . 26
- 2.5 Observation of Geologically Produced Antineutrinos . . . 29
- 2.6 Motivation for Combined Analysis . . . 31

3 Event Reconstruction **33**
- 3.1 Waveform Analysis . . . 33
- 3.2 Muon Tracking . . . 34
- 3.3 Energy Reconstruction . . . 35
- 3.4 Vertex Reconstruction . . . 35

4 Reactor Antineutrinos **36**
- 4.1 Reactors around KamLAND . . . 36
- 4.2 Reactor Antineutrino Components . . . 37
- 4.3 Inverse Beta Decay Cross Section . . . 39
- 4.4 Spectrum Distortion . . . 41
- 4.5 Instantaneous Spectrum Calculation . . . 42

5 Terrestrial Antineutrinos **44**
5.1 Sources of Terrestrial Antineutrinos 44
5.2 Terrestrial Antineutrino Spectrum 48
5.3 Goals of the Study 48
5.4 Terrestrial Antineutrino Flux and Oscillations 51

6 Backgrounds **52**
6.1 Accidentals 52
6.2 Muon Induced Correlated Background 57
6.3 Alpha-n Correlated Background 57
6.4 Reactor and Terrestrial Antineutrino Mutual Backgrounding 59

7 Likelihood Analysis **61**
7.1 Simple Likelihood Model 61
7.2 Rate+Time, Rate+Shape and Rate+Shape+Time Analyses 63
7.3 Adding the Backgrounds 65
7.4 Parameter Estimation Errors 66
7.5 Handling the Systematic Uncertainties 67
7.6 Selection Criteria Problem for Combined Analysis 69
7.7 Differential Likelihood 71
7.8 Delayed Spectrum for Correlated Events 77
7.9 Time Separation 77
7.10 Space Separation 78

8 Analysis Resutls **80**
8.1 Rate+Shape Oscillation Analysis 80
8.2 Rate+Shape+Time Oscillation Analysis 81
8.3 Rate+Shape+Time Oscillation Analysis with no 2.6 MeV threshold . 81
8.4 Differential Combined Analysis Oscillation and Terrestrial Results . . 84

9 Conclusions **87**

Bibliography **89**

Appendix **94**

A V2 Vertex Fitter **95**

B Possibility of Antineutrino Direction Reconstruction in LS $\bar{\nu}_e$ Detectors **101**

C Oscillated Reactor Spectrum Calculation Algorithm **107**
C.1 Method A 107
C.2 Method B 108

Vita **112**

List of Tables

5.1 Naturally occurring long-living β^--decaying isotopes with stable products 45
5.2 Thorium Decay Series 46
5.3 Raduim Decay Series 46
5.4 Neptunium Decay Series 47
5.5 Actinium Decay Series 47

7.1 Quantiles for confidence levels 67
7.2 KamLAND $\bar{\nu}_e$ selection criteria 71

B.1 Necessary event counts to test geo-reactor hypothesis for given confidence levels (CL) and different vertex reconstruction resolutions . . . 105
B.2 Necessary event counts to test geo-reactor hypothesis for given confidence levels (CL) and different background rates 106

List of Figures

1.1 A possible neutrino mixing hierarchy 6
1.2 Solar neutrino energy spectrum for the solar model BS05(OP) 8
1.3 Theoretical predicions of solar neutrino rates by BS05(OP) model compared to experimental results. 9
1.4 Fluxes of ^8B solar neutrinos deduced from different channels of detection in SNO experiments 10
1.5 Super Kamiokande atmospheric neutrino study allowed regions for Δm^2_{23} and $\sin^2 2\theta_{23}$ 11
1.6 K2K allowed regions for Δm^2_{23} and $\sin^2 2\theta_{23}$ 13
1.7 Ratio of measured to expected $\bar{\nu}_e$ events in reactor experiments before KamLAND 15
1.8 "Solar" oscillation parameter regions allowed at 95% CL in2002, before KamLAND 17

2.1 Reactor sites around KamLAND 19
2.2 Schematic diagram of KamLAND detector. [51] 21
2.3 Ratio of measured to expected $\bar{\nu}_e$ events in reactor experiments including KamLAND 23
2.4 Spectrum Distortion in KamLAND First Result 24
2.5 "Solar" oscillation parameter regions after KamLAND First Result . 25
2.6 Time variation of the expected no-oscillation $\bar{\nu}_e$ flux at KamLAND . 27
2.7 KamLAND Second Result antineutrino spectrum 27
2.8 KamLAND reactor antineutrino oscillation Second Result 28
2.9 KamLAND terrestrial antineutrino spectrum with backgrounds . . . 29
2.10 KamLAND terrestrial antineutrino parameter allowed ranges 30

4.1 Baseline distribution of the expected $\bar{\nu}_e$ flux at KamLAND for years 2003 and 2005 37
4.2 Reactor antineutrino energy spectra for ^{235}U, ^{238}U, ^{239}Pu and ^{241}Pu fissions, $\bar{\nu}_e$ per MeV per fission 38
4.3 Cross section of the inverse beta decay reaction as a function of $\bar{\nu}_e$ energy 39
4.4 No-oscillation detection energy spectra for neutrinos from fissions of ^{235}U, ^{238}U, ^{239}Pu and ^{241}Pu 40
4.5 Cumulative no-oscillation detection energy spectra for reactor $\bar{\nu}_e$ . . . 40

4.6 Reactor $\bar{\nu}_e$ Energy Spectrum Distortion 42

5.1 Antineutrino spectra from the Thorium and Radium decay series . . 49
5.2 Detectable terrestrial antineutrino energy spectra 49

6.1 Energy spectra of single events for fiducial cuts 500 and 600 cm . . . 54
6.2 Single event density rate as function of energy and radius 55
6.3 Single event density rate as a function of radius for different energy cuts 56
6.4 ^8He and ^9Li background prompt spectra 58
6.5 Alpha-n background prompt spectrum 59

7.1 Space separation distributions for $\bar{\nu}_e$ coincidences 79

8.1 Oscillation parameters by Rate+Shape analysis with 2.6 MeV energy threshold 82
8.2 Oscillation parameters by Rate+Shape+Time analysis with 2.6 MeV energy threshold 82
8.3 Oscillation parameters by Rate+Shape+Time analysis with 0.9 MeV energy threshold 83
8.4 Oscillation parameters by Rate+Shape+Time analysis with 0.9 MeV energy threshold, LMA1 area. 83
8.5 Oscillation parameters by differential likelihood analysis. 85
8.6 Oscillation parameters by differential likelihood analysis, LMA1 area. 85
8.7 Terrestrial antineutrino parameters obtained by combined differential analysis 86

A.1 A typical pulse shape 96
A.2 V2 fitter bias tests 99
A.3 The V2 fitter resolution tests 100

B.1 Neutron direction as a function of positron direction for $\bar{\nu}_e$ energies 2.2, 3.4, 8.2 MeV. 102
B.2 Displacements of the prompt and delayed signals from the origin . . . 103
B.3 Prompt-to-Delayed vertex displacement 104

Chapter 1

Introduction

1.1 Neutrinos: Prediction and Observation

Neutrinos were postulated by W. Pauli in 1930 [1] as a solution to the apparent energy non-conservation in the β-decay of ^3H nucleus. The continuous spectrum of the process indicated that the decay could not have only two particles as end products, if the conservation of energy and momentum was to be observed. The evasive particle had to be electrically neutral with little or zero mass. It was originally called "neutron" but soon afterwards a much heavier neutral particle now known as neutron was discovered and the particle suggested by Pauli was renamed to "neutrino" ("little neutral one").

Neutrinos were first experimentally observed by F. Reines and C. Cowan in 1956 [2] by the inverse β decay reaction.

$$\bar{\nu}_e + p \rightarrow e^+ + n \tag{1.1}$$

To be exact, the particles observed in that experiment were electron antineutrinos produced in β^- decays, as well as the particles Pauli postulated. In 1962 [3] muon neutrinos (ν_μ) were produced and observed in a accelerator based experiment at the Brookhaven National Laboratory. In the same year, the construction of solar neutrino detector was started by R. Davis. 6 years later the first solar neutrino results were published [4].

In 2000, the last flavor of neutrinos, the tau-neutrinos (ν_τ) was observed in the DONUT experiment [5].

The difficulty of neutrino observation comes from their properties. They have no electric charge no color charge, so the only remaining force they can measurably interact with is the weak interaction. However the cross sections of the reactions mediated by the weak interaction are small. That's why neutrino experiments typically require either big detectors or/and long exposure times or high neutrino fluxes.

The Standard Model of Particle Physics (see e.g. [6]) has three neutrino flavors, ν_e, ν_μ, ν_τ and three corresponding antiparticles, $\bar{\nu}_e$, $\bar{\nu}_\mu$, $\bar{\nu}_\tau$. Along with three charged

leptons (e, μ, τ) and their antiparticles ($\bar{e}$, $\bar{\mu}$, $\bar{\tau}$) they constitute the class of elementary particles called leptons. Another class of elementary particles called quarks (6 quarks and corresponding antiquarks).

In the Standard Model, all neutrinos have zero mass, zero charge and a spin 1/2. However there seems to be no reason why neutrinos should be massless. Direct measurements of antineutrino mass have not found indications for finite neutrino masses yet [7], [8]. The upper limit for $\bar{\nu}_e$ average mass is currently 2.3 eV at 0.95 C.L., which suggests that electron antineutrino is "lighter" than the electron by more than 5 orders of magnitude. However, with the discovery of neutrino oscillations in several different experiments, the zero-mass hypothesis was excluded since the effect of oscillations requires non-zero neutrino masses.

1.2 Neutrino Oscillations

Neutrino oscillation is a quantum mechanical effect of its flavor transformation, e.g. $\nu_e \rightarrow \nu_\mu$. It was suggested by Pontecorvo [9], [10] and, independently, by Maki, Nakgawa and Sakata [11]. The flavor of a neutrino is actually its weak interaction eigenstate, so neutrino detection, as based on weak interactions is, generally, flavor-sensitive. But the flavor eigenstates are not the same as mass eigenstates which govern the propagation of neutrinos. The general form of the connection between the mass and flavor eigenstates is given by:

$$|\nu_l\rangle = \sum_{i=1}^{3} U_{li}|\nu_i\rangle, \quad l = e, \mu, \tau \tag{1.2}$$

where l is a flavor index and $i = 1, 2, 3$ are neutrino mass eigenstates. The U_{li} matrix is called Pontecorvo-Maki-Nakagawa-Sakata (PMNS) matrix and is the neutrino analog of Cabibo-Kobayashi-Masukawa (CKM) matrix for quarks [12]. It can be conveniently decomposed as follows:

$$\mathbf{U} = \begin{pmatrix} c_{12}c_{13} & s_{12}c_{13} & s_{13}e^{-i\delta} \\ -s_{12}c_{23} - c_{12}s_{23}s_{13}e^{i\delta} & c_{12}c_{23} - s_{12}s_{23}s_{13}e^{i\delta} & s_{23}c_{13} \\ s_{12}s_{23} - c_{12}c_{23}s_{13}e^{i\delta} & -c_{12}s_{23} - s_{12}c_{23}s_{13}e^{i\delta} & c_{23}s_{13} \end{pmatrix} \times \begin{pmatrix} e^{i\alpha_1/2} & 0 & 0 \\ 0 & e^{i\alpha_2/2} & 0 \\ 0 & 0 & 1 \end{pmatrix} \tag{1.3}$$

Here, $s_{ij} = \sin\theta_{ij}$, $c_{ij} = \cos\theta_{ij}$, $i, j = 1, 2, 3$. The phase factors α_1 and α_2 are non-zero only if neutrinos are Majorana particles (i.e. neutrinos are their own antiparticles) but have no effect on the oscillations anyway, so the second matrix in decomposition (1.3) can be omitted for our purposes. If neutrino oscillation violates CP symmetry, the phase factor δ is non-zero. No experimental evidence whether this is the case

or not is available yet. There are six independent parameters in the PMNS matrix, θ_{12}, θ_{13}, θ_{23}, δ, α_1, α_2. Two other parameters take part in the neutrino oscillation phenomenon, the differences between the three neutrino mass eigenstates.

The propagation of a free neutrino in i-th mass eigenstate follows the plane-wave solution of time-dependent Hamiltonian.

$$|\nu_i(t)\rangle = e^{-i(Et-\mathbf{p}\cdot\mathbf{x})}|\nu_i(0)\rangle \tag{1.4}$$

In natural units ($\hbar = c = 1$), we have for energy:

$$E = \sqrt{p^2 + m_i^2} = p\sqrt{1 + (\frac{m_i}{p})^2} \tag{1.5}$$

In the ultrarelativistic limit ($p \gg m$), owing to the approximation $\sqrt{1+\epsilon} \approx 1 + \epsilon/2$,

$$E \approx p + \frac{m_i^2}{2p} \tag{1.6}$$

$p \gg \frac{m_i^2}{2p}$ and $t \approx L$, the distance the neutrino has travelled. Finally, for the mass eigenstate at distance L we have:

$$|\nu_i(L)\rangle = e^{-im_i^2 L/2E}|\nu_i(0)\rangle \tag{1.7}$$

If a neutrino was created in flavor eigenstate l then by the time it has travelled distance L its state will be

$$|\nu(t)\rangle = \sum_{i=1}^{3} U_{li} e^{-im_i^2 L/2E}|\nu_i\rangle \tag{1.8}$$

The probability to find this neutrino in flavor eigenstate m is

$$\begin{aligned} P(\nu_l \to \nu_m) &= |\langle\nu_m|\nu(L)\rangle|^2 \\ &= |\sum_{i=1}^{3} U_{li}^* U_{im} e^{-im_i^2 L/2E}|^2 \\ &= \sum_{i=1}^{3}\sum_{j=1}^{3} (U_{li}^* U_{im} U_{lj} U_{jm}^*) e^{-i(m_i^2 - m_j^2)L/2E} \end{aligned} \tag{1.9}$$

A more convenient form of writing the same

$$\begin{aligned} P(\nu_l \to \nu_m) &= \sum_{i=1}^{3} |U_{li}|^2 |U_{im}|^2 \\ &+ \sum_{i=1}^{3} \sum_{j \neq i} Re(U_{li}^* U_{im} U_{lj} U_{jm}^*) \cos(\frac{m_i^2 - m_j^2}{2E} L) \\ &+ \sum_{i=1}^{3} \sum_{j \neq i} Im(U_{li}^* U_{im} U_{lj} U_{jm}^*) \sin(\frac{m_i^2 - m_j^2}{2E} L) \end{aligned} \tag{1.10}$$

Denoting $\Delta m_{ij}^2 \equiv m_i^2 - m_j^2$ and using the unitarity of matrix U, (1.10) can be simplified further to:

$$\begin{aligned} P(\nu_l \to \nu_m) &= \delta_{lm} \\ &- 4 \sum_{i=1}^{3} \sum_{j<i} Re(U_{li}^* U_{im} U_{lj} U_{jm}^*) \sin^2(\frac{\Delta m_{ij}^2}{4E} L) \\ &+ 2 \sum_{i=1}^{3} \sum_{j<i} Im(U_{li}^* U_{im} U_{lj} U_{jm}^*) \sin^2(\frac{\Delta m_{ij}^2}{2E} L) \end{aligned} \tag{1.11}$$

There are only two independent Δm_{ij}^2 since

$$\Delta m_{12}^2 + \Delta m_{23}^2 + \Delta m_{31}^2 = m_1^2 - m_2^2 + m_2^2 - m_3^2 + m_3^2 - m_1^2 \equiv 0 \tag{1.12}$$

Assuming CPT invariance,

$$P(\nu_l \to \nu_m) = P(\bar{\nu}_m \to \bar{\nu}_l) \tag{1.13}$$

is always true but

$$P(\nu_l \to \nu_m) = P(\bar{\nu}_l \to \bar{\nu}_m) \tag{1.14}$$

holds only if CP invariance holds as well since

$$P(\nu_l \to \nu_m; U) = P(\bar{\nu}_l \to \bar{\nu}_m; U^*) \tag{1.15}$$

However, for the oscillation into the same flavor to be symmetric over charge conjugation:

$$P(\nu_l \to \nu_l) = P(\bar{\nu}_l \to \bar{\nu}_l) \tag{1.16}$$

CPT invariance is enough. In particular, for $\bar{\nu}_e$ and ν_e disappearance experiments

$$\begin{aligned} P(\nu_e \to \nu_e) &= P(\bar{\nu}_e \to \bar{\nu}_e) \\ = 1 &- \cos^4(\theta_{13}) \sin^2(2\theta_{12}) \sin^2(\Delta m^2_{21} L/4E) \\ &- \sin^2(2\theta_{13}) \sin^2(\Delta m^2_{32} L/4E) \end{aligned} \tag{1.17}$$

Oscillation length is the distance over which the phase between two mass eigenstates changes by 2π.

$$L_{ij} = \frac{4\pi E}{\Delta m^2_{ij}} \tag{1.18}$$

There is strong experimental evidence that $\Delta m^2_{12} \ll \Delta m^2_{23}$ and therefore $L_{12} \gg L_{23}$. For long distances and if $\sin^2 2\theta_{13}$ can be considered small the equation (1.17) takes on the form

$$P(\nu_e \to \nu_e) \approx 1 - \sin^2(2\theta_{12}) \sin^2(\Delta m^2_{21} L/4E) \tag{1.19}$$

since $\cos^4(\theta_{13} \approx 1)$ and the last term oscillates rapidly around $\frac{1}{2}\sin^2(2\theta_{13})$ and, for any experiment with finite energy resolution, averages to this small value. This expression for $\bar{\nu}_e$ survival probability is applicable to KamLAND.

For shorter distances (L $\sim$ 1-5 km), $\sin^2(\Delta m^2_{21} L/4E)$ is nearly zero, but $\sin^2(\Delta m^2_{32} L/4E)$ is not. The approximate $\bar{\nu}_e$ survival probability becomes

$$P(\nu_e \to \nu_e) \approx 1 - \sin^2(2\theta_{13}) \sin^2(\Delta m^2_{32} L/4E) \tag{1.20}$$

Newly proposed medium-baseline experiments Double CHOOZ and Daya Bay are expected to be sensitive to the oscillation parameters entering this formula, in particular $\sin^2(2\theta_{13})$.

Before proceeding, it may be useful to cover one issue in more detail. This thesis follows the common two-index convention for mixing angle denomination: θ_{12}, θ_{23}, θ_{12}. Technically, this convention is incorrect and has been criticized by theorists. First, only three angles are possible rather than nine, and their indexing should be one-dimensional. Those mixing angles are analogous to the three Euler angles in a rotation transformation, so the tensor-like notation is not appropriate. Moreover, such a nomenclature is even more confusing when compared with that for Δm^2. In the latter case, the numerical indices correspond to the mass eigenstates which are denoted by numbers $1, 2, 3$, as opposed to the flavor eigenstates represented by letters e, μ, τ. Δm^2_{12} is indeed the difference in squared mass eigenvalues 1 and 2. However θ_{12} has little to do with mass eigenvalues $1, 2$ or the corresponding eigenstates. Two different mass eigenstates are orthogonal, so there is no mixing between them. The actual "mixing" or rather mutual orientation is between the mass and the flavor *eigenspaces*. In the case of three masses and three flavors, the mixing can be fully described by three angles. In the two-mass, two-flavor case there would be only one mixing angle.

An alternative, somewhat less widespread way to index both mixing angles and Δm^2 is to refer to them as "solar" or "atmospheric" for indices "12" and "23", respectively. This may be a little better but still quite misleading since the mixing angles and squared mass differences are denoted in the same way. Once again, there is no physical affiliation between the Δm^2_{solar}, θ_{solar}. They are grouped together just because they can be measured by solar neutrino experiments, owing to the interplay of the actual mass differences, available neutrino energies and baselines.

A possible neutrino mass hierarchy is shown in Figure 1.1. Each mass eigenstate is a superposition of different weak interaction eigenstates and vice versa.

Bottom line is that "solar" or "12" parameters are measured at solar neutrino or long-baseline reactor antineutrino experiments. "atmospheric" or "13" parameters are measured at atmospheric neutrino and accelerator based experiments. θ_{13} can be measured by medium-baseline reactor experiments.

KamLAND measures "solar" oscillation parameters: $\sin^2\theta_{12}$ and Δm^2_{12}.

1.3 MSW matter effect

The neutrino oscillations discussed in the previous paragraph are those of free neutrinos, and this was explicitly used in (1.4). This is perfectly valid for the neutrino propagation through vacuum. However if neutrinos can interact with the matter through the weak interactions, the equations, generally, do not hold anymore. What causes a major effect on the neutrino oscillation matter is the "asymmetry" between neutrino flavors. All flavors (electron, μ, τ) can interact with electrons through Z-boson mediated neutral current interaction, but only electron neutrino can, additionally, exchange charge with electrons through W-bosons since there are electrons

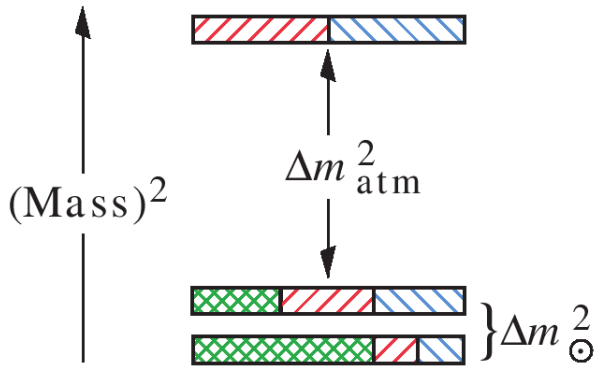

Figure 1.1: A possible neutrino mixing hierarchy. Three-neutrino m^2 spectrum that accounts for the flavor changes of the solar and atmospheric neutrinos. The ν_e fraction of each mass eigenstate is crosshatched in green, the ν_μ fraction is indicated by the right-leaning red hatching, and the ν_τ fraction by left-leaning blue hatching. [13]

but no muons or τ particles in the matter. In terms of phase change, the additional interaction shifts the phase of ν_e component relative to the phase of ν_μ and ν_τ components. This effect was discovered by Wolfenstein [14], Mikheyev and Smirnov [15] and named Mikheyev-Smirnov-Wolfenstein (MSW) effect.

This MSW effect is especially important for solar neutrinos that propagate through the high-density interior of the Sun. However, for KamLAND and other reactor neutrino experiments, the matter effects don't play a significant role and are not included in the considerations here.

1.4 Solar Neutrino Problem

As mentioned above, the first solar neutrinos were observed in 1968 [4]. The neutrino detector was located 1.5 km deep in Homestake Mine in South Dakota. A big tank was filled with 390 m^3 of perchloroethylene C_2Cl_4, a chlorine-based cleaning fluid. The inverse β-decay reaction was used to detect the neutrinos:

$$^{37}Cl + \nu_e \rightarrow {}^{37}Ar + e^- \tag{1.21}$$

Only the neutrinos with energies above the 814 keV threshold can be detected. The detection was based on the fact that ^{37}Ar nucleus is radioactive with half-life of 35 days, which makes it possible to monitor its production rate. The detector was bubbled with helium on the monthly basis to extract the ^{37}Ar nuclei that had formed and evaluate the number of captured neutrons.

While there was a clear evidence of the neutrino signal, it was consistently about one third of what had been predicted by the Standard Solar Model (SSM) [16]. This started the so-called "Solar Neutrino Problem" which was solved only recently with the experimental proof of neutrino oscillations. In the beginning, the contradiction didn't appear to be a serious problem since both SSM and the Homestake experiment had large uncertainties. However, later the SSM has been refined and the error margins for the neutrino experiment went down with longer exposure time and the discrepancy became statistically significant.

The Standard Solar model (SSM) [16] predicts that almost 98.5% of solar energy comes from the pp-chain ("pp", for "proton-proton") and the rest is attributed to the Carbon-Nitrogen-Oxygen (CNO) cycle. The net effect of the pp-chain, including the annihilation of the positrons is

$$4p + 2e^- \rightarrow \quad {}^4He + 2\nu_e + 26.73MeV \tag{1.22}$$

The full spectrum of solar neutrinos is shown in Figure 1.2. Unfortunately, due to the relatively high energy threshold ($E_\nu > 0.814keV$) of reaction (1.21), most of this spectrum cannot be detected in chlorine neutrino experiments. A similar reaction with ^{71}Ga has a much lower threshold of 233 keV and better suited for the detection of low energy solar neutrinos:

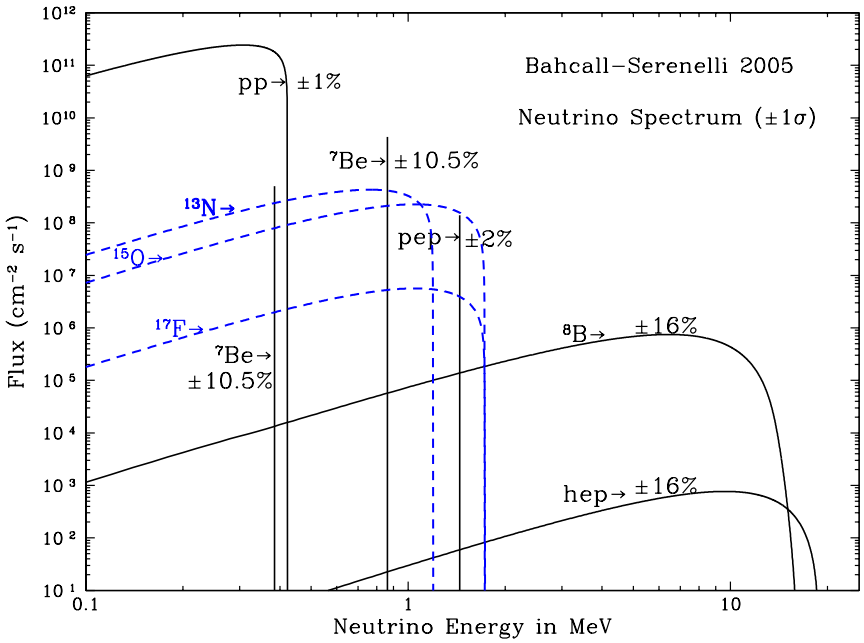

Figure 1.2: Solar neutrino energy spectrum for the solar model BS05(OP) [17]. Black solid lines belong to the pp-chain; CNO components are shown in dashed blue lines.

$$^{71}Ga + \nu_e \rightarrow {}^{71}Ge + e^- \tag{1.23}$$

Three experiments have detected solar neutrinos using ^{71}Ga reaction: GALLEX [18], GNO [19] and SAGE [20]. All have detected a lower number of neutrinos than was predicted by the SSM, although the deficit was somewhat less significant than in the Homestake experiment — about one half of the expected signal.

The Water Cherenkov technique can also be used for solar neutrino detection. Compared with radiochemical methods discussed above, it has a rather high practical energy threshold of about 5 MeV, which is a serious limitation. However it has important advantages of real-time observation in large-mass detectors and the sensitivity to the direction of incoming neutrinos. These advantages can provide the evidence that the detected neutrinos are coming from the Sun and not somewhere else. Additionally, Cherenkov detectors are sensitive to neutrino energies, as far as the energies are above the threshold, allowing for energy spectrum analysis. The detection is based on the following elastic scattering reaction:

$$\nu_l + e^- \rightarrow \nu_l + e^-, \text{ where } l = e, \mu, \tau \tag{1.24}$$

The reaction can involve all neutrino weak interaction eigenstates however, for ν_e, it can go through both neutral current and charge current, whereas for ν_μ, ν_τ only the

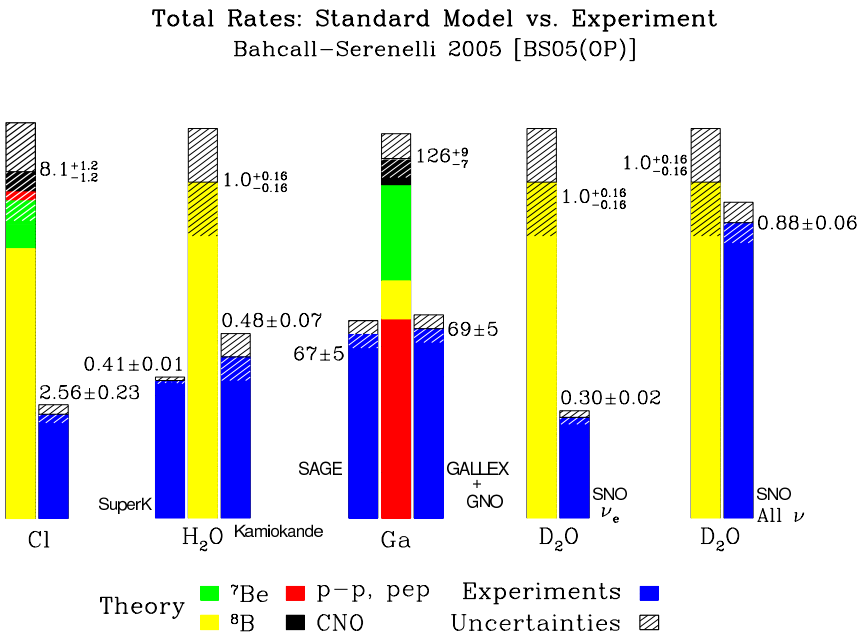

Figure 1.3: Theoretical predicions of solar neutrino rates by BS05(OP) model compared to experimental results. [17]

neutral current reaction is possible. Therefore, cross section for ν_μ, ν_τ is substantially smaller than for ν_e: $\sigma(\nu_{\mu,\tau}e) \approx 0.16\sigma(\nu_e e)$.

Three experiments based on the Cherenkov technique have been carried out: Kamiokande [21], Super Kamiokande (SuperK) [22], and SNO [23]. The first two observed about 50% of neutrinos predicted by SSM (Figure 1.3).

The SNO experiment was unique in that it used ultrapure heavy water D_2O. In addition to the elastic scattering, (1.24), this enabled two reactions on ^2H (deuteron) nucleus, charge-current (CC):

$$\nu_e + d \rightarrow p + p + e^- \tag{1.25}$$

and neutral-current (NC):

$$\nu_l + d \rightarrow p + n + \nu_l, \text{ where } l = e, \mu, \tau \tag{1.26}$$

The CC reaction is possible with electron neutrinos but the NC reaction is equally sensitive to all three flavors. The NC reaction can be distinguished by double coincidence since the neutron is later captured on deuteron, producing a 6.25 MeV gamma. In 2002, SNO reported the first direct evidence for solar neutrino flavor transformation [23]. At the second phase of the experiment, salt ($NaCl$) was added to the detector to enhance the neutron capture detection [24]. ^{35}Cl nucleus has a higher

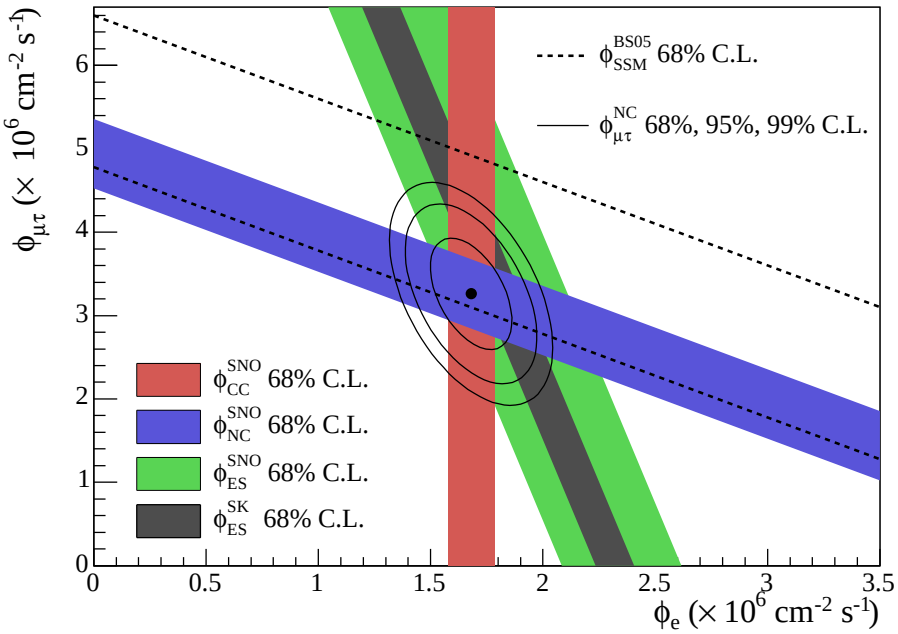

Figure 1.4: Fluxes of ^8B solar neutrinos deduced from different channels of detection in SNO experiments. [25]

capture cross section than ^2H and releases several gammas with total energy about 8.6 MeV.

The ability to distinguish between the two reactions, one sensitive to electron neutrinos only and another to all three flavors, provided an opportunity to solve the Solar Neutrino Problem. SNO has shown that there is really no deficit of solar neutrinos but part of ν_e turn into ν_μ and ν_τ which are undetectable or almost undetectable by earlier experiments (Figure 1.4).

1.5 Atmospheric Neutrinos

It was the observation of atmospheric neutrinos that actually provided the first direct evidence for neutrino oscillations. Unlike solar neutrinos, the expected flux was not known well enough but the ratio between the neutrino flavors is constrained. The difference between expected and observed ratios can be attributed to neutrino oscillations. Atmospheric neutrinos are produced in the decays of pions and other mesons generated in the upper atmosphere by cosmic rays. A pion decays into a muon and muon neutrino. Then the muon decays producing an electron, an electron neutrino

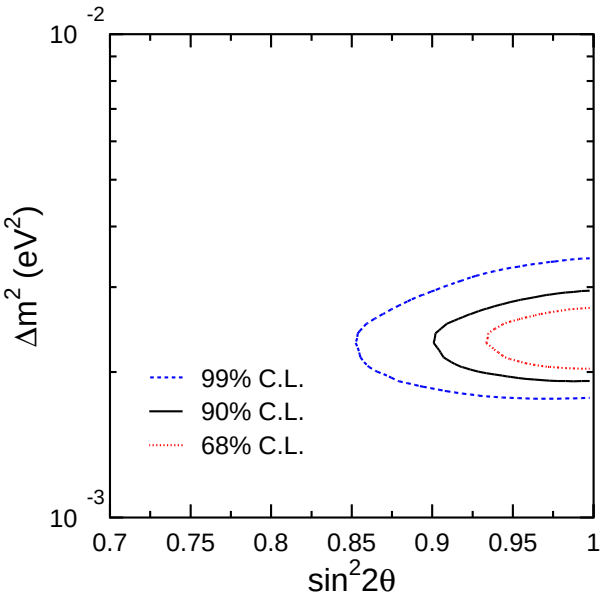

Figure 1.5: Super Kamiokande atmospheric neutrino study allowed regions for Δm^2_{23} and $\sin^2 2\theta_{23}$. [31]

and one more muon neutrino:

$$\begin{aligned} \pi^+ \rightarrow \quad & \mu^+ \quad + \quad \nu_\mu \\ & \mu^+ \quad \rightarrow e^+ + \bar{\nu}_\mu + \nu_e \end{aligned} \tag{1.27}$$

$$\begin{aligned} \pi^- \rightarrow \quad & \mu^- \quad + \quad \bar{\nu}_\mu \\ & \mu^- \quad \rightarrow e^- + \nu_\mu + \bar{\nu}_e \end{aligned} \tag{1.28}$$

In no-oscillation scenario, the ratio of $(\nu_e + \bar{\nu}_e)$ flux to $(\nu_\mu + \bar{\nu}_\mu)$ flux is expected to be 1/2.

Water Cherenkov detectors Kamiokande [26], and IMB [27] actually observed about the same number of ν_{mu} and ν_e events. The Iron calorimeter detector Soudan2 reported [28] a similar relative deficit of ν_{mu} [28], although earlier iron calorimeter detectors, NUSEX [29] and Frejus [30], found the ν_e to ν_μ ratio consistent with expected.

The Super-Kamiokande detector combined a large exposure with directionality detection, which allowed for quantitative measurement of neutrino oscillation parameters. The study was based on the zenith angle dependence of the atmospheric ν_μ and ν_e fluxes. The oscillation baseline changed from 15 km to almost 13,000 km for zenith to nadir direction, respectively.

The most recent results for the neutrino oscillation parameters are shown in Figure 1.5.

1.6 Accelerator Neutrinos

Accelerator produced neutrinos are similar to atmospheric neutrinos in that they are produced from pion decays. The pions are generated when proton beams from an accelerator hit a metal target. The neutrinos from pion decays are detected at some distance from the target. Detectors can be of Cherenkov type (Super Kamiokande in K2K [32], MiniBooNE [33]), liquid scintillator (LSND [34], KARMEN [35]), or calorimeter (MINOS [36]).

Accelerator neutrino experiments detect the disappearance of muon neutrinos and antineutrinos but some of them can also search for the appearance of ν_e from ν_μ.

LSND (Liquid Scintillator Neutrino Detector) of Los Alamos Neutron Science Center has observed the excess of ν_e events which could be interpreted as the $\nu_\mu \rightarrow \nu_e$ oscillations. The problem with this result was that it implied a very high value for squared mass difference $\Delta m^2_{LSND} > 0.1eV^2$ inconsistent with the other two well established values. If $\Delta m_{12} \sim 7.5 \times 10^{-5}eV$ and $\Delta m_{23} \sim 2 \times 10^{-3}eV^2$, the remaining difference cannot be that large.

It is extremely important to confirm or refute the LSND result. If it is confirmed the implications will be profound. In particular, this would require one more neutrino mass eigenstate and flavor. Besides, the PMNS matrix may become non-uniform, resulting in a more complicated neutrino oscillation theory.

The KARMEN (KArlsruhe Rutherford Medium Energy Neutrino) experiment has the sensitivity to the same kind of oscillations. It found no excess of electron neutrinos, so the LSND result was not confirmed. However the sensitivity of the experiment was insufficient to exclude all of the LSND allowed oscillation regions.

MiniBoonNE (Mini Booster Neutrino Experiment) is a Fermilab oil Cherenkov detector experiment. It is a much larger detector than KARMEN, quite capable of confirming or refuting the LSND result completely. It has started taking data 2002.

MINOS (Main Injector Neutrino Oscillation Search) is also a Fermilab project. The detector is located in the Soudan mine, Minnesota and is a segmented steel-scintillator sampling calorimeter. Its advantage is the ability to study the flavor oscillations for neutrinos and antineutrinos separately. It is a long baseline neutrino experiment.

The main goal of the K2K (KEK to Kamioka) experiment is to obtain a confirmation of the Super Kamiokande atmospheric oscillation result. The neutrinos are produced at the High Energy Accelerator Research Organization (KEK) in Ibariki Prefecture and detected by Super Kamiokande in Kamioka, Gifu Prefecture in Japan. The oscillation results for the "Atmospheric" mixing angle and Δm^2 are consistent with the the ones obtained in Super Kamiokande from the analysis of the atmospheric neutrinos, which is an excellent independent cross check. Figure 1.6 shows the "atmospheric oscillation" results of the K2K experiment.

Despite their superior size, neither MINOS nor K2K are sensitive to the LSND oscillation region, so it will probably be MiniBooNE that confirms or excludes the LSND result.

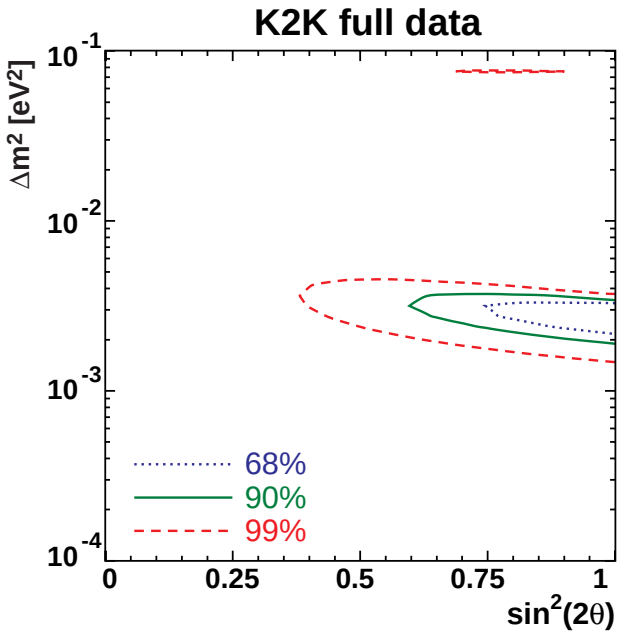

Figure 1.6: K2K allowed regions for Δm^2_{23} and $\sin^2 2\theta_{23}$. [37]

A very important advantage that accelerator neutrino experiments share with reactor antineutrino experiments is that our knowledge about the source is quite conclusive and not model-dependent. In some cases the source is not only directly monitorable but also controllable, which is impossible for atmospheric and solar neutrino experiments.

1.7 Reactor Antineutrinos

Nuclear reactors produce electron antineutrinos through beta decays of short-lived fission products. Many relatively short-based reactor experiments have been performed before KamLAND. Most of them were liquid scintillator (LS) detectors that used the inverse beta decay reaction to detect antineutrinos (1.1). In fact the first observation of ν or $\bar{\nu}$ in history [2] was the detection of reactor antineutrinos through the inverse beta decay technique. The limitation of this technique, the sensitivity to electron neutrinos only and the energy threshold of about 1.8 MeV are not a major problem for reactor experiments. Reactors produce only ν_e anyway and a significant fraction of them has energy above that threshold. On the other hand, the advantage of an efficient background suppression by double coincidence far outweighs the loss of a part of energy spectrum.

Since the $\bar{\nu}_e$ detection by inverse beta decay is of profound importance for the whole study presented in this thesis, it would be instructive to cover it here in more detail. After antineutrino interacts with a proton, a positron and a neutron emerge.

Due to the laws of kinematics, the positron, the much lighter of the two, gets most of the available energy which is about 0.8 MeV less than the energy of the incident $\bar{\nu}_e$.

The prompt signal is generated from the energy deposited by the positron through ionization and Cherenkov radiation, followed by the positron annihilation. The ionization generates scintillation directly, while the UV part of Cherenkov radiation can be absorbed and re-emitted in longer wavelengths by the scintillator. The positron annihilation with an electron releases two 0.511 MeV gammas. The gammas lose energy mostly to Compton scattering on electrons; the electrons cause ionization and hence scintillation. All those processes take place on the time scale of 1 ns and are normally detected as a single event.

The neutron lives much longer than 1 ns. First it thermalizes losing most of its initial kinetic energy in elastic collisions. After thermalization, the neutron continues to experience elastic collisions before being captured on a nucleus in the LS. The capture results in an isotope in an excited state and the isotope is sometimes unstable, with a very short life time. The deexcitation produces gammas and, in case of an unstable nucleus, other particles as well. They are registered by the scintillation. This constitutes the delayed signal. Due to the limited path of the inverse beta and neutron capture products, the prompt and delayed signals are correlated not only in time but also in space.

The time separation from the prompt to delayed signal varies in the range from several microseconds to several hundred microseconds and depends on the cross section of the neutron capture. The cross section differs significantly for different nuclei, a property that has been successfully used in some experiments through LS loading. Loading of LS is an addition of a relatively small amount of the isotope with a cross section higher than that of ^1H and ^{12}C which constitute most of the scintillator. This results in shorter capture time making it possible to narrow the selection window for coincidences and reduce the background rate even further.

After the hypothesis of neutrino oscillations was proposed, several reactor antineutrino experiments attempted to find evidence for antineutrino oscillation. Due to the inverse beta decay detection principle, the oscillation signal in reactor antineutrino detector would be the disappearance of a fraction of the $\bar{\nu}_e$ flux, as part of antineutrinos would oscillate into other flavors which cannot participate in reaction (1.1). ILL [38], Savannah River [39], Bugey [40], Rovno [41], Goesgen [42], Krasnoyarsk [43], Palo Verde [44], Chooz [45] experiments found no $\bar{\nu}_e$ disappearance (Figure 1.7).

With the contemporary knowledge base this result is quite understandable. All those experiments were too short-baselined to be sensitive to the Δm^2_{12}. As for the Δm^2_{23}, although L_{32} is shorter, there is little to no mixing between ν_e flavor eigenstate and ν_3 mass eigenstate (see Figure 1.1), so experiments with electron neutrinos are unlikely to observe this oscillation mode.

Despite the lack of oscillation signal, the significance of those experiments should not be underestimated. The fact that they observed the fluxes in a very good agreement with the expected not only allowed to set limits on the oscillation parameters

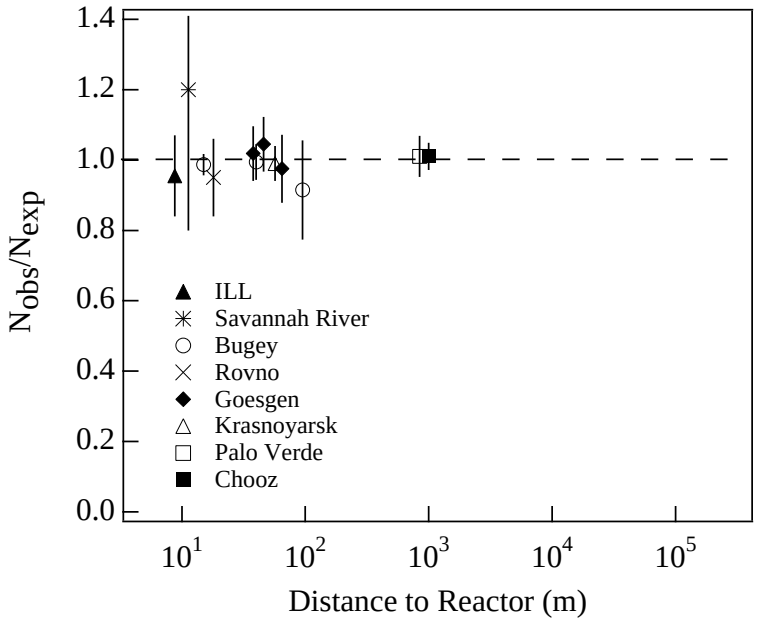

Figure 1.7: Ratio of measured to expected $\bar{\nu}_e$ events in reactor experiments before KamLAND. [13]

but also demonstrated that we can calculate reactor antineutrino fluxes really well. Without this confidence, the later success of KamLAND would not have been possible.

1.8 Terrestrial Antineutrinos

The origin of terrestrial antineutrinos is similar to that of reactor antineutrinos. They are produced in beta-decays of naturally occurring radioactive isotopes. There are several naturally occurring radioactive isotopes, but the expected $\bar{\nu}_e$ flux from many of them is too low to be detected or the energies of the antineutrinos are below the inverse beta decay threshold.

Terrestrial antineutrinos generally have lower energy than reactor antineutrinos and, the inverse beta decay threshold is a serious limitation in their study. Only the antineutrinos from decay chains starting with ^{238}U and ^{232}Th are relatively easy to observe. The radioactive ^{40}K is believed to be rather abundant in the Earth, according to mainstream geological models. The overall antineutrino flux from its decay should be quite substantial as well. Unfortunately, the maximum antineutrino energy from its β^--decay is 1.311 MeV is below the inverse beta decay threshold. The detection of the terrestrial antineutrinos from ^{40}K decays is one of the most challenging tasks for the near future.

There can be another source of terrestrial antineutrinos. Back in 1996, a hypothesis that a nuclear reactor is working in the Earth's core has been proposed [46]. This hypothesis can explain the changes in the magnetic field of the Earth and the

excess of ^3He isotope in magma sources (i.e. volcanic lavas) [47]. However most conventional geological models disfavor this possibility. In particular, the core of the Earth is believed to be depleted in heavy radioactive isotopes, so there should be no fuel for such a reactor. Nonetheless, this hypothesis is worth testing and the study of the antineutrino flux can provide such a test. For such a study, a directionality measurement would be very useful. Unfortunately, a quantitative study shows that practical directionality study in LS antineutrino experiments requires much larger detectors than built so far (Appendix B). Yet, there is a possibility to test this hypothesis based on rate and spectrum analysis, once a fairly large antineutrino detector is constructed far enough from nuclear power plants and other reactors.

It's worth noting that the antineutrinos from the Earth's core reactor, should it exist, are essentially reactor antineturinos and should be studied as such. In particular, their spectrum must be typical of reactor antineutinos, their only difference being the directionality and oscillation patterns.

Terrestrial neutrinos from the decay series starting with ^{238}U and ^{232}Th have a much "softer" spectrum than reactor antineutrinos, regardless of the origin of the reactor. Later in this work, the terms "terrestrial antineutrinos" or "geo-neutrinos" will be used exclusively for those relatively low-energy antineutrinos.

The only experiment that has managed to observe geologically produced antineutrinos so far is KamLAND [48]. The antineutrino flux from ^{238}U and ^{232}Th decay chains was detected. This result is covered in more detail in Section 2.5.

1.9 Solar Neutrino Oscillation Landscape before KamLAND

As was mentioned above, due to the combination of practically achievable baselines and typical $\bar{\nu}_e$ energies, reactor antineutrino experiments can be sensitive to the "solar" oscillation parameters, namely θ_{12} and Δm^2_{12}. So, in order to see the impact of KamLAND, it would be interesting to look at the situation that existed in the study of those parameters before 2002.

Of possible combination regions, the so-called Large Mixing Angle (LMA) solution to the solar neutrino problem was most likely since it didn't contradict any solar ν experiment (red area in Figure 1.8). Other solutions were disfavored by one or more experiments. Yet the oscillation picture was not quite clear, even for those two oscillation parameters. First, the exclusion of alternative solutions was not statistically strong enough. Second, the LMA area established by solar neutrino experiments was quite wide in Δm^2. Despite looking fairly small on a logarithmic plot, the allowed region was still about a 5-fold change in Δm^2 at a rather modest 95% CL. New experiments with high sensitivity to this parameter were necessary.

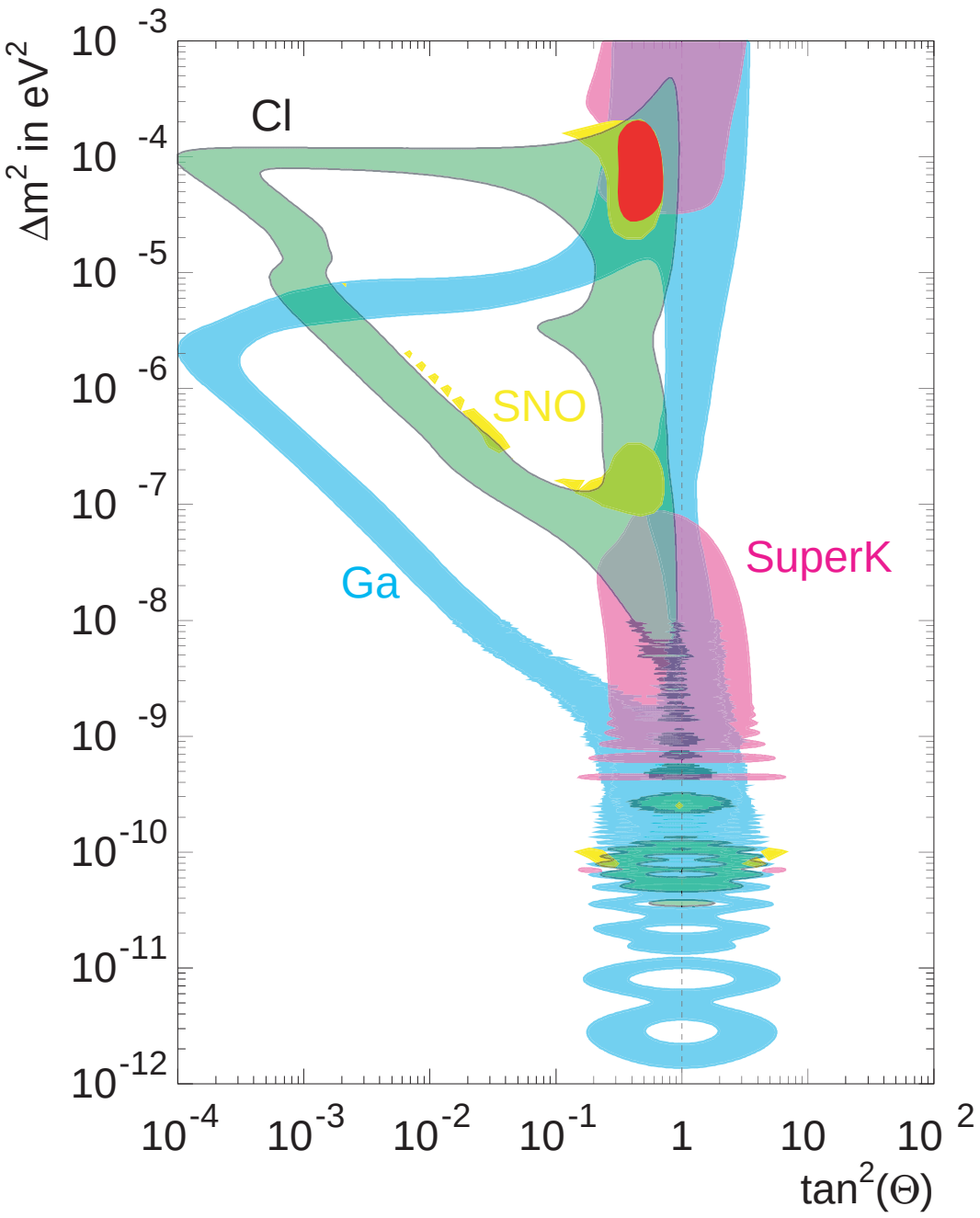

Figure 1.8: "Solar" oscillation parameter regions allowed at 95% CL in2002, before KamLAND. [49]

Chapter 2

KamLAND

2.1 Idea of the Experiment

KamLAND is the KAMioka Liquid scintillator AntiNeutrino Detector. It is a long-baseline 1-kiloton unloaded liquid scintillator (LS) detector located in Kamioka mine at the site of the old Kamiokande detector.

Its first goal was to provide an independent test for LMA solution of Solar Neutrino Problem (Section 1.9) and, if the result is positive, the measurement of "solar" oscillation parameters with higher accuracy than had been achieved by solar experiments.

As was discussed in Chapter 1, reactor antineutrino experiments are sensitive to "solar" parameters if placed at right distance from the source, which is from 50 to 250 km, assuming the validity of the LMA solution and CPT invariance. Longer baselines will result in a quickly oscillating pattern for the possible values Δm^2, making its precise measurement difficult. Shorter baselines may not be enough to observe $\bar{\nu}_e$ deficit.

It's necessary to note that even the baseline on the order of 100 km is already very long for a reactor $\bar{\nu}_e$ experiment. One needs either a huge detector or an extremely powerful reactor or both to have a sufficient event rate. The design of KamLAND and the choice of its placement were determined by this consideration. On one hand it is the largest liquid scintillator antineutrino detector ever built. On the other hand, its location takes advantage of the surrounding nuclear power plants. Several Japanese nuclear power plants are at a distance between 80 and 220 km (Figure 2.1) from the Kamioka mine, constituting more than 80% of reactor antineutrino flux at KamLAND site.

If LMA solution is the case, KamLAND was expected to see a pronounced deficit of antineutrinos. Moreover, like other scintillator detectors using the reaction 1.1, KamLAND is sensitive to the $\bar{\nu}_e$. The expected reactor antineutrino spectrum can be calculated as well as the total flux. However, as follows from formula (1.19), the disappearance probability depends on the energy. If $E_{\bar{\nu}_{e_1}} \neq E_{\bar{\nu}_{e_2}}$ the deficit of the former

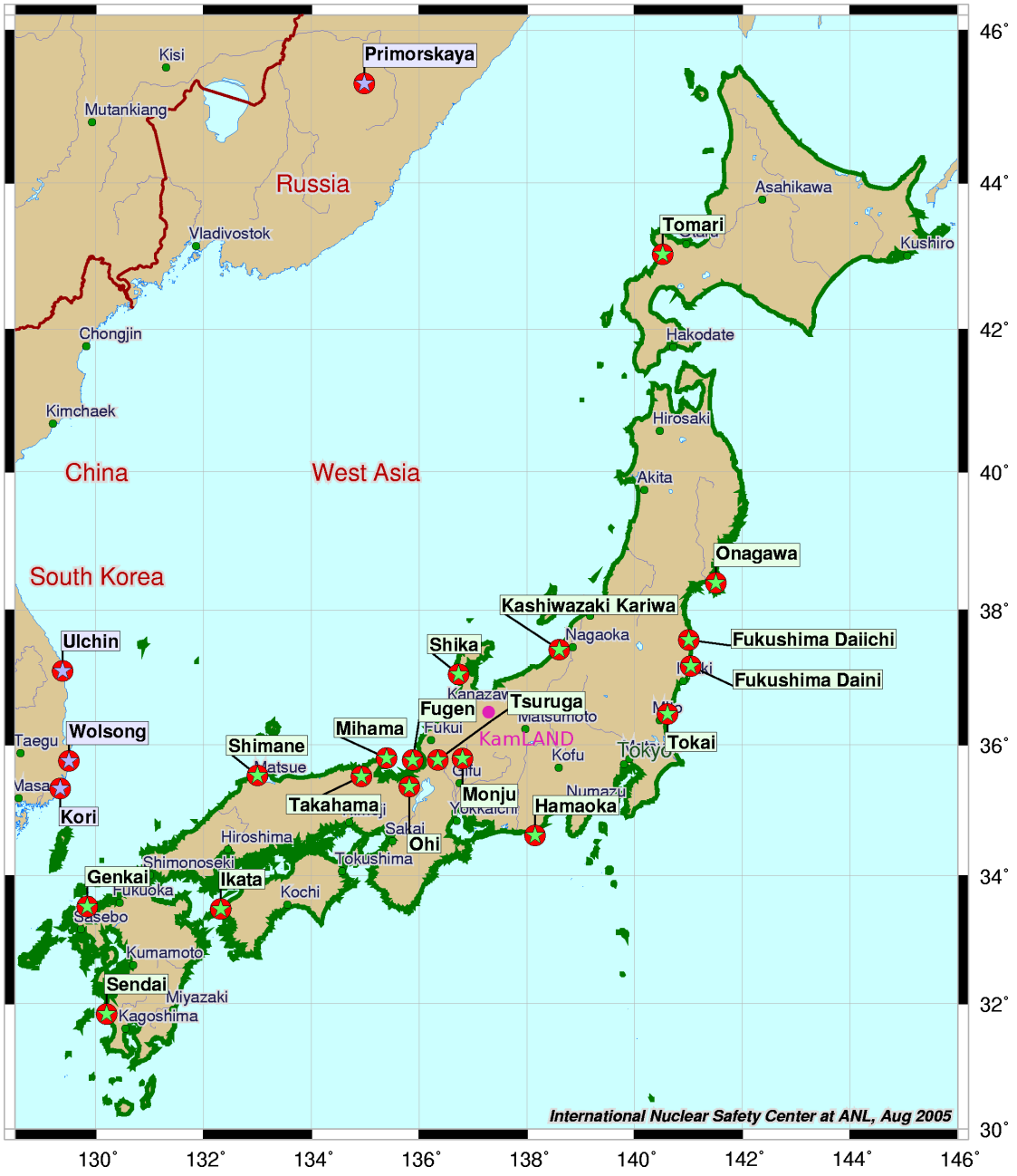

Figure 2.1: Reactor sites around KamLAND. The stars mark reactor sites. KamLAND is marked by the purple circle. [50]

is, generally, different from that of the latter. This leads to a measurable distortion of the observed $\bar{\nu}_e$ spectrum, which provides a more powerful tool for oscillation studies than simple $\bar{\nu}_e$ monitoring. In particular, spectrum analysis can yield a single best fit point in the 2-dimensional oscillation parameter space, while the total rate of $\bar{\nu}_e$, no matter how precisely measured, can only disfavor some areas.

Other goals of KamLAND include the observation and measurement of terrestrial antineutrino flux and, at the next stage of experiment, the direct observation of solar ^7Be neutrinos. The KamLAND collaboration also pursues the goals of the search for rare processes like nucleon decay, relic supernovae neutrinos and neutrino signals from close supernova explosions.

2.2 KamLAND Detector

KamLAND (Figure 2.2), physically, consists of two detectors, the Inner Detector (ID) and the Outer Detector (OD). The ID is an organic liquid scintillator detector. The OD is a water-Cherenkov detector surrounding the ID. The purpose of the ID is to detect events caused by highly energetic cosmic muons and provide vetoing. The actual antineutrino data is collected by the ID.

The core of KamLAND ID is 1 kiloton of liquid scintillator (LS) which is contained in a transparent balloon suspended by Kevlar ropes inside a vessel filled with buffer mineral oil (MO). The balloon is made of 135-μm-thick nylon/EVOH (Ethylene Vinyl Alcohol Copolymer) film, its purpose being to separate the LS from the MO.

KamLAND LS is composed of 80.2% dodecane ($C_{12}H_{26}$), 19.8% pseudocumene (1,2,4-trimethylbenzene, C_9H_{12}) and 1.52 gliter of PPO (2,5-diphenyloxazole, $C_{15}H_{11}NO$). PPO is the scintillating molecule, pseudocumene is the energy transferor and dodecane is the diluter. Dodecane was chosen because it is chemically less aggressive than pseudocumene and reduces the flash point of the scintillator to acceptable levels. Other advantages include high Hydrogen/Carbon ratio, light transparency and stability.

MO shields LS from external radiation and fast neutrons. It is composed of dodecane and isoparaffins to have a density 0.04% lower than that of LS.

The events in the ID are viewed by 1325 17" PMT's and 554 older 20" PMT's. The 17" PMT's are line-focus type tubes. This design choice provides very good time and charge resolutions, a quality important for event reconstruction. The 20" PMT's are of the venetian-blind type and are inferior in those respects but have an advantage of almost 40% larger detection area. The 17"-only PMT coverage of ID is only 22%, while with the addition of 20" tubes it is 34%. The quantum efficiency of the PMT's of both types is about 20% for the typical wavelengths produced by the scintillator, 350-400 nm.

The steel sphere separates ID from OD. The OD has 225 20" PMT's and filled with 2600 m^3 of ultra-purified water. The OD detects muons by the Cherenkov light that they produce while passing through the water. Besides the muon veto system,

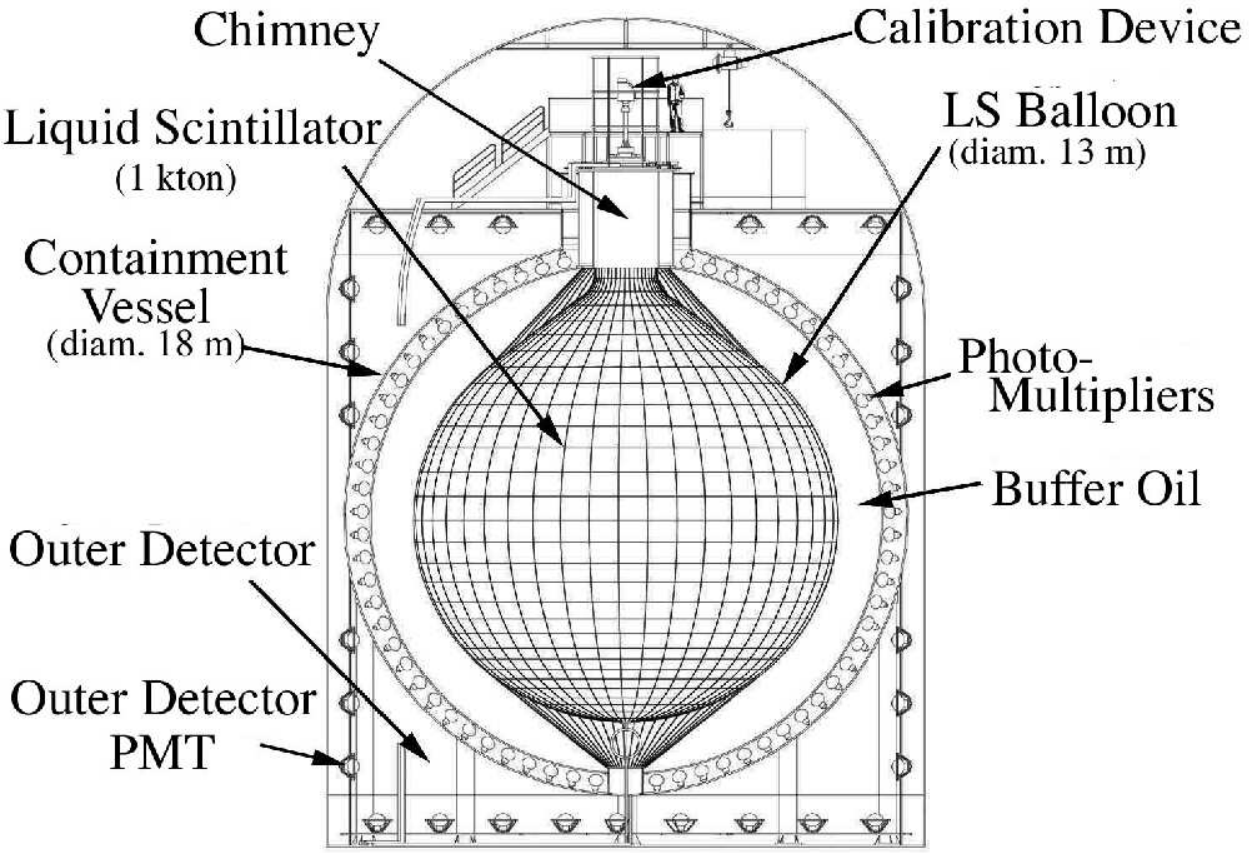

Figure 2.2: Schematic diagram of KamLAND detector. [51]

the OD plays the role of an additional shield for the LS area from radioactivity of the surrounding rocks.

Each PMT is connected to two ATWD (Analog Transient Waveform Digitizers) chips custom-developed at Lawrence Berkeley National Laboratory. These chips digitize and record PMT output voltage, producing 128-sample digital waveforms represented by 10-bit values per sample. The sampling rate is programmable and, in real experiments, is fixed at approximately 0.65 GHz, so that the whole 128-sample window is about 200 ns long. Digitization takes about 150 times longer but the dead time is minimized by having two alternating ATWD chips connected to the same PMT. The ATWD's are self-launching on the basis of the discriminator threshold set to 1/3 of a single photoelectron (SPE) voltage. If a signal exceeds this threshold, the ATWD captures the waveform but not necessarily digitizes it. Owing to the delay circuit introduced before its input, the ATWD stores the whole of the waveform and not just the part past the discriminator threshold. The ATWD's and supporting circuits are mounted on front-end electronics (FEE) boards. There are 12 channels on each FEE board, 20 boards on each crate and 10 VME crates in KamLAND.

Writing down all the waveforms is technically impossible due to the amount of data and in fact is unnecessary. Every significant event in the ID produces hundreds of photons, so that a large number of PMT's are hit within a very short period of time. Only the waveforms from such events actually need to be written. To implement this approach, the trigger module has been developed at Stanford University.

The trigger works in the following way. It distributes a 40 MHz clock to all FEE boards and keeps them synchronized. At every clock tick it sums up the number of 17" ID PMT's that produced a signal, as well as the numbers of such 20" PMT's in different sections of the OD. If these numbers exceed some programmable thresholds trigger issues a global acquisition signal to all FEE. When this signal arrives, ATWDs digitize the previously captured waveforms and the data is written to the disks. Besides the "physics" acquisition triggers issued when the number of ID hits exceeds the threshold, there are many "service" triggers that force data taking even when there are no events in ID.

KamLAND data acquisition (DAQ) software, KiNOKO, is a networked parallel system developed at Tohoku University. Due to its distributed processing nature, it reads ATWD data independently, so the waveforms are written to disk out of time order. Event building stage takes care of this by sorting the waveforms according to their times.

Even with normal trigger settings, KamLAND produces more than 500 GBytes of raw data per day, which is huge and can cause serious logistic problems. In order to mitigate this issue, most of the data is compressed by customized routines by about a factor of 3. The compression is lossless and performed in real time at the stages of data taking and event building.

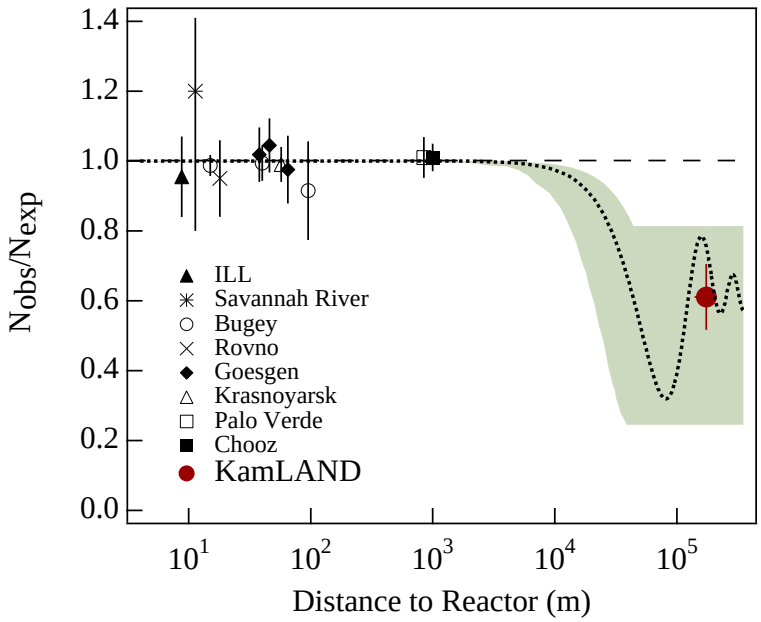

Figure 2.3: Ratio of measured to expected $\bar{\nu}_e$ events in reactor experiments including KamLAND. [51]

2.3 First Reactor Antineutrino Result

In early 2003, KamLAND reported the first result of evidence for reactor $\bar{\nu}_e$ disappearance [51], which became since then one of the the most cited papers in experimental particle physics. The main result was that, unlike earlier, shorter-baselined reactor antineutrino experiments, KamLAND did observe a deficit of $\bar{\nu}_e$ events (Figure 2.3). Instead of 86.8 events expected in 145.1 days of data taking only 55 were detected.

Like other experiments using the inverse beta decay reaction, KamLAND is sensitive to antineutrino energy and capable of detecting the $\bar{\nu}_e$ energy spectrum distortion associated with oscillations. The observed spectrum distortion is shown in in Figure 2.4. Despite the small statistical base, this distortion allowed the first estimations of "solar" oscillation parameters. The best fit was found to be: $\sin^2 2\theta = 1.0$ and $\Delta m^2 = 6.9 \times 10^{-5} eV^2$.

The significance of this result was two-fold. First of all, it was the first experimentally observed reactor $\bar{\nu}_e$ deficit. Second, although the precise determination of oscillation parameters was not possible at that stage, all solutions to Solar Neutrino Problem except the LMA were strongly disfavored. The impact of KamLAND result on the "solar" oscillation parameter allowed regions is shown in Figure 2.5.

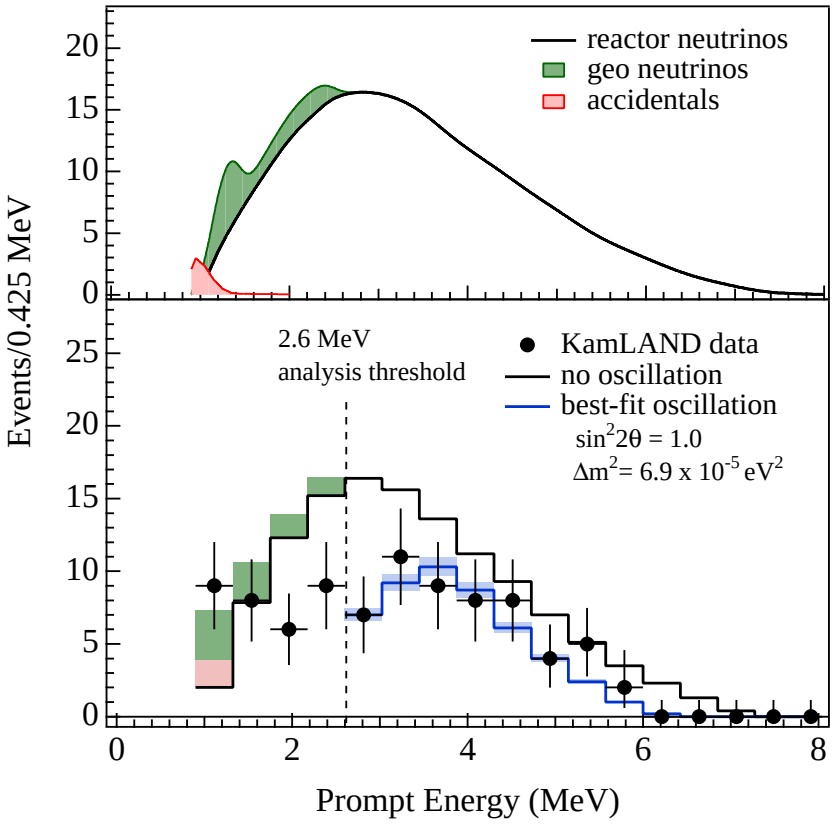

Figure 2.4: Upper panel: Expected $\bar{\nu}_e$ energy spectrum with known backgrounds. (α-n background was not known at that time and not shown here) Lower panel: Observed distorted spectrum along with no-oscillation expected and best fit oscillation expected. [51]

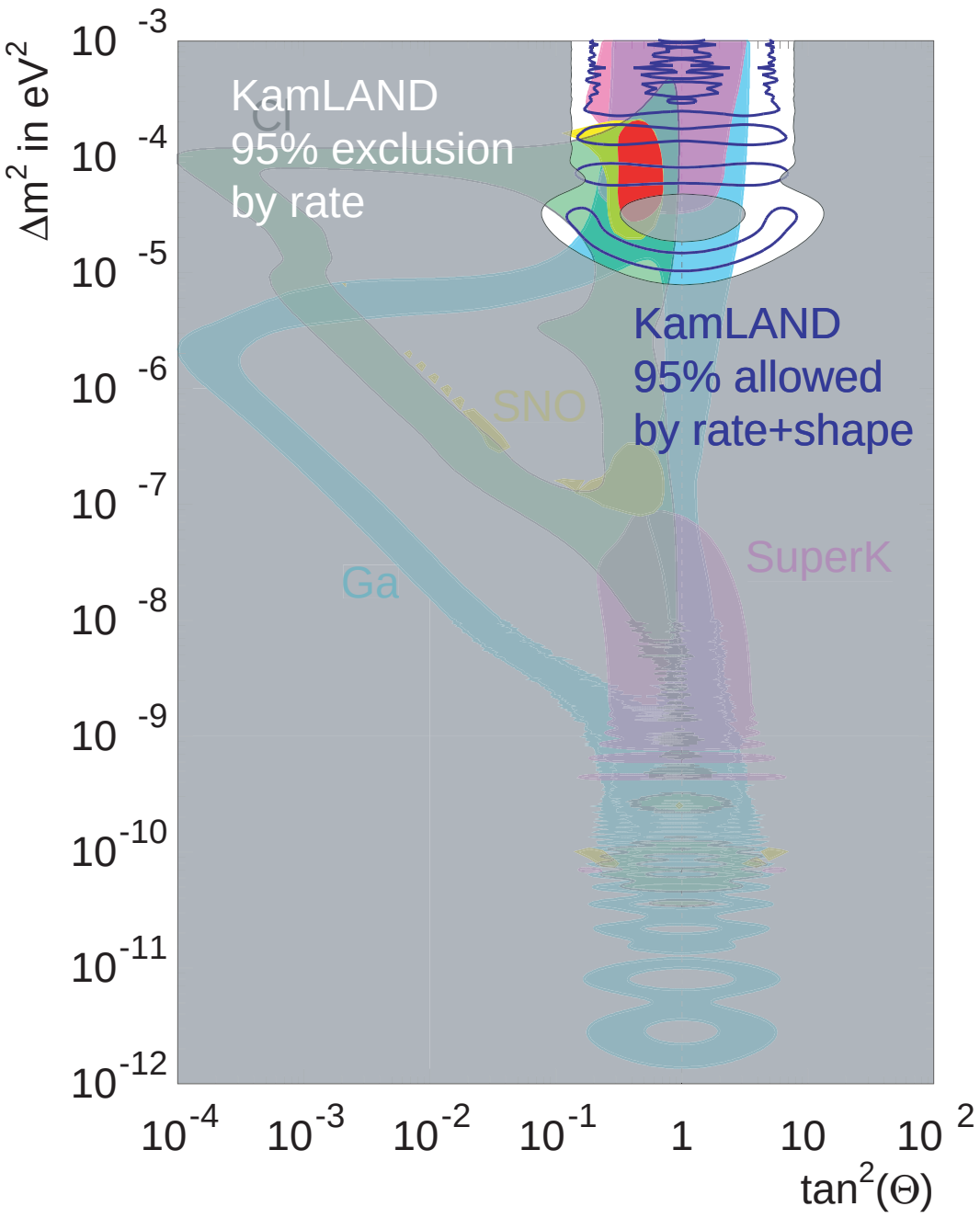

Figure 2.5: "Solar" oscillation parameter regions after KamLAND First Result. 95% CL allowed with Rate and Rate+Shape analysis [49]

2.4 Second Reactor Antineutrino Result

In the beginning of 2005 KamLAND published a more precise result on reactor antineutrino oscillation. This was obtained with substantially larger statistical base, detector hardware upgrade (enabling the 20" PMTs in the ID, some modifications to FEE boards) and newer analysis tools, allowing for much higher accuracy of the parameter evaluation.

During the work on the second $\bar{\nu}_e$ oscillation result, a new source of background has been found in the $^{13}C(\alpha, n)^{16}O$ reaction. This background is described in more detail in Chapter 6.3. Due to the relatively high analysis threshold of 2.6 MeV, this background has little effect on the reactor $\bar{\nu}_e$ oscillation parameters but is critical for terrestrial antineutrino studies.

Other improvements were based on better understanding of the detector and higher confidence in the new reconstruction tools and analysis methods. They included relaxing the radial selection cut from 500 to 550 cm (resulting in more than 30% increase of fiducial mass) and wider selection criteria for higher selection efficiency. The oscillation parameter evaluation was based on the analysis of $\bar{\nu}_e$ flux and energy spectrum, both integrated over time (**Rate+Shape** analysis).

During the two years of data taking, the reactor power in the plants surrounding KamLAND varied significantly, and so did the antieneutrino flux (Figure 2.6). This has been taken into account in the **Rate+Time** analysis. Although, theoretically, such analysis could test the geo-reactor hypothesis, KamLAND didn't prove to be sensitive enough to perform such a test at a considerable CL.

Due to small accuracy gains possible at that point the statistical analysis involving both the $\bar{\nu}_e$ flux and spectrum variation with time (**Rate+Shape+Time**) was *not* performed.

Figure 2.7 shows the expected original and oscillation-distorted $\bar{\nu}_e$ spectra and known sources of background. The observed signal shown in the same figure is in good agreement with the neutrino oscillation hypothesis.

The main result of that KamLAND study is presented in Figure 2.8. The allowed LMA region of "solar" oscillation parameters is split into three parts (bottom to top: LMA0, LMA1, LMA2), the central one (LMA1) being most favored by KamLAND data, in a good agreement with solar data. This plot actually shows the direction of further improvements. Of the two parameters, KamLAND is much more sensitive to the Δm^2, once the "alternative" LMA regions are excluded at sufficiently high CL. So the proof that the true value is indeed within LMA1 and its precise estimation within that area became one of the main goals of KamLAND experiment since then.

The splitting of the LMA area into several parts is an effect of the oscillatory nature of $\bar{\nu}_e$ flavor change and hence of the observed apparent disappearance. If the flux of reactor $\bar{\nu}_e$ neutrinos were monoenergetic and the sources were at the same distance from the detector then an infinite family of solutions would have been equally likely and thus indistinguishable in such experiments. However the actual reactor $\bar{\nu}_e$ spectra are continuous and, besides KamLAND detects antineutrinos from several reactors

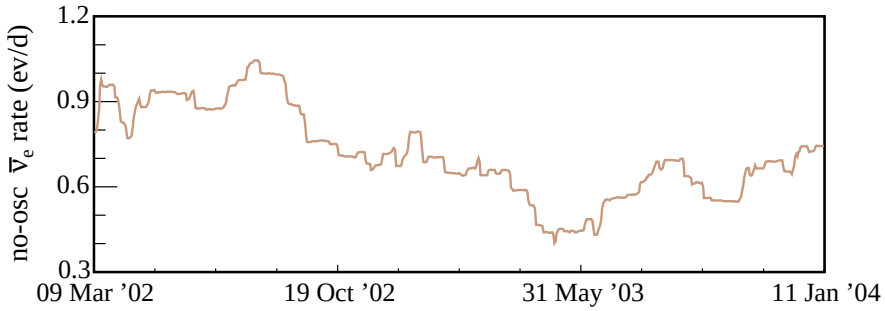

Figure 2.6: Time variation of the expected no-oscillation $\bar{\nu}_e$ flux at KamLAND. [52]

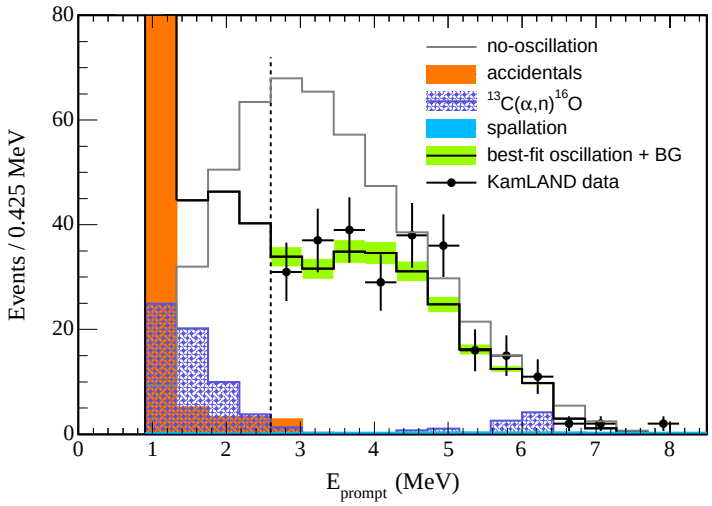

Figure 2.7: KamLAND Second Result antineutrino spectrum. Prompt energy spectrum with best-fit oscillation spectrum shown in solid black. The green bands indicate the systematic error. The grey histogram gives the unoscillated spectrum, the accidental spectrum is shown in orange, blue is spallation background (Section 6.2) and hatched light blue is the (α, n) background (Section 6.3). [52]

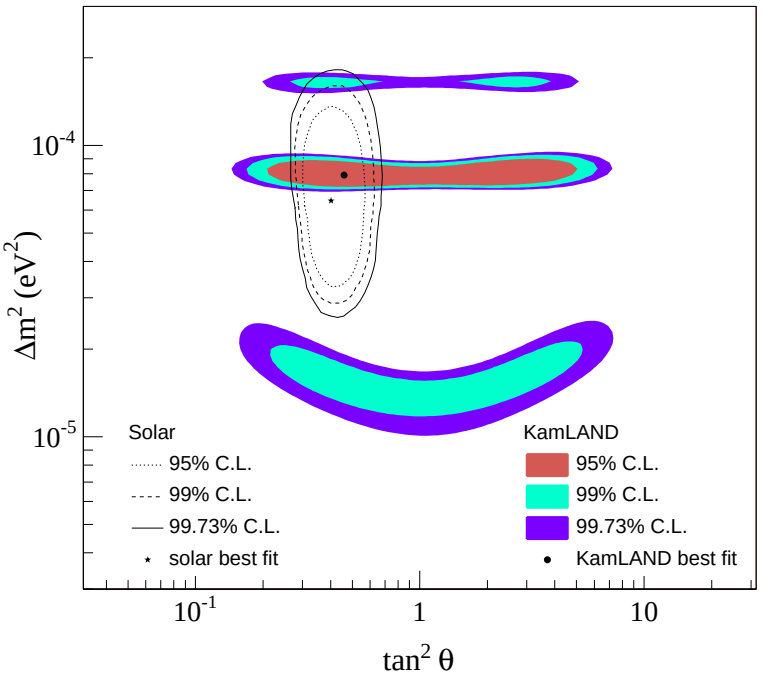

Figure 2.8: KamLAND reactor antineutrino oscillation Second Result. Confidence level bands for "solar" oscillation parameters, as determined by KamLAND. Best fit point is at $\Delta m^2 = 7.9 \times 10 - 5eV^2$ and $tan^2\theta = 0.46$. [52]

located at different distances. This decreases the accuracy with which oscillation parameters, especially Δm^2_{12} can be evaluated with a given number of events but allows to distinguish between the different solutions with the same oscillation "phase".

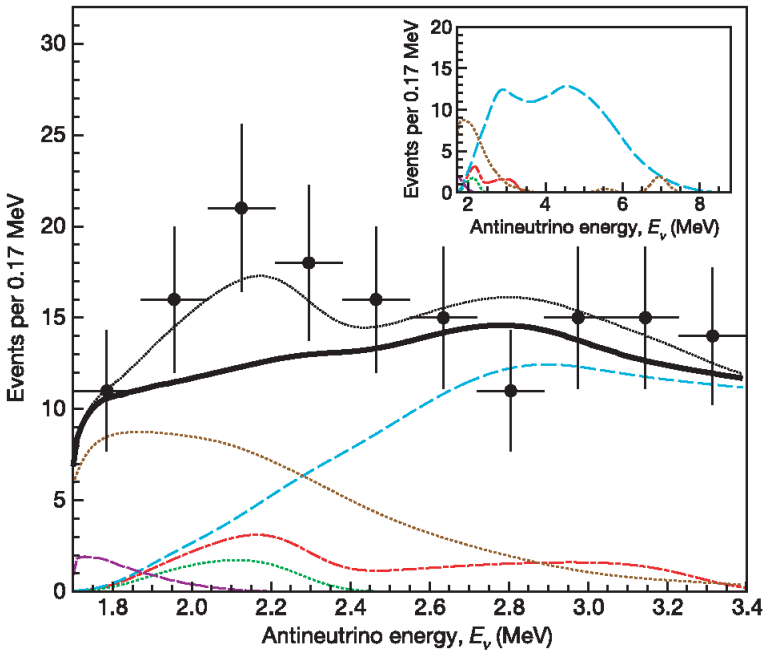

Figure 2.9: KamLAND terrestrial antineutrino spectrum with backgrounds. [48]

2.5 Observation of Geologically Produced Antineutrinos

In 2005, KamLAND reported the first evidence for the observation of geologically produced antineutrinos [48]. The presence of terrestrial antineutrinos in the data set has been proven through Rate+Shape analysis with precise evaluation of all backgrounds. Due to substantial backgrounding from $^{13}C(\alpha, n)^{16}O$ reaction and from the reactor antineutrinos (Figure 2.9), KamLAND is not very sensitive to the separation of ^{238}U and ^{232}Th components of the terrestrial signal. Because of that, the ratio between those components was fixed to 3.9, according the reference geophysical model [53] and the evaluation for the total antineutrino flux has been provided (Figure 2.10).

Due to the otherwise overwhelming accidental coincidence background, selection criteria for this study were similar to those used in the First Reactor Antineutrino Result rather than the Second one despite some detection efficiency loss. Energy selection cuts from 0.9 to 2.6 MeV in prompt visible energy were applied instead of 2.6 to 8.5 MeV to be sensitive to the terrestrial antineutrinos. This corresponds approximately to the real $\bar{\nu}_e$ energy below 3.4 MeV. Rate-only and Rate+Shape analysis methods were used in that study.

The total number of antineutrino candidates in the terrestrial antineutrino selection window was 152, 127 $\pm$ 13 of which are estimated to be background events. The best fit for the total terrestrial antineutrino flux is $51^{+3.9}_{-3.6}$ TNU (Terrestrial Neutrino Units, terrestrial $\bar{\nu}_e$ events per 10^{32} target protons per year).

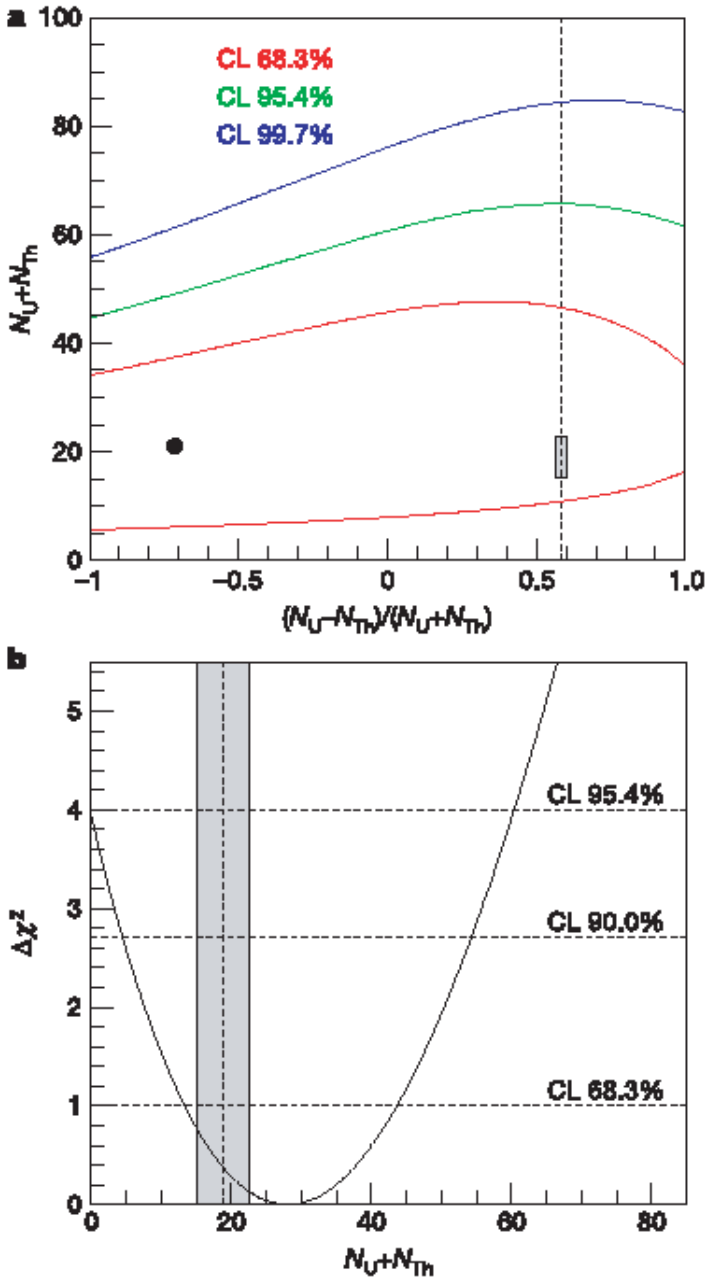

Figure 2.10: KamLAND terrestrial antineutrino parameter allowed ranges. [48]

At 99% CL, the upper limit for the total terrestrial flux is 145 TNU, which, according to the reference model, corresponds (within the considered Earth model) to 60 TW of total radiogenic power from just those two components. Since this is considerably higher than the 30-40 TW of total heat flux from the Earth, such an estimation does not allow exclusion of any reasonable geological model at this point.

A better sensitivity to the terrestrial antineutrino flux can be achieved by the combination of

- detector purification in order to reduce the amount of the $^{13}C(\alpha, n)^{16}O$ and accidental backgrounds;
- longer observation times;
- more sophisticated analysis methods to reduce the statistical uncertainty at given exposition.

Currently, the KamLAND detector is being purified to remove the residual radioactivity caused by ^{210}Pb and ^{85}Kr and other radioactive nuclei still present in the scintillator and, possibly, the balloon. If the process is successful, the $^{13}C(\alpha, n)^{16}O$ background will be essentially gone and the reduced accidental rates will allow the use of much more relaxed cuts for terrestrial antineutrino studies.

At the same time, a more advanced analysis actually enables to considerably improve the accuracy of the antineutrino flux evaluation even before the purification, which is presented in this thesis.

2.6 Motivation for Combined Analysis

The motivation for the combined antineutrino analysis is two-fold. On one hand, the $\bar{\nu}_e$ oscillation parameters can be determined more precisely by the inclusion of the low-energy range below 2.6 MeV. Both the ability to distinguish between the LMA0,1,2 areas and to find a precise evaluation of Δm^2 within LMA1, should it prove to be the true solution, depend on the antineutrinos with energies below 2.6 MeV. Ignoring them by the 2.6 MeV energy threshold is as good as throwing away up to 40% of the relevant experimental data.

On the other hand, the selection criteria previously used for terrestrial antineutrino studies had been very tight, which also led to less than optimal selection efficiency. If it were possible to use "reactor-like" loose selection cuts for terrestrial antineutrinos, the number of candidates could have almost doubled for a given observation period. Due to the amount of accidental background (Section 6.1), this definitely could not be done in a straightforward manner. However the differential approach to KamLAND data likelihood evaluation developed in this work made it possible to perform such an analysis.

An additional source of improvement is a more comprehensive use of timing information than had been done before. As was mentioned, in the Second oscillation

result, KamLAND used Rate+Time analysis and Rate+Shape analysis separately. Performing the simultaneous Rate+Shape+Time analysis provides a more accurate estimation for oscillation parameters but, for technical reasons, is more challenging. The implementation of computationally efficient Rate+Shape+Time parameter fitting procedure was also one of the goals of this work.

Chapter 3

Event Reconstruction

3.1 Waveform Analysis

After DAQ and Event Building (Section 2.2) all data about events has a form of digitized ATWD waveforms (one waveform per PMT that was hit in the event), which is not convenient for further analysis. Of physical interest are not the waveforms themselves but the information about the photoelectrons that generated them, namely the number of photoelectrons per PMT, the times of their arrival and the PMT coordinates. The number of photoelectrons is essential for energy reconstruction and the timing – for vertex fitting. PMT response resolution does not permit exact determination of the number of photoelectrons; instead the waveform's integral (called "charge") is evaluated as a representative of this number, which is not integer unlike the physical number of photoelectrons. The first stage of KamLAND data analysis takes the raw waveforms and converts them into much more compact time and charge data. It is called the "TQ" stage.

A TQ algorithm normally consists of two parts: time and charge estimation. Charge estimation is, in principle, rather straightforward. The waveform integral is proportional to the sum of sample values comprising this waveform. Time estimation is not so obvious because it is uncertain which sample is to be taken as the reference: the first sample belonging to the waveform, the one with maximum value (i.e. the peak), some sample in between or even some function of a subset of samples. One of the main requirements to TQ algorithms is good time resolution, so for a fixed signal timing the time returned by the TQ algorithm should have the narrowest spread possible. Time resolution is limited by the physical properties of the PMTs, (the transition time spread of 17" PMTs is measured to be slightly above 1.5 ns), but a TQ algorithm always introduces additional smearing, and this theoretical limit can never be reached in real data analysis.

KamLAND practically uses two different TQ algorithms that yield comparable time resolution (around 2.5 ns, for single photo electron waveforms on 17" PMTs). One uses the peak time of a smeared waveform as reference, which it fits with a second

order polynomial. The other considers the start of the waveform as such a reference and calculates the first, second and third order derivatives of the smeared waveform to find its precise position. This work is done mostly within the Tohoku University's KAT (KamLAND Analysis Toolkit), so it uses the latter TQ approach standard for that toolkit.

Although more sophisticated TQ algorithms with appreciably better time resolutions have been developed later, they have not been adopted, partly because of the amount of re-tuning associated with a TQ algorithm change. Waveform to TQ conversion is the lowest level of data analysis and its modifications are the most expensive since it affects all the higher level stages.

The cases when one PMT gets several photoelectrons separated in time are treated in a special way. The TQ algorithms are usually able to resolve several peaks unless they are too close to each other. The integral of the resulting multi-peak waveform is a good approximation for the total charge and hence still a valid evaluator for the number of photoelectrons. However, due to the electrical properties of PMTs and electronics, the timing accuracy is good only for the first pulse. Because of that, the time of only the first peak is normally considered (in particular, for vertex finding). The following peaks, if any, contribute to the total charge and participate in the energy reconstruction but their timing is, although available, rarely used.

3.2 Muon Tracking

If an event is recognized as a muon event, a muon fitter is used to reconstruct it. One of the two following conditions is sufficient to qualify an event as due to a muon:

- Total charge in 17" PMTs of ID $\geq$ 10000 photoelectrons ($\sim$ 30 MeV)
- Total charge in PMTs of ID $\geq$ 500 photoelectrons **and** the number of PMT hits in OD is $\geq$ 5

When this happens, a muon fitter is called to reconstruct an event. Muon tracking in a LS is a challenging task because light is generated by both the Cherenkov effect and scintillation, the latter being isotropic. The muon fitter procedure developed at RCNS of the Tohoku University takes advantage of the fact that the speed of the muon is close to the speed of light in the vacuum. In that case, the trajectory of the scintillation photon that hits a PMT first is the same as that of a Cherenkov photon hitting the same PMT. The scintillation photons that may hit this PMT from other directions must arrive later.

The fitter returns the information about the entrance point, the direction of muon and the quality of the reconstruction. If the latter is not good enough, special measures are taken. In particular, the veto cuts are widened.

A more detailed description of the muon fitter and its operation can be found in [53].

3.3 Energy Reconstruction

Different approaches to energy estimation are possible and have been successfully used by KamLAND. The energy estimation can be based on the total charge of ID PMTs, on the pattern of PMT hits (the charges being totally ignored), or combine both sources of information about the energy of the signal. The charge-based energy fitters tend to be simpler and normally perform better in the relatively high energy area but have a relatively poor energy resolution for events below 1 MeV. Hit-based fitters offer substantially better accuracy in the lower energy area but become comparable to charge-based energy fitters and around 2 MeV and worse at higher energies. Besides, they are harder to develop and tune.

A technically better approach is to combine both hit and charge pattern information in a seamless framework. If done properly, this "combined" approach is guaranteed to outperform both purely hit-based and purely charge-based algorithms in the whole energy range because the hit-based and the charge-based energy reconstruction can be seen as extreme cases of a more general multitude of possible estimators. The only disadvantage of this method is that it is even harder to implement, tune and validate than the purely hit-based estimator.

This work uses a charge based energy estimator developed at the Tohoku University and standard for KAT. Its principle, performance and calibration are described in much more detail in [53].

The energy fitter offers the resolution of $6.2\% \times \sqrt{E_{vis}[MeV]}$ with both 17" and 20" PMT's on and $7.25\% \times \sqrt{E_{vis}[MeV]}$ with 17" PMT's only.

3.4 Vertex Reconstruction

Vertex reconstruction can be based on PMT hit pattern, PMT charge pattern and PMT hit timing. All three approaches have been tested in KamLAND, as well as some combinations of those. Owing to the properties of KamLAND PMT's and the size of the detector, of the three "pure" methods, time-based vertex reconstruction provides by far the best results. "Combined" methods can, theoretically, yield a small improvement over a time-based reconstruction but the complexity overhead has been too high to develop an optimally operating vertex fitter based on hit and timing or hit and charge information.

This work uses a newly developed time-based vertex fitter, "V2". Unlike other event reconstruction tools, it has not been covered in the earlier KamLAND publications or theses, so its description can be found in Appendix A.

The fitter provides the vertex resolution of $12.1cm/\sqrt{E_{vis}[MeV]}$ with 17" and 20" PMT's and $12.5cm/\sqrt{E_{vis}[MeV]}$ with 17" only for each of the three axes, X, Y, and Z.

Chapter 4

Reactor Antineutrinos

4.1 Reactors around KamLAND

Nuclear reactors of Japanese power plants are the primary source of antineutrinos for KamLAND studies. The combined thermal power of this source of neutrinos is above 200 GW. Nuclear reactors from other countries do contribute to the total $\bar{\nu}_e$ flux at KamLAND site but since the flux falls off as the inverse square of distance, their contribution to the total flux is quite small.

Oscillation parameter studies require the knowledge of the following parameters:

- Distances to the reactors (also called baselines);
- Initial (non-oscillated) $\bar{\nu}_e$ spectrum at every point in time, for each reactor or reactor site.

These parameters are either known or provided to KamLAND collaboration by the power companies with sufficient accuracy, which makes the commercial reactors a convenient and powerful source of antineutrinos, with well known relevant characteristics.

The distances to reactors enter the oscillation picture in two aspects. First, as was just mentioned, the flux from a reactor falls with the distance to that reactor. Second, the oscillation length is directly connected with the difference of squared mass eigenstates (1.18) , one of the key parameters KamLAND was designed to measure.

Because they are well known in terms of intensities, spectra and distances, the sources of reactor antineutrinos constitute an excellent tool for oscillation parameter studies used in KamLAND.

The case easiest for analysis and the best one in terms of attainable accuracy would be when all reactors are located at exactly the same distance from the detector. This is certainly not the case since there is no point in space equidistant to all power plants. Nevertheless KamLAND location is very fortunate indeed. Most of the flux comes from rather similar distances, so that the oscillation pattern from one site does not smear much that from another site (Figure 4.1). Sometimes an "average baseline" of

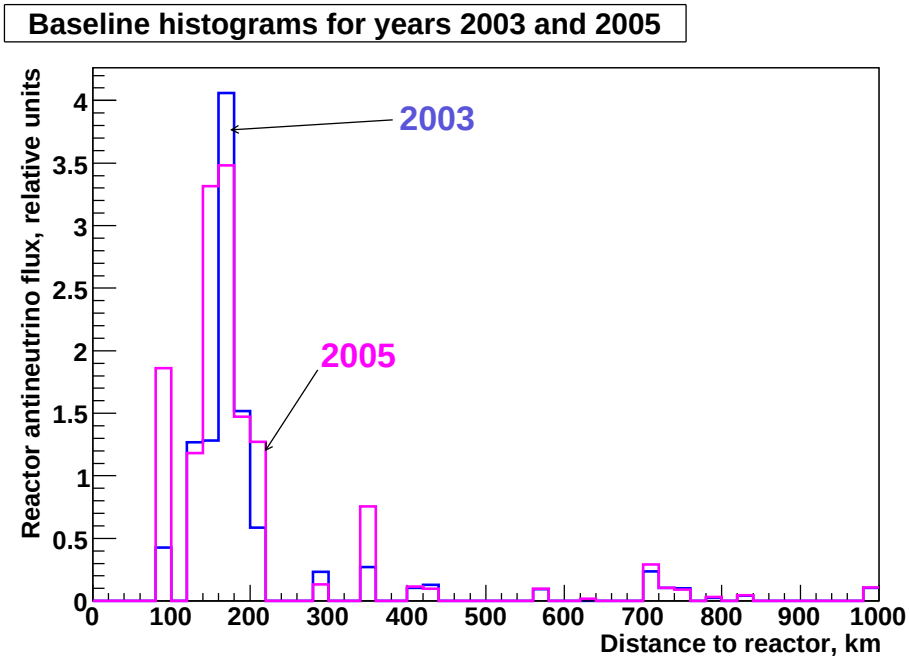

Figure 4.1: Baseline distribution of the expected $\bar{\nu}_e$ flux at KamLAND for years 2003 and 2005. Note the substantially increased component below 100 km for the later period of observation.

180 km is quoted in reference to KamLAND. Strictly speaking, this is not correct. There is no way to reduce the oscillation pattern from several sources located at different distances to that of a single, "average" source located at some "average" baseline. Yet, if the main sources are clustered around some single distance, this approximation may be valid for draft estimations. In case of KamLAND, all actual calculations referring to reactor $\bar{\nu}_e$ oscillations are performed with exact distances to particular reactors and no "average baseline" approximation is used.

Figure 4.1 reveal yet another potential problem: the baseline pattern changes with time. Ignoring this change leads to the loss in the accuracy in the oscillation parameter determination. The bigger the change in the pattern, the greater the loss. For short periods of observations the changes were small but over about 4 years of exposure some reactors have been temporarily shut down; some new reactors have been built. The implementation of "Rate+Shape+Time" analysis was one of the distinctive features of the analysis presented here that allowed for its better accuracy.

4.2 Reactor Antineutrino Components

There are 4 principal fissionable isotopes in power plant reactors: ^{235}U, ^{238}U, ^{239}Pu, ^{241}Pu. Upon a neutron capture, these isotopes split, initiating decay sequences.

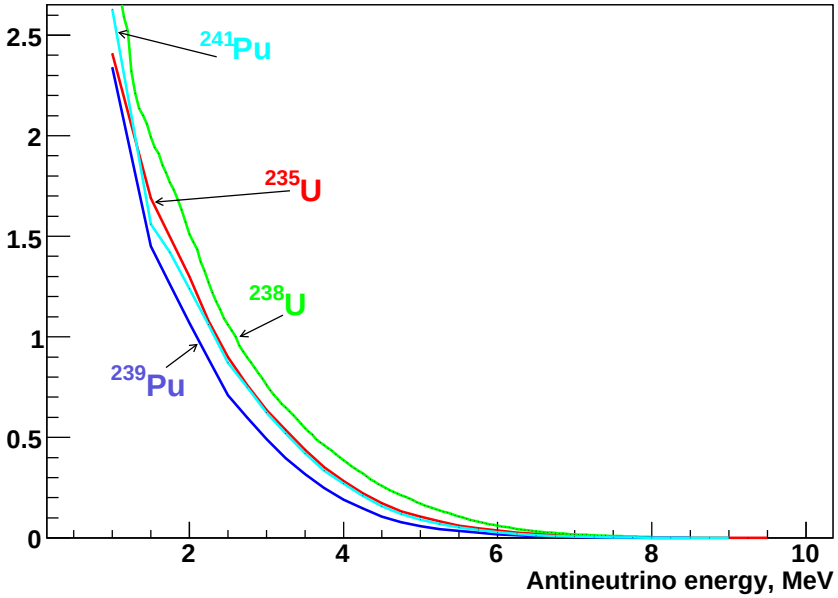

Figure 4.2: Reactor antineutrino energy spectra for ^{235}U, ^{238}U, ^{239}Pu and ^{241}Pu fissions, $\bar{\nu}_e$ per MeV per fission. [54], [55], [56]

Short-living isotopes in those sequences β-decay, effectively producing 4-7 $\bar{\nu}_e$ particles per initial fission. Not all such antineutrinos have energy above the detection threshold. The $\bar{\nu}_e$ energy spectra for the fissions of ^{235}U and ^{238}U are provided by [54] and [55], respectively. The $\bar{\nu}_e$ spectra for ^{239}Pu and ^{241}Pu fissions can be found in [56] The plots of those spectra are shown in Figure 4.2.

A small but not completely negligible addition to the reactor $\bar{\nu}_e$ flux comes from long lived isotopes in fission products. Due to their relatively long life time they are stored on the reactor sites. Their concentration as a function of time does not match its counterpart for the main fission isotopes, so they must be treated separately. Of six isotopes listed in [57], three live long enough to require a separate treatment. These are ^{144}Ce, ^{106}Ru, ^{90}Sr. Their spectra are substantially "softer" than that of the fission-produced antineutrinos and more resembles the terrestrial antineutrino spectrum (Section 5.2). In fact the presence of long-lived isotopes affect the terrestrial antineutrino studies more than the reactor-based oscillation studies. However they are localized at the sites of the reactors, so their oscillation pattern is exactly the same as that of the four main reactor $\bar{\nu}_e$ components, so, technically speaking, they are a kind of reactor antineutrinos.

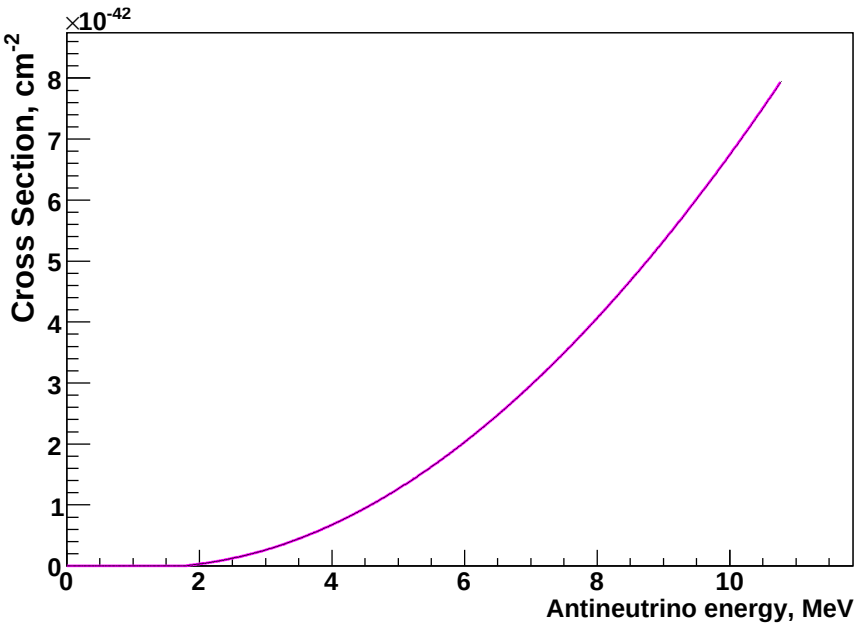

Figure 4.3: Cross section of the inverse beta decay reaction as a function of $\bar{\nu}_e$ energy.

4.3 Inverse Beta Decay Cross Section

Knowing the antineutrino flux at the reactor site and the number of target protons is not enough to evaluate the $\bar{\nu}_e$ detection rate and its energy dependence. The cross section of the reaction (1.1) does depend on the antineutrino energy and, generally, on the angle of the resulting positron direction with respect to the direction of the incident antineutrino. The cross section can be calculated theoretically [58]. The angular dependence is small and, combined with relativistic kinematics of the inverse beta decay, results in some smearing of the response energy.

The dependence on the $\bar{\nu}_e$ energy is much more substantial. Since (1.1) is a threshold reaction, its cross section is zero below the 1.8 MeV threshold. For higher values of $E_{\bar{\nu}_e}$ energies quickly grows (Figure 4.3). Because of that dependence, the shape of the observed $\bar{\nu}_e$ energy spectrum even in the absence of oscillations is quite different from the "raw" energy spectrum of reactor antineutrinos . Figure 4.4 shows such spectra for the four fissionable isotopes expressed in arbitrary units but normalized for the average abundance of the ^{235}U, ^{238}U, ^{239}Pu and ^{241}Pu fissions in typical reactors. Because fissions of ^{235}U are most common, they produce most $\bar{\nu}_e$ and their contribution to the antineutrino spectrum is dominant.

Figure 4.5 provides the detected reactor antineutrino shapes for their "fission" and "long-lived isotope decay" components separately as well the overall spectrum. The "long-lived isotope decay" part is visible in the lowest energy part but is a small correction, anyway.

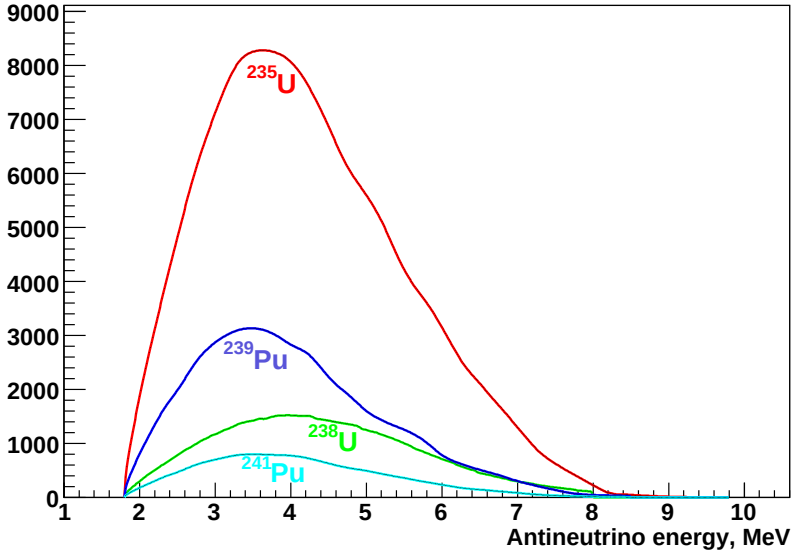

Figure 4.4: No-socillation detection energy spectra for neutrinos from fissions of ^{235}U, ^{238}U, ^{239}Pu and ^{241}Pu. Relative frequency of the fissions of different isotopes is taken into account.

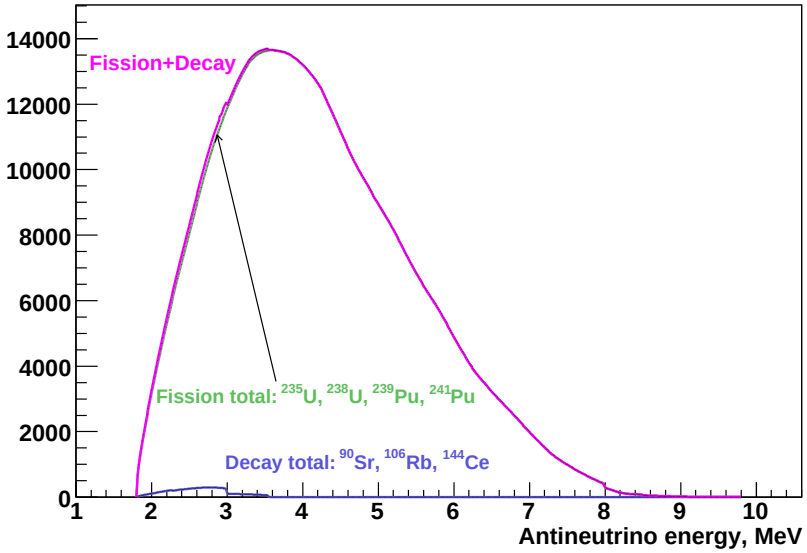

Figure 4.5: Cumulative no-oscillation detection energy spectra for reactor $\bar{\nu}_e$. "Fission" antineutrinos are actually from β-decays of short living fission products; "decay" antineutrinos are from the decays of long-living fission products. Relative frequency of the fissions and decays of different isotopes is taken into account.

4.4 Spectrum Distortion

The "disappearance" of electron antineutrinos, i.e. the smaller amount of $\bar{\nu}_e$ events detected, compared to the no-oscillation expectation can be measured with a fairly good accuracy. However the integrated event deficit measurement, no matter how precisely it can be done, yields only one parameter, the ratio of observed to expected events. This doesn't allow for a precise oscillation study when more than one unknown parameter is involved. In case of KamLAND, there are at least two unknown parameters, θ_{12} and Δm^2_{12}. In fact much more oscillation information comes through the spectrum distortion. It's the good sensitivity to $\bar{\nu}_e$ energy that makes KamLAND such a powerful tool for oscillation studies.

The distortion of the observed $\bar{\nu}_e$ spectrum is caused by the $\bar{\nu}_e$ "disappearance", i.e. their oscillation to the weak interaction states not detectable through the inverse beta decay. Since the antineutrino energy explicitly enters the expression for $P(\bar{\nu}_e \rightarrow \bar{\nu}_e)$ (1.19), the deficit of observed $\bar{\nu}_e$ is, generally, not uniform across their energy spectrum. The distortion depends on the baseline and the neutrino oscillation parameters. Since the baseline is known, the precise evaluation of those parameters is possible with energy spectrum measurement.

For KamLAND, the expected spectrum distortion for some different combinations of oscillation parameters is presented in Figure 4.6. Note the importance of the energy spectrum shape studies. The oscillation patterns for the four combinations yield about the same overall number of detected antineutrinos and are indistinguishable by means of Rate-only analysis. Yet, they describe completely different physics. In particular, the Δm^2_{12} differs by more than an order of magnitude. However the resulting spectrum shapes are quite different as well, which can be tested by methods of binless spectrum analysis described in Chapter 7.

There is another important point about the character of spectrum distortion due to $\bar{\nu}_e$ oscillations. The plots in Figure 4.6 look so unlike each other that one may think that the changes in oscillation parameters may cause almost arbitrary distortion to the observed spectrum. Actually they can not. The distortions due to oscillation are still just disappearances. The oscillations can "suppress" one energy range more than another but not transfer the events between the ranges. The spectrum distortions are "vertical", not "horizontal". In other words, anineutrinos of E_1 energy bin "know" nothing about the occupancy of E_2 bin if $E_1 \neq E_2$. To be exact, there is some amount of "horizontal" exchange due to recoil smearing of the inverse beta decay reaction and the finite energy resolution of the detector but this is totally external to neutrino oscillations. This strictly "vertical" nature of oscillation-related spectrum distortion is a very substantial constraint which has been used in this study to simplify the calculations.

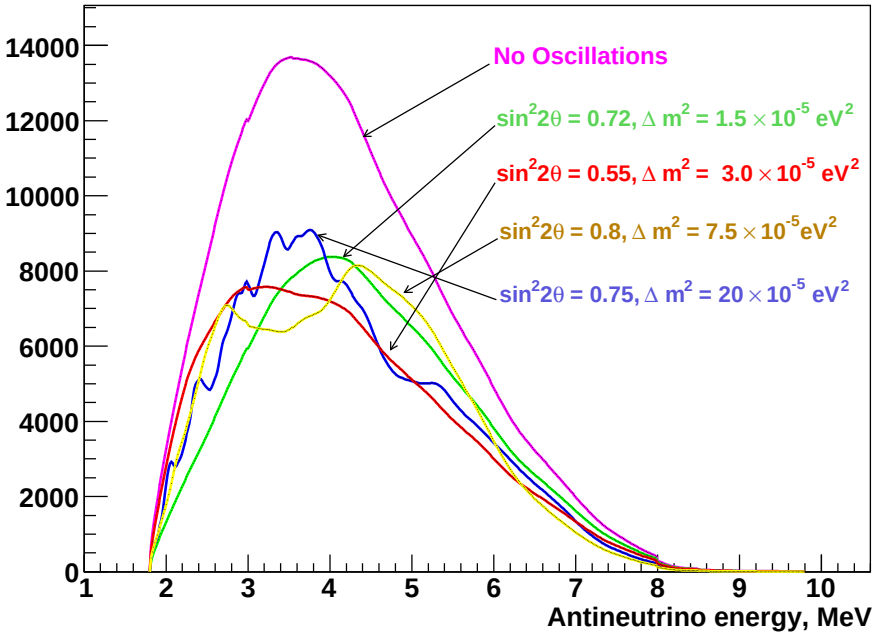

Figure 4.6: Reactor $\bar{\nu}_e$ Energy Spectrum Distortion. No-oscillation case and several combinations of "solar" neutrino oscillation parameters. Note that all oscillation affected spectra would have the same Rate.

4.5 Instantaneous Spectrum Calculation

The calculation of the expected $\bar{\nu}_e$ energy spectra is in fact a rather challenging problem for purely technical reasons. There are tens of reactors that contribute substantially to the antineutrino flux at KamLAND, all located at different distances, each having a unique composition of the nuclear fuel and hence the unique antineutrino spectrum, which, in addition, is changing in time.

The final statistical analysis involves the expected $\bar{\nu}_e$ spectrum calculation at every instance of oscillation parameter change. To be sensitive to oscillation parameters, the spectra must be evaluated with sufficient accuracy, normally at hundreds of points. When those hundreds are multiplied by the tens of reactor sites the problem gets quite demanding for CPU resources since finding the best fit point involves hundreds to thousands of such evaluations and must be repeated at every combination of the main parameters (in case of oscillation studies, Δm_{12} and θ_{12}). The requirement of full Rate+Shape+Time analysis makes matters even worse since one more dimension is added to the problem: the spectra need to be evaluated for every day separately.

A solution for that problem has been found during the work on this thesis, which eliminates the need for the run-time summation of the reactor fluxes and removes at

least one dimension from this problem. The algorithm is based on the pre-calculation of oscillation disappearance patterns and is described in Appendix C.

Chapter 5

Terrestrial Antineutrinos

5.1 Sources of Terrestrial Antineutrinos

As was mentioned above, the source of terrestrial antineutrinos (geo-neutrinos, for short) are the naturally occurring radioactive isotopes. However not all unstable isotopes are sources of detectable antineutrinos. In fact the conditions for an isotope to be such a source are quite restricting.

First of all, the immediate sources of antineutrinos are β^--decays only. Other common nuclear reactions, such as α-decays, deexcitations with γ emission don't produce neutrinos or antineutrinos. β^+-decays produce neutrinos but these are not detectable with the inverse beta reaction on electrons. Second, not all β^--decays produce antineutrinos with sufficient energy. In fact the threshold of the reaction 1.1 of 1.8 MeV is quite high when considered in the context of long living isotope decays. The majority of the known beta decays isotopes have Q-values lower than that. Third, the source of sufficiently energetic antineutrinos must be abundant enough to provide a practically detectable antineutrino flux.

In fact the two last requirements are rather conflicting. Although there is no one-to-one correspondence between Q-values and lifetimes, isotopes with highly energetic decays tend to be short-lived. As a result, they have all decayed away during the life time of the Earth, and naturally found only in trace amounts if any at all. There are extremely long living β^--decaying isotopes that are still substantially present in the core of the Earth. The list of such isotopes is provided in Table 5.1. Q-values for all those β^--decays is below the inverse beta decay threshold, which excludes the observation of corresponding antineutrinos with this technique. Of those beta-decaying isotopes, ^{40}K is most abundant and should be a substantial source of antineutrinos but its observation will require the construction of new and probably specialized detectors exploiting detection techniques other than the inverse beta decay used in KamLAND.

Fortunately for geo-neutrino studies, radioactive isotopes do not necessarily decay directly into stable states. Actually the products of most decays are radioactive

Table 5.1: Naturally occurring long-living β^--decaying isotopes with stable products. No β^--decay has enough energy to produce antineutrinos above the inverse beta decay detection threshold.

Isotope	Decay Mode	Half Life	Q-value, MeV	Decay Product
^{40}K	$89.28\%\beta^-$ / $10.72\%EC$	1.277×10^9y	1.31109 / 1.5042	^{40}Ca / ^{40}Ar
^{87}Rb	β^-	4.75×10^{10}y	0.2833	^{87}Sr
^{138}La	$66.4\%EC$ / $33.6\%\beta^-$	1.05×10^{11}y	1.738 / 1.044	^{138}Ba / ^{138}Ce
^{176}Lu	β^-	3.78×10^{10}y	1.1929	^{176}Hf

themselves. If a decay starts with a relatively long-living isotope, followed by much shorter-lived products, a decay series (often referred to as "decay chain") forms. After undergoing up to tens of α- and β-decays the decay series finally ends in a stable isotope. Most intermediate products are much shorter-lived than the "parent" nuclides and often have higher Q-values for their decays. This potentially offers better opportunities for terrestrial geo-neutrino studies. Even if such an intermediate β^- decaying isotope is too short lived to survive in considerable quantities by itself, there is a source of those isotopes in the decays of longer-lived chain members located above in the series.

Since each α-decay decreases the nuclear mass number by four and β-decays don't change it at all, the number (A Mod 4) is invariant for the whole chain. Correspondingly, the possible decay chains can be described by this invariant number and there are four of them.

- Decay chain with $A = 4n$ starts with ^{232}Th isotope and is called Thorium Chain (Table 5.2).
- Decay chain with $A = 4n+1$ starts with ^{237}Np isotope and is called Neptunium Chain (Table 5.4).
- Decay chain with $A = 4n + 2$ starts with ^{238}U isotope and is called Radium Chain (Table 5.3).
- Decay chain with $A = 4n + 3$ starts with ^{239}Pu isotope and is called Actinium Chain (Table 5.5).

Note that the presence of β^--decays with Q-value above 1.8 MeV is a necessary but not a sufficient condition for the $\bar{\nu}_e$ energy spectrum to reach the inverse beta decay detection threshold. The β^--decay can go to the excited state of the daughter nucleus, in which case only a fraction of the whole Q-value is available to be distributed among the β^--decay products. The rest of it is emitted with a gamma. An example here is the β^--decay of ^{234}Pa in the Radium decay chain (Table 5.3). The lowest energy

Table 5.2: Thorium Decay Series. Q-values for the transitions that lead to antineutrinos detectable through inverse beta decay are in **bold**.

Isotope	Decay Mode	Half Life	Q-value, MeV	Decay Product
^{232}Th	α	1.405×10^{10}y	4.081	^{228}Ra
^{228}Ra	β^-	5.75y	0.046	^{228}Ac
^{228}Ac	β^-	6.25h	**2.124**	^{228}Th
^{228}Th	α	1.9116y	5.520	^{224}Ra
^{224}Ra	α	3.6319d	5.789	^{220}Rn
^{220}Rn	α	55.6s	6.404	^{216}Po
^{216}Po	α	0.145s	6.906	^{212}Pb
^{212}Pb	β^-	10.64h	0.570	^{212}Bi
^{212}Bi	64.06%β^- / 35.94%α	60.55min	**2.252** / 6.208	^{212}Po / ^{208}Tl
^{212}Po	α	299ns	8.955	^{208}Pb (stable)
^{208}Tl	β^-	3.053min	**4.999**	^{208}Pb (stable)

Table 5.3: Radium Decay Series. Q-values for the transitions that lead to antineutrinos detectable through inverse beta decay are in **bold**.

Isotope	Decay Mode	Half Life	Q-value, MeV	Decay Product
^{238}U	α	4.468×10^{9}y	4.270	^{234}Th
^{234}Th	β^-	24.10d	0.273	^{234}Pa
^{234}Pa	β^-	6.70h	2.197	^{234}U
^{234}U	α	245500y	4.859	^{230}Th
^{230}Th	α	75380y	4.770	^{226}Ra
^{226}Ra	α	1602y	4.871	^{222}Rn
^{222}Rn	α	3.8235d	5.590	^{218}Po
^{218}Po	99.98%α/0.02%β^-	3.10min	6.615/0.265	^{214}Pb/^{218}At
^{218}At	99.90%α/0.10%β^-	1.5s	6.874/**2.883**	^{214}Bi/^{218}Rn
^{218}Rn	α	35ms	7.263	^{214}Po
^{214}Pb	β^-	26.8min	1.024	^{214}Bi
^{214}Bi	99.98%β^-/0.02%α	19.9min	**3.272**/5.617	^{214}Po/^{210}Tl
^{214}Po	α	0.1643ms	7.883	^{210}Pb
^{210}Tl	β^-	1.30min	**5.484**	^{210}Pb
^{210}Pb	β^-	22.3y	0.064	^{210}Bi
^{210}Bi	99.9999%β^-/0.0001%α	5.013d	1.426/5.982	^{210}Po/^{206}Tl
^{210}Po	α	138.376d	5.407	^{206}Pb (stable)
^{206}Tl	β^-	4.199min	1.533	^{206}Pb (stable)

Table 5.4: Neptunium Decay Series. Q-values for the transition that lead to antineutrinos detectable through inverse beta decay is in **bold**.

Isotope	Decay Mode	Half Life	Q-value, MeV	Decay Product
^{241}Pu	β^-	14.4y	0.021	^{241}Am
^{241}Am	α	432.7y	5.638	^{237}Np
^{237}Np	α	2.14×10^6y	4.959	^{233}Pa
^{233}Pa	β^-	27.0d	0.571	^{233}U
^{233}U	α	1.592×10^5y	4.909	^{229}Th
^{229}Th	α	7.54×10^4y	5.168	^{225}Ra
^{225}Ra	β^-	14.9d	0.36	^{225}Ac
^{225}Ac	α	10.0d	5.935	^{221}Fr
^{221}Fr	α	4.8min	6.3	^{217}At
^{217}At	α	32ms	7.0	^{213}Bi
^{213}Bi	α	46.5min	5.87	^{209}Tl
^{209}Tl	β^-	2.2min	**3.99**	^{209}Pb
^{209}Pb	β^-	3.25h	0.644	^{209}Bi
^{209}Bi	α	1.9×10^{19}y	3.14	^{205}Tl (stable)

Table 5.5: Actinium Decay Series. No decays generate antineutrinos detectable through inverse beta decay reaction.

Isotope	Decay Mode	Half Life	Q-value, MeV	Decay Product
^{239}Pu	α	2.41×10^4y	5.244	^{235}U
^{235}U	α	7.04×10^8y	4.678	^{231}Th
^{231}Th	β^-	25.52h	0.391	^{231}Pa
^{231}Pa	α	32760y	5.150	^{227}Ac
^{271}Ac	$98.62\%\beta^-/1.38\%\alpha$	21.772y	0.045/5.042	$^{227}Th/^{223}Fr$
^{227}Th	α	18.68d	6.147	^{223}Ra
^{223}Fr	β^-	22.00min	1.149	^{223}Ra
^{223}Ra	α	11.43d	5.979	^{219}Rn
^{219}Rn	α	3.96s	6.946	^{215}Po
^{215}Po	$99.9998\%\alpha/0.0002\%\beta^-$	1.781ms	7.527/0.715	$^{211}Pb/^{215}At$
^{215}At	α	0.1ms	8.178	^{211}Bi
^{211}Pb	β^-	36.1min	1.367	^{211}Bi
^{211}Bi	$99.724\%\alpha/0.276\%\beta^-$	2.14min	6.751/0.575	$^{207}Tl/^{211}Po$
^{211}Po	α	516ms	7.595	^{207}Pb (stable)
^{207}Tl	β^-	4.77min	1.418	^{207}Pb (stable)

final state is the 948 keV excited state of ^{234}U, so the $\bar{\nu}_e$ antineutrino can at best get 1249 keV and can never be detected by inverse beta reaction.

The Actinium chain does not include β^--decays with over-threshold Q-values at all and can not be monitored with KamLAND or similar experiments. The Neptunium chain has one suitable β^- decay but is practically extinct now due to the relatively short life of the parent isotope, ^{237}Np. This leaves the Thorium and the Radium chains as the only sources of geo-neutrinos detectable with KamLAND. So, speaking about terrestrial antineutrino studies in the context of KamLAND experiment, we mean the detection of electron antineutrinos produced by the β^--decays marked in bold in Tables 5.2 and 5.3.

Although not in good agreement with nuclear physics naming conventions, neutrino geophysics pioneered by KamLAND often refers to antineutrinos from the Radium decay series as "Uranium" or "^{238}U" terrestrial antineutrinos by the name of the parent isotope of the series. The antineutrinos from the Thorium decay chain are called "Thorium" or "^{232}Th" terrestrial antieneutrinos, so there is no potential confusion here.

5.2 Terrestrial Antineutrino Spectrum

Terrestrial antineutrino spectra were calculated based on the known data for radioactive decays, available at The Isotopes Project of LBNL [59]. This study generally followed the approach developed by KamLAND collaborators [53] and [60] and provided a cross-check for the results obtained before, which the study [48] was based on. The resulting antineutrino spectra for the Thorium and the Radium serii is shown in Figure 5.1. For the reasons discussed above the $\bar{\nu}_e$ from the other two decay chains and from the decays of ^{40}K, ^{87}Rb, ^{138}La and ^{176}Lu are either almost non-existent or not detectable in KamLAND due to their sub-threshold energies. These spectra are not shown here.

Similarly to reactor antineutrinos, this spectrum does not reflect the actual detection rate as a function of $\bar{\nu}_e$ energy. To become representative of the expected observed spectrum, the cross section of the inverse beta reaction (Figure 4.3) must be taken into account. The resulting detected $\bar{\nu}_e$ energy spectra for the two relevant decay series is shown in Figure 5.2.

5.3 Goals of the Study

In their relation to KamLAND experiment, terrestrial antineutrinos are very different from reactor antineutrinos. The difference comes not from the physics of those particles themselves (the only distinctive feature being the "softer" energy spectrum) but rather from our knowledge about the corresponding sources. Whereas the sources of reactor antineutrinos are well known, we have no hard experimental data on the

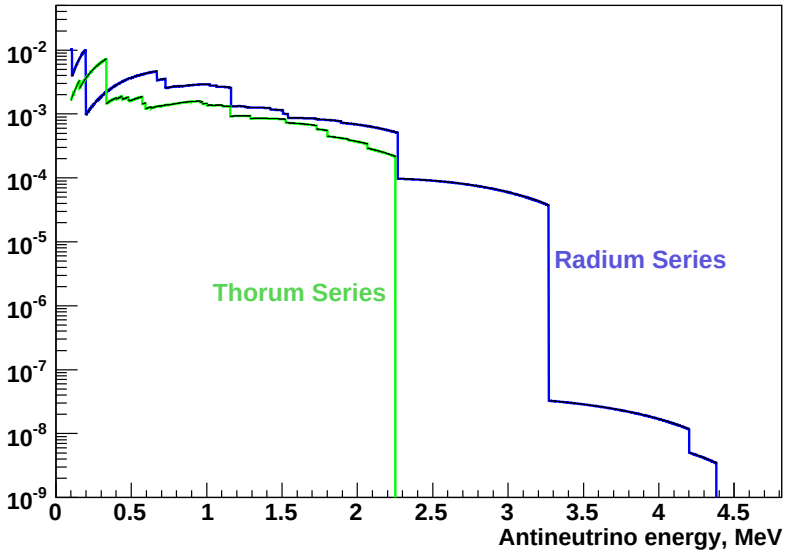

Figure 5.1: Antineutrino spectra from the Thorium and Radium decay series. Spectra are normalized for the same number of decays of parent nuclei, ^{232}Th and ^{238}U, respectively.

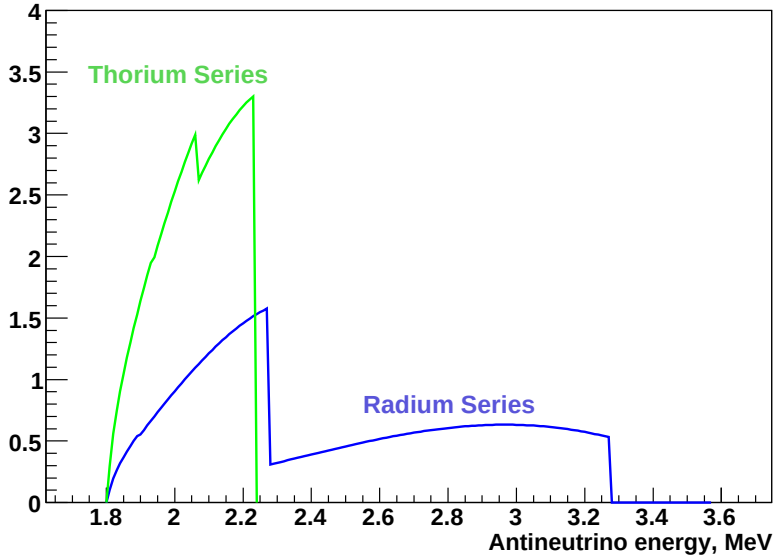

Figure 5.2: Detected terrestrial antineutrino energy spectra. The distributions for Thorium and Radium chains are normalized to 1. No experimental energy resolution applied.

sources of terrestrial antineutrinos. Instead, the main goal of geo-neutrino studies at KamLAND is to infer some information about those sources, their intensities and spatial distribution. The idea to use geologically produced antineutrinos to study the interior structure of the Earth was first proposed by Eder [61] and Marx [62] almost 40 years ago. However, due to the relatively small flux of the terrestrial antineutrinos no such studies were possible before KamLAND.

According to mainstream geological and geochemical models [63], [64] and rate of radiogenic heat release [65] the Thorium and Radium decay chains can produce about 16 TW, which is about 40-50% of total heat dissipated by the Earth [66], [67]. The number of decays is connected with the number of terrestrial antineutrinos, so the measurement of their flux offers an independent way to test the prediction of geological models, provided the necessary accuracy can be achieved. It should be noted though that there is no one-to-one correspondence between the antineutrino flux and the amount of radiogenic heat from terrestrial radioactive sources. In particular, Radium decay series produces much more detectable antineutrinos than Thorium series does, so the observed geo-neutrino flux can be a reliable estimation of the radiogenic heat only if the ^{238}U to ^{232}Th concentration ratio is known or can be measured.

The measurement of this ratio interesting in its own right and is, in principle, possible through antineutrino observations. Owing to the different energy spectra shapes of "Uranium" and "Thorium" geo-neutrinos, it is possible to statistically separate those components and estimate the relative concentrations of those isotopes in the core of the Earth.

To summarize the geo-neutrino studies that can be performed with KamLAND, two parameters can be directly determined in this experiment:

- Geo-neutrino flux from the Thorium series;
- Geo-neutrino flux from the Radium series,

or, equivalently,

- Total flux from both decay series;
- Balance between the contributions from the two series

The geophysical implications of such studies depend on the achievable accuracy of geo-neutrino flux estimations. If the estimation is precise enough, some models can be excluded or at least strongly disfavored, as long as the model does predict the concentration and distribution of ^{232}Th and ^{238}U isotopes.

After the observation of geo-neutrino signal in [48], the next obvious step is to confirm it at higher confidence level on one hand and, simultaneously, to bring the uncertainty of the upper limit to the point where the fully radiogenic hypothesis of the heat produced by the Earth can be tested.

5.4 Terrestrial Antineutrino Flux and Oscillations

Due to the small number of expected events for such a study, terrestrial $\bar{\nu}_e$ directionality measurement with KamLAND is practically impossible (Appendix B). What KamLAND can evaluate is the flux as a function of energy. This flux from each decay series can be expressed as:

$$\frac{d\phi(E_\nu, \mathbf{r})}{dE_\nu} = A\frac{dn(E_\nu)}{dE_\nu}\int_{V_\oplus} d^3\mathbf{r}'\frac{a(\mathbf{r}')\rho(\mathbf{r}')P(E_\nu, |\mathbf{r}-\mathbf{r}'|)}{4\pi|\mathbf{r}-\mathbf{r}'|^2} \tag{5.1}$$

where A is the decay rate per unit mass, the integral is over the volume of the Earth, $a(\mathbf{r}')$ is the isotope (^{232}Th or ^{238}U) mass per unit rock mass, $\rho(\mathbf{r}')$ is the rock density and $P(E_\nu, |\mathbf{r}-\mathbf{r}'|)$ is the antineutrino survival probability [48]. The approximation for survival probability used in this work is the same as in [48]:

$$P(E_\nu, L) \approx 1 - 0.5\sin^2 2\theta_{12} \tag{5.2}$$

This is valid as long as matter effects and spectrum distortion due to the non-uniform distribution of the radioactive isotopes can be ignored. As has been estimated in [53] and [60], the possible error of this approximation is about 1%.

In other words, unlike reactor antineutrinos, the terrestrial $\bar{\nu}_e$ spectrum is essentially undistorted by oscillations. The only effect of the oscillations is the proportional suppression of the signal. This lack of spectrum distortion is the consequence of the fact that antineutrino sources are distributed across a large volume. The small distortion caused by the higher concentration of the sources in the crust compared to the mantle can be taken into account in further, more accurate studies, but it is important to bear in mind that exact quantitative estimation of such a distortion is model-dependent.

Chapter 6

Backgrounds

6.1 Accidentals

There is always a finite probability that a pair of single physically unrelated events passes coincidence selection criteria. The higher the single rate and the wider the selection criteria, the higher the rate of such accidental coincidences. Single event rate is several orders of magnitude higher than the rate of true $\bar{\nu}_e$ events. It becomes especially high at the low energy part of the spectrum and at the outer areas of the detector, so that if no energy or fiducial cuts are applied even the number of coincidences coincidences totally overwhelm the expected number of antineutrino events with the ratio of about 3500:1, which would make make analysis almost prohibitively difficult.

All KamLAND studies have to deal with accidental coincidence background. Selection criteria are usually chosen in a way to keep it low but not negligible, so that the sample contamination by accidentals is optimally outbalanced by the sample size. Unfortunately, this is not an option for the combined $\bar{\nu}_e$ analysis because such an optimal choice turns out to be different for reactor and terrestrial antineutrino studies (Section 7.6), so a new approach to the accidental background treatment was necessary, which is described below.

Traditionally, two different methods to study this background have been used in KamLAND: the long off-time window and the random pairing of single events. The off-time window method uses exactly the same selection criteria as in the main study but for the time window, which is chosen much wider to minimize statistical errors and placed off-time to remove the physically correlated events from the sample. Usually, the window from 10 milliseconds to 20 seconds is used for such studies. 10 milliseconds is almost 50 times greater than the neutron capture time, so practically all physical coincidences with neutron captures as delayed event are excluded by this choice. The method is precise enough to measure not only the total rate of accidental coincidences with an extremely good accuracy but also their prompt and delayed spectra for the whole fiducial volume. The fact that the prompt spectrum of

accidental coincidences is different from the prompt spectrum of antineutrino events has been used in KamLAND Rate+Shape analysis. The random pairing method uses the experimental distributions of single events and Monte-Carlo techniques to generate pairs in compliance with selection criteria. This method substantially relies on the absence of unknown correlated backgrounds but is more flexible than the off-time window method.

For the combined $\bar{\nu}_e$ study described here none of the methods work well, though. The combined analysis, in order to provide the accuracy of dedicated studies needs to know not only the spatial distribution of accidental rates but also their local spectra if the spectra are position dependent. Actually prompt and delayed accidental coincidence spectra are position dependent because the distribution of singles in space and energy $\xi(E, \vec{R})$ can not be factored out as a product of some global energy spectrum and some rate spatial distribution:

$$\xi(E, \vec{R}) \neq \zeta(E)\omega(\vec{R}) \tag{6.1}$$

The additional correlations introduced by selection cuts make the adequate description of accidentals very difficult, as long as there are integrations along any of the parameters, let it be the delayed energy or either prompt or delayed coordinates.

However, the following relation remains valid, as long as there are no unaccounted for correlated backgrounds mistakenly mixed with accidentals. The accidental "prompt" and accidental "delayed" are physically independent and their distribution is the same, so the probability density of the accidental event in the direct product space of two energies and two spatial coordinates is strictly the product of individual densities of singles:

$$\psi(E_p, \vec{R}_p, E_d, \vec{R}_d) = \xi(E_p, \vec{R}_p)\xi(E_d, \vec{R}_d) \tag{6.2}$$

This relation implies that the full description of the accidentals is possible, based on the knowledge of the distributions of singles only. Such a description has been used in the fully differential combined analysis. For the differential analysis, there is actually no such notion as an "accidental background". It just considers two separate flows of single events and evaluates the probability for each to give a prompt and a delayed signal with given energies and coordinated independently. This technique is described in more detail in Section 7.7. What is important here, it's enough to know the probability density of singles. Even though the density is very non-trivial and not factorizable (6.1), it is possible to obtain it from KamLAND data with a good accuracy, owing to billions of single events that we have.

The spatial dependence of the singles spectra can be seen in Figure 6.1. In the inner part of the detector, the single rate is predominantly low-energetic but closer to the balloon a higher energy component appears. In particular, going from 500 cm cut to a bigger fiducial volume makes it necessary to repeat the whole accidental coincidence study, no matter what method is used.

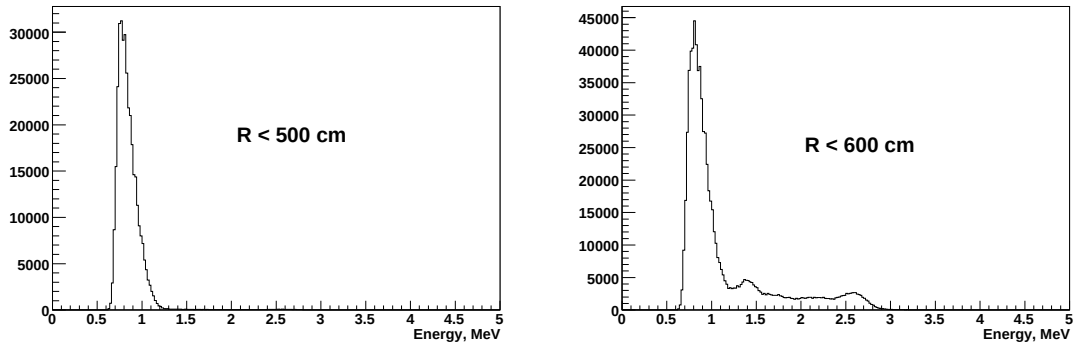

Figure 6.1: Energy spectra of single events for fiducial cuts 500 and 600 cm.

More informative is the 2-dimensional distribution in terms of radius cubed and energy (Figure 6.2). At least three different sources of single events can be located in the plot, making the overall distribution highly irregular. The plot may suggest that at 550 cm and below there are almost no accidentals. Actually this is not the case. The histogram is totally dominated by the low energy singles near the balloon and the small but still considerable part of the distribution can not not seen at this scale.

To make an accidental coincidence, one needs a prompt and a nearby delayed passing the corresponding energy cuts. The rate of accidentals is proportional to the product of the two rates. Figure 6.3 clarifies the picture. There are many low-energy prompt candidates in the whole detector but much less singles that can qualify as "delayed", given a typical selection cut for the delayed even in the coincidence $1.8MeV < E_d < 2.6MeV$. The distribution of the "delayed" singles is more non-uniform. Finally, a prompt cut $E_p > 2.6MeV$ used in KamLAND reactor antineutrino publications reduces the number of accidental coincidence to an almost negligible value for the fiducial cut of 550 cm or less.

As the combined analysis has no option of the high prompt energy threshold, the most comprehensive knowledge about the distribution of the singles has to be collected. To reduce the dimensionality of the problem, an axial symmetry of KamLAND detector was assumed. For bins of equal volume size in the space $(E, R^3, cos(\theta))$, the histogram of single events has been filled with all the KamLAND data available from 2002 through 2005. Normalized to the live time and the volume of each bin, this histogram is essentially the function $\xi(E, \vec{R})$ in (6.1) and (6.2).

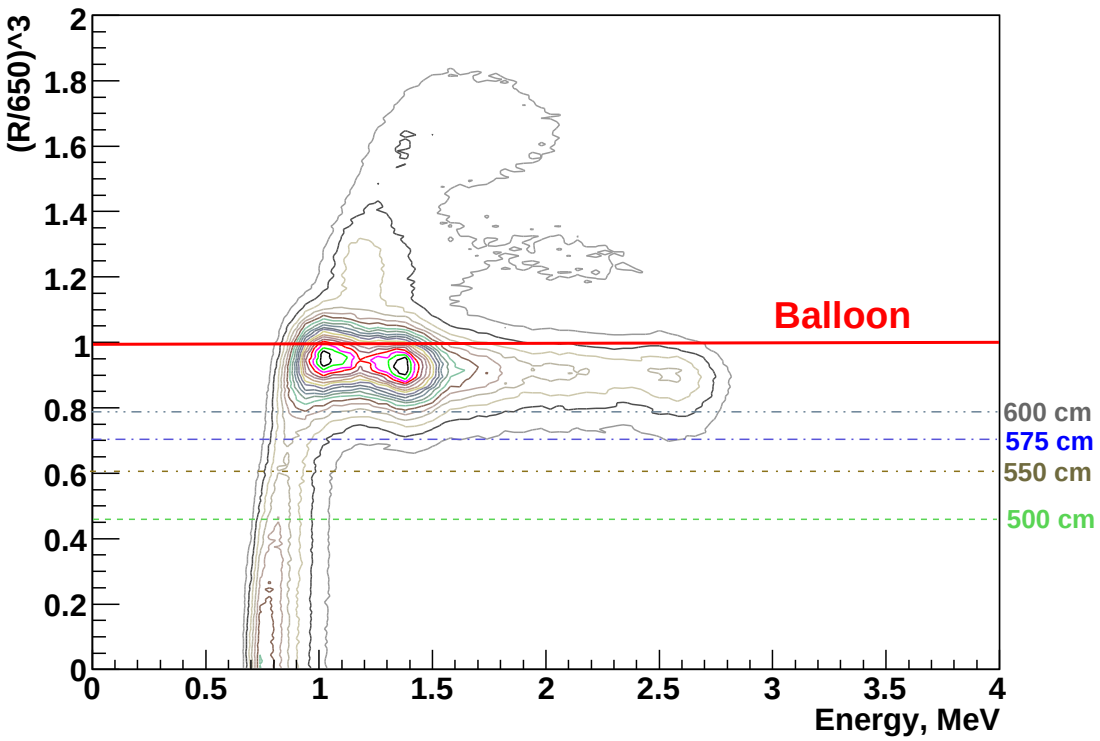

Figure 6.2: Single event density rate as function of energy and radius. The Y-axis is the cubed ratio of the event radius to the radius of the balloon, so that all bins have the same physical volume.

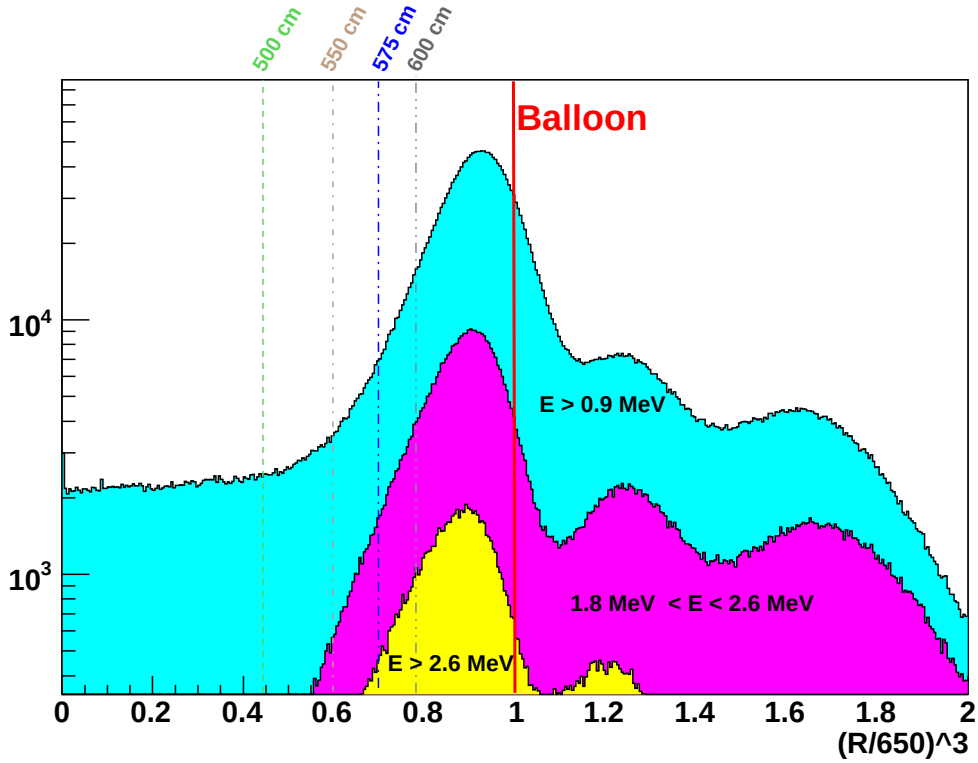

Figure 6.3: Single event density rate as a function of radius for different energy cuts. The X-axis is the cubed ratio of the event radius to the radius of the balloon, so that all bins have the same physical volume.

6.2 Muon Induced Correlated Background

KamLAND is located 1000 m underground, which provides the overburden of 2700 m.w.e. (meters of water equivalent) to shield the detector from cosmic rays, primarily high-energy muons. But even this is not enough to completely exclude muon events and every 3 seconds a muon passes through the inner detector and every 5 seconds – through the scintillator. The huge energy deposited by those events causes temporary problems for data taking by itself, so a 2 ms veto is applied for the whole detector after every muon, which is enough for the electronics to recover. There are more long-lasting effects of muons, though. Muons can cause spallation of the nuclei of the LS. Some spallation products are radioactive with decay modes that almost perfectly mimic an inverse beta decay double coincidence. In particular, β-radioactive ^{8}He (half life 119.0 ms) and ^{9}Li (half life 178.3 ms) in 16% and 49.5% of cases, respectively, decay into the excited state of daughter nuclei that emits a neutron or disintegrate with the emission of a neutrion.

$$\begin{aligned} {}^{8}He &\rightarrow {}^{7}Li + \beta + n + \bar{\nu}_e \\ {}^{9}Li &\rightarrow \alpha + \alpha + \beta + n + \bar{\nu}_e \end{aligned} \tag{6.3}$$

Due to the high Q-values of the β-decays, the prompt signal produced by the β-particle can take on any value within the analysis window. The neutron is captured by the ^{1}H or ^{12}C nuclei of the LS producing exactly the same delayed signal as in the case of the inverse beta decay.

In order to minimize the effect of such fake $\bar{\nu}_e$ candidates, cylinder vetos are applied along the reconstructed tracks of the muon. Even this leaves a few spallation induced coincidences, which need to be taken into account in the analysis. Many studies have been carried out by KamLAND to evaluate this background. It turned out that the spallation background is dominated by ^{9}Li, with ^{8}He constituting less than 15% of it. The prompt spectra of ^{8}He and ^{9}Li backgrounds is shown in Figire 6.4.

Since the combined analysis didn't require special treatment for this background, this work generally followed the methods developed by KamLAND collaboration for reactor and terrestrial $\bar{\nu}_e$ studies. A comprehensive explanation of the procedure can be found in [68] and [53].

6.3 Alpha-n Correlated Background

An α-particle can participate in nuclear reactions with the release of a neutron. If the neutron is emitted with sufficiently high energy or if some other particles are produced in an (α, n) reaction, a double coincidence signature occurs which is extremely difficult to tell from the one made in an inverse beta decay event. There are several alpha-emitting isotopes in KamLAND belonging to Thorium (Table 5.2) and Radium (Table 5.3) decay series. By far, the most abundant alpha-emitter is ^{210}Po from the Radium

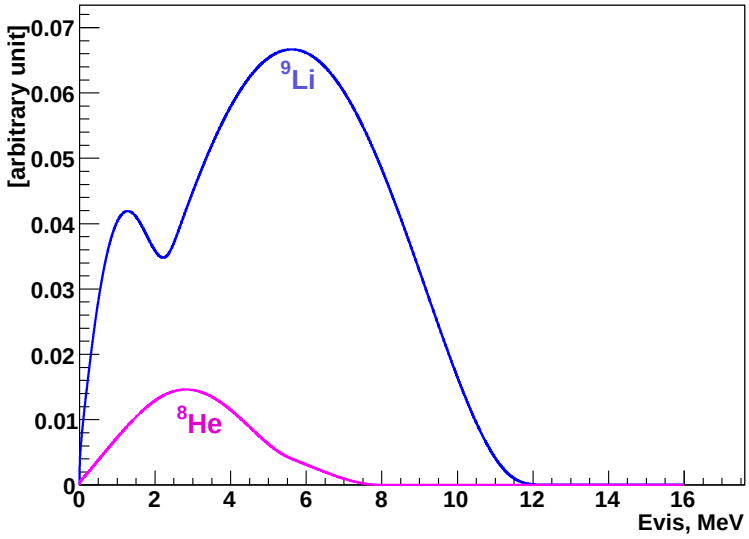

Figure 6.4: ^{8}He and ^{9}Li background prompt spectra.

series. It is a daughter product of a relatively long living ^{210}Pb which is one of the principal radioactive contaminators of the detector. The α-particles from ^{210}Po decays have an energy of 5.3 MeV, which is not enough for (α, n) reactions on most abundant isotopes.

However the stable ^{13}C isotope with a natural abundance of 1.1% has a zero threshold for (α, n) reaction. The cross section for $^{13}C(\alpha, n)^{16}O$ reaction is quite high and, given the measured concentrations of ^{210}Po in KamLAND LS can occur with a frequency smaller than but comparable to the $\bar{\nu}_e$ event rate.

The delayed event resulting from a $^{13}C(\alpha, n)^{16}O$ is the same as for the $\bar{\nu}_e$ inverse beta decay – a neutron capture producing a 2.2 MeV gamma. The physics of the prompt signal is much more complicated.

First of all, an (α, n) reaction on a ^{13}C can leave the resulting ^{16}O in one of excited states. There are two excited states achievable with a 5.3 MeV α produced in a ^{210}Po decay: 6.1299 MeV and 6.0494 MeV. The first deexcites through γ emission, the second – through electron-positron pair production. The neutron released in this reaction has an energy on the scale of hundreds of keV and provides a small but not negligible addition to the prompt signal by elastic scatterings on protons. The shape of this fraction of prompt spectrum is a narrow line centered about 6.2 MeV of E_{vis} (depending on the energy scale calibration).

If the ^{16}O is produced in a ground state, then the neutron has much more energy. About 2% of such neutrons experience an inelastic scattering on a ^{12}C nuclei ($^{12}C(n, n\gamma)^{12}C$ reaction), the excited state of ^{12}C emitting a 4.4 MeV gamma. This forms a small line about 4.75 MeV.

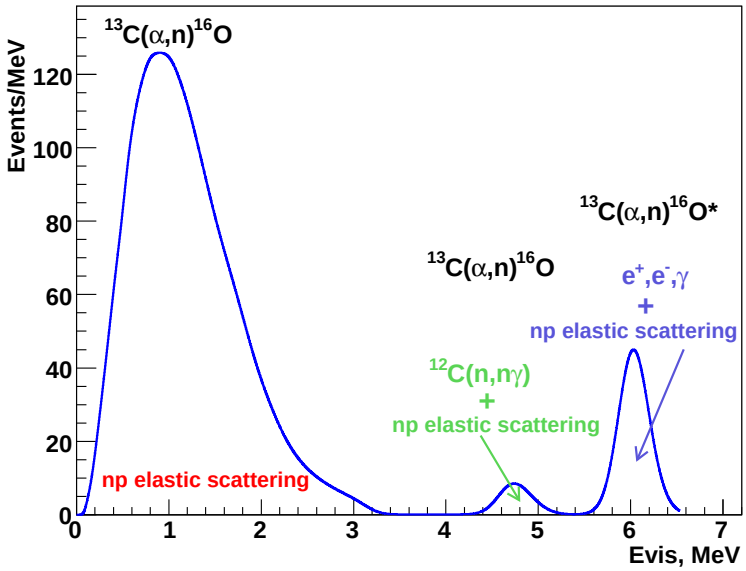

Figure 6.5: Alpha-n background prompt spectrum.

The rest 98% neutrons quickly lose the energy though elastic scattering on protons. Since the initial energy of the neutrons in this case is quite high, they alone can produce enough visible energy to pass the 0.9 ("terrestrial") and even 2.6 MeV ("reactor") energy thresholds. This is by far the biggest part of the spectrum and one of the main troubles for terrestrial antineutrino studies.

The prompt spectrum of the $^{13}C(\alpha, n)^{16}O$ is shown in Figure 6.5. It has been calculated in the RCNS of the Tohoku University with the use of JENDL (Japanese Evaluated Nuclear Data Library) database [69] for the cross sections of the (α, n) reactions and GEANT3 and GEANT4 Monte-Carlo packages for α and neutron tracking in KamLAND LS.

A much more detailed description of this background and its treatment in KamLAND can be found in [53].

6.4 Reactor and Terrestrial Antineutrino Mutual Backgrounding

There is no way to tell a reactor-produced antineutrino from a terrestrial one, as long as its energy can belong to the spectra of both. These two can be separated only statistically. This affects the accuracy with which both can be evaluated. In that combination, the terrestrial antineutrinos are in a bigger disadvantage, for their spectrum is fully covered by the spectrum of their reactor-produced counterparts. No energy selection cut can provide a geo-neutrino window free from reactor background.

Besides, the overall rate of the terrestrial antineutrinos is lower, which makes them relatively more affected by the presence of another source of $\bar{\nu}_e$. One of the results is KamLAND's rather poor sensitivity to the relative fraction of the geo-neutrinos produced in Thorium and Radium decay series despite their different spectra.

Reactor antineutrino studies are in a better situation here. First of all it is possible to set the analysis energy threshold to 2.6 MeV by visible energy and practically exclude the terrestrial antineutrinos completely, which was actually done in KamLAND First [51] and Second [52] neutrino oscillation publications. A more efficient solution, as has been shown in this work, is to include the two terrestrial components to the analysis and release the rates of the two kinds of geo-neutrinos as unconstrained unknown parameters. It can be shown that this technique is guaranteed to produce the results equal or superior to the ones obtainable with the conservative 2.6 MeV cut and the real calculations support this theoretical prediction (Chapter 8). The gain is achieved due to the fact that although the total flux of terrestrial $\bar{\nu}_e$ is not known, the two spectral components are. This is a very serious and absolutely "legal" constraint. Using the 2.6 MeV threshold and discarding all the antineutrino candidates with visible energies lower than that corresponds to asserting that the fluxes, *and the spectra* of geo-neutrinos are both unknown. Actually the spectra are known quite well (Section 5.2) and this knowledge can be used not only in terrestrial but also in reactor $\bar{\nu}_e$ studies.

Besides the spectrum shape, there is one more way to statistically separate terrestrial and reactor antineutrinos from which both antineutrino studies will benefit. Reactor $\bar{\nu}_e$ flux does change with time, while terrestrial does not. A Rate+Shape+Time analysis takes advantage of this fact and offers a better estimation for oscillation parameters and geo-neutrino fluxes than a simpler Rate+Shape can do.

Chapter 7

Likelihood Analysis

7.1 Simple Likelihood Model

For many experiments including KamLAND, the Maximum Likelihood (ML) approach described in e.g. [70], [71] is the main analysis method used to recover the unknown physical parameters from raw experimental data. The accuracy of the method depends on the amount of information used in the construction of the likelihood function (LF). A more accurate description involving more information, generally, leads to more precise estimations and narrower confidence limits but is often unreasonably difficult to implement. For a successful combined antineutrino analysis, the development of a more detailed LF than the one previously used is essential.

LF is the joint probability of the experimental outcomes regarded as a function of the target parameters. Since individual observations (in KamLAND, antineutrino events) are considered independent, the probability can be written as:

$$L(\vec{\theta}) = \prod_{k=1}^{n} f(\mathbf{x_k}; \vec{\theta}) \tag{7.1}$$

Here, $\vec{\theta}$ stands for the set of target parameters (e.g. Δm^2_{12}, geo-neutrino flux) and $\mathbf{x_k}$ is the set of values measured in k-th observation ($\bar{\nu}_e$ energy, time, space and time separation, etc.). During the analysis $\vec{\theta}$ is varied being actually unknown, while $\mathbf{x_k}$ is fixed since it is the observed outcome of the experiment. $f(\mathbf{x_k}; \vec{\theta})$ is the probability density function (PDF) to observe an $\bar{\nu}_e$ event with $\mathbf{x_k}$, given physics parameters $\vec{\theta}$.

Assuming that the PDF $f(\mathbf{x_k}; \vec{\theta})$ adequately the physics of the phenomenon under study, one naturally expects to see a high value of LF for a set of parameters close to true ones and low otherwise. This consideration determines the ML method which prescribes to find the set of parameters $\vec{\theta}$ that delivers the maximum to the LF within the allowable region of the parameter space.

It is usually more convenient to work with the logarithm of LF than with the function itself. The product then turns into the summation.

$$\log(L(\vec{\theta})) = \sum_{k=1}^{n} \log(f(\mathbf{x_k}; \vec{\theta})) \tag{7.2}$$

Two things become apparent here. First, likelihood is determined only up to some constant factor. Multiplying the LF by any constant factor or, equivalently, adding a constant term to its logarithm affects the value of the maximum but not the values of parameters $\vec{\theta}$ that deliver this maximum. Moreover, this factor can be not constant but a function of observed data, as long as it does not depend on the parameters θ. Second, neither the absolute value of LF, nor its logarithm have any physical sense and, in particular, must not be used for the conclusions about the goodness of fit or anything else. What matters for analysis is only the change of LF value with parameters.

To see how the method works, it may be instructive to consider the simplest possible case, derive LF for it and apply the ML method to extract a parameter. Suppose, we have a process that produces events at some unknown constant rate R. For time span T we have observed N events. To decouple this into a product of individual probabilities, we can split the continuous observation time into a sequence of finite but small equal bins ΔT, so that the probability to observe more than one event in a single bin is negligibly small. The probability to observe an event in the i-th time bin is thus

$$P(t_i) = R\Delta T \tag{7.3}$$

for any i.

The joint probability of our observation is the product of the probabilities of observing events within N time bins **and** not observing anything in all others. The latter is equal to $(1 - R\Delta T)$ for each "free of events" time bin.

If we now take the limit of $\Delta T \to 0$, then the product of $R\Delta T$ will become infinitesimally small but the number of factors in the "free of events" part will become infinite, as the overall exposition time is fixed. Owing to the the well known $\lim_{\epsilon\to 0}(1-\epsilon)^{k/\epsilon} = e^{-k}$

$$\lim_{\Delta T\to 0}(1 - R\Delta T)^{T/\Delta T} = e^{-TR} \tag{7.4}$$

This is the "no-observation" part of the LF. The "observation" part is equal to

$$(R\Delta T)^N \tag{7.5}$$

and, formally, does depend on the binning but this dependence does not affect the value of R that maximizes the LF.

So, for our simplest case, we have

$$L = e^{-TR}(R\Delta T)^N \tag{7.6}$$

Since logarithm is a monotonically increasing function, maximizing the logarithm of LF is equivalent to maximizing the function itself but the former is usually simpler to compute.

$$\log(L) = -TR + N \log R - N log \Delta T \tag{7.7}$$

The last term can be omitted in the maximization process. For such a simple case, this can be done analytically by differentiating (7.7) by R and finding the value of the latter that zeroes the derivative:

$$T = \frac{N}{R} \tag{7.8}$$

The answer is the expected $R = N/T$ which, of course, could have been predicted by inspection without any likelihood functions. However even such a simplistic case exhibits some important properties of LF typical of much more advanced studies.

First, of all, the "no-observation" part (7.4) does not depend on the experimental data at all. Second, it is essentially the exponential of the **expected** number of events taken with the "minus" sign. This statement holds for all kinds of relevant analysis and has a remarkable property of not depending on the kind of analysis that is actually done. Whether it is a Rate-only or a Rate+Shape+Time study, this part is the same for any given selection criteria. The "observation" part of LF does depend on both the experimental data and the parameters and is, usually, a bit harder to evaluate.

Despite its simplicity, the LF constructed above can be actually used for a Rate-only oscillation study, once the correct expression for R as a function of oscillation parameters is supplied. However, Rate-only analysis can not provide the best estimation for more than one parameter. It is suitable for disfavoring a hypothesis but, generally, cannot point to the best fit point in more than a one-dimensional parameter space.

Note that this LF does not depend on the time of event arrival or on the energy of the antineutrinos, although this information is available. Only the number of observed events is used, hence the limited power of the method. Going any further requires the accommodation of additional information available from the experiment.

7.2 Rate+Time, Rate+Shape and Rate+Shape+Time Analyses

Going from Rate-only to Rate+Time is quite straightforward. In (7.7) the event rate R was considered constant in time. It really is not constant but, for KamLAND case, can still be expressed as

$$R(t) = KR_0(t), \tag{7.9}$$

where $R_0(t)$ is some known function of time (in KamLAND case, the expected reactor flux) and K, the target parameter (for KamLAND, the disappearance probability averaged over energy).

Expression (7.7) turns into

$$\log(L) = -K \int R_0(t)dt + \sum_{j=1}^{N} \log(KR_0(t_j)) \tag{7.10}$$

(Constant term $Nlog\Delta T$ is omitted here). The integration is done over the observation period, and $R_0(t_j)$ is the value of the rate factor at the time when j-th event was observed. Note that almost nothing has changed. The likelihood equation can still be solved analytically and yields the easily predictable estimation for K:

$$K = \frac{N}{\int R_0(t)dt} \tag{7.11}$$

Note also that the time of event observation does not matter here. Although the likelihood to observe more events in the periods with higher rate factor $R_0(t)$ is higher, this does not affect the value of K at which the maximum is observed. However the addition of any time-independent background makes the event timing important.

Rate+Shape analysis is rather similar to Rate+Time. The difference is that now $R = R(E;\vec{\theta})$, where, in KamLAND case, $\vec{\theta}$ stands for oscillation parameters. Due to its non-trivial dependence on the oscillation parameters, the Rate+Shape LF

$$\log(L) = -\int R(E;\vec{\theta})dE + \sum_{j=1}^{N} \log(R(E_j;\vec{\theta})) \tag{7.12}$$

is more difficult to maximize. In return, it provides much more oscillation information than Rate+Time possibly can.

Rate+Shape+Time case is a rather incremental change over (7.12):

$$\log(L) = -\int\int r(E,t;\vec{\theta})dEdt + \sum_{j=1}^{N} \log(r(E_j,t_j;\vec{\theta})) \tag{7.13}$$

where $\int r(E,t;\vec{\theta})dt \equiv R(E;\vec{\theta})$.

Two details are important here. First, there is a two-dimensional integration for the "no-observation" part. The dimensionality of $r(E,t;\vec{\theta})$ is different from that of $R(E;\vec{\theta})$ in the Rate+Shape case. The Rate+Shape+Time probability density is 2-dimensional, while Rate+Shape is 1-dimensional. However the meaning of this term in the expression is the same: the number of expected events. Second, it is the "observation" part of LF that actually tells apart Rate+Shape and

Rate+Shape+Time analysis. The Rate+Shape deals with spectra integrated over time, while the Rate+Shape+Time takes instantaneous spectra.

For the actual KamLAND oscillation analysis, Rate+Shape+Time approach is computationally more demanding but provides better results than Rate+Shape since the oscillation-related spectrum distortion is not constant in time. This happens because reactors located at different distances change their power, shut down and resume operation thus changing the oscillation pattern. In addition, the fuel composition in reactors changes in time, changing the $\bar{\nu}_e$ energy spectrum. The longer the exposure period, the more advantages Rate+Shape+Time analysis provides because the changes in the spectrum distortion become more pronounced and just integrating them as effectively done in Rate+Shape analysis smears the oscillation picture. The introduction of the new Shika2 power plant in Japan in early 2005 with a much shorter distance to KamLAND than most other reactors made the addition of time information to the analysis almost mandatory.

The form of Rate+Shape LF obtained here is different from the one developed in RCNS for the same purpose and used in KamLAND publication on the spectrum distortion [52]. One can not be directly derived from another. The difference is due to the fact that the RCNS Rate+Shape LF assumes Gaussian distribution for the expected number of events, while (7.12) implies the Poisson distribution. Strictly speaking, the latter is correct whereas the former is not. However, given several hundred antineutrino events, the difference between the two distributions is negligible and the two approaches yield practically indistinguishable results.

7.3 Adding the Backgrounds

Likelihood models discussed so far are still just "toy" models since they ignore backgrounds which are present in all real experiments including KamLAND. The effect of a background is the additional probability or probability density for event observation.

A background is, statistically, just an additional probability to observe an event, so it enters the LF in a way analogous to the antineutrino signal and is an additive correction to it. Instead of $R(E;\vec{\theta})$ in (7.12) we now have $R(E;\vec{\theta}) + B(E)$, or, in case of multiple background sources, $R(E;\vec{\theta}) + B_1(E) + ... + B_n(E)$. Background components, generally, differ from each other and from the main signal in spectra and time distribution. This gives an opportunity to discriminate them statistically, which is done automatically, once the correct energy spectra and time dependencies are supplied.

The explicit form of likelihood logarithm including a background is:

$$\log(L) = -\int \left(R\left(E;\vec{\theta}\right) + B(E)\right) dE + \sum_{j=1}^{N} \log\left(R(E_j;\vec{\theta}) + B(E)\right) \qquad (7.14)$$

And, analogously, for Rate+Shape+Time:

$$\log(L) = -\int\int (r(E,t;\vec{\theta}) + b(E))dEdt + \sum_{j=1}^{N} \log(r(E_j,t_j;\vec{\theta}) + b(E)) \qquad (7.15)$$

where $b(E) \equiv B(E)/T$.

Note that Rate+Shape+Time analysis has an additional advantage of better background suppression for reactor antineutrino studies. The Rate+Shape can discern the background only by its spectrum, while the Rate+Shape+Time can also utilize the fact that the background does not change along with the reactor antineutrino flux.

A background can, in general, be time-dependent, which then needs to be taken into account in the Rate+Shape+Time analysis. Additionally, it can depend on some unknown parameters which are then added as additional dimensions of the parameter "vector" $\vec{\theta}$ (holds for all kinds of analysis, not only Rate+Shape+Time). A more general version of (7.15) then becomes:

$$\log(L) = -\int\int (r(E,t;\vec{\theta}) + b(E,t;\vec{\theta}))dEdt + \sum_{j=1}^{N} \log(r(E_j,t_j;\vec{\theta}) + b(E;\vec{\theta})) \quad (7.16)$$

7.4 Parameter Estimation Errors

Finding the best fit point is only a part of likelihood analysis. Its another part is the estimation of confidence intervals for physics parameters and regions for combinations of those parameters. A confidence range or region for a given confidence level (CL) should be understood as a parameter space subset with highest possible LF, the size of the subset to contain the unknown true parameter value with the probability equal to CL. Since the only information about that parameter available is the experimental data, it is natural to start with the best fit point (which does not necessarily coincide with the true parameter value) and then expand the area by allowing lower likelihoods and covering more of the parameter space. The best fit point, by definition, has the highest likelihood. The points in the parameter space yielding lower likelihoods have correspondingly lower probabilities to be the true parameters.

When LF can be approximated with multidimensional Gaussian distribution, the confidence regions take on the shape of ellipses (in more than 2 dimensions, hyper-ellipsoids) centered around the best fit point. These regions are limited by points of equal likelihood smaller than the likelihood of the best fit point by some constant factor G.

It turns out that, under rather general assumptions, the factor G has a one-to-one correspondence to the probability of the region limited by the condition $\frac{L_{max}}{L(\theta)} < G$ to cover the true parameter or combination of parameters. As was mentioned above, it is almost always more convenient to work with logarithms of likelihoods. It can be

Table 7.1: The values of quantile Q_γ for frequently cited values of CL, in 1-dimensional and 2-dimensional cases.

CL $\equiv 1-\gamma$	n=1	n=2
0.683(1σ)	1	2.31
0.900	2.71	4.61
0.954 (2σ)	3.84	6.17
0.990	6.63	9.21
0.9973 (3σ)	9.00	11.8
0.9999	15.1	18.4

shown [71] that the dependence between the $\log L$ and CL of $1-\gamma$ is

$$\log L_{max} - \log L(\theta) = \frac{Q_\gamma}{2} \tag{7.17}$$

where quantile Q_γ is determined by the equation

$$\int_0^{Q_\gamma} f(z;n)dz = 1-\gamma \tag{7.18}$$

and $f(z;n)$ is the χ^2-distribution with n degrees of freedom.

For a single-parameter confidence range $n = 1$; for a confidence region of two-parameter plane $n = 2$. For a chosen CL, the value of Q_γ is fixed, so these values are usually looked up in tables rather than calculated every time. Table 7.1 lists Q_γ values for most commonly used confidence levels.

In order to find the confidence range or region, the LF is evaluated at every point θ of the parameter space. Then Q_γ is chosen according to the dimensionality of the error estimation and the CL. The points for which $\log L_{max} - \log L(\theta) < Q_\gamma/2$ are included into the confidence range or region.

7.5 Handling the Systematic Uncertainties

Even with the inclusion of backgrounds, the likelihood model is still not adequate for a real experiment because any experiment has systematic uncertainties. In general, the influence of the uncertainties on the parameter estimation is quite complicated, especially if many parameters are involved. For example, fiducial volume error in KamLAND is critical for the accuracy of the mixing angle evaluation but has little effect on the Δm^2.

Geo-neutrino parameter evaluation is affected by errors in the alpha-n background estimation much more than neutrino oscillation parameter evaluation. So just adding the squared systematic uncertainties to the statistical error does not work well.

Fortunately, the likelihood approach provides a straightforward and convenient way to accommodate systematic errors. The expected net effect of systematic uncertainties should be some loss of estimation accuracy, i.e. the widening of confidence regions for given CL.

In order to account for systematic errors, the likelihood parameter space is expanded to include "hidden" parameters corresponding to the uncertainties. They are similar to the "target" physical parameters but are not completely released during the fit. Although the fit is allowed to vary them, some "penalty" is subtracted from the logarithm of the full likelihood. The penalty is higher when the deviation of the uncertain parameter from the central expected value is large, so such a combination gets relatively "disfavored". The lower the uncertainty of the value, the bigger the penalty for a given deviation. Normally, a Gaussian penalty is used and the logarithm of LF is decreased by

$$\Delta \log(L) = \frac{\Delta p^2}{2\sigma^2} \tag{7.19}$$

where Δp is the deviation of the uncertainty parameter from its central value and σ is the estimation of the accuracy with which it is known.

When several **independent** uncertainties are involved, the total penalty is the sum of individual penalties:

$$\Delta \log(L) = \sum_{j=1}^{n} \frac{\Delta p_j^2}{2\sigma_j^2} \tag{7.20}$$

where n is the number of uncertainty parameters.

Systematic uncertainties reduce the exclusion power of the experimental output by allowing the points distant from the best fit to have higher likelihood than they would have if there was no uncertainty.

The procedure for the parameter fit and confidence region evaluation is as follows. First the best fit point is found by varying all parameters, including the "hidden" ones. At his stage, physics parameters are completely free and the systematic uncertainty parameters are indirectly constrained by the information we know about them. After the best fit point is obtained, L_{max} is found by evaluating the LF at it. To determine the confidence interval for some physics parameter, e.g. Δm^2, that parameter is consecutively fixed at different points and the highest possible LF is found by varying all other parameters. It is guaranteed to be less than or equal to L_{max} since the latter is the maximum found over a parameter space of higher dimensionality. For a confidence region, two physics parameters are fixed at a time and the rest are allowed to vary. From this point, the procedure is exactly the same as in the case without systematic uncertainties described in the previous section.

It often happens that different systematic uncertainties, as they can be evaluated experimentally, correlate. In that case, "penalty" to the logarithm of LF becomes:

$$\Delta \log(L) = \frac{1}{2}\mathbf{\Delta p}^T V^{-1} \mathbf{\Delta p} \tag{7.21}$$

where $\mathbf{\Delta p}$ should be understood as the n-dimensional vector of the parameter deviations from central values and V^{-1} is the $n \times n$ inverse covariance matrix of the uncertainty parameters.

In many cases it is possible to avoid the calculation of the covariance matrix by the choice of uncertainty parameters so that they are independent or their correlation is negligible. For example, in the case of alpha-n background uncertainties, the overall rates in the low energy and the 4 MeV regions are strongly correlated and using the formula (7.20) is not acceptable and (7.21) must be used. However, if the total rate of $\alpha - n$ events and the ratio between the 4 MeV and low-energy regions are considered instead, the two parameters become practically disentangled.

7.6 Selection Criteria Problem for Combined Analysis

In practice, likelihoods introduced above depend on a group of other implicit parameters not discussed yet: event selection criteria. It is usually impractical or impossible to achieve a 100% detection efficiency by considering all possible candidates. For KamLAND $\bar{\nu}_e$ studies, this is especially obvious. Only the coincidences correlated in space and time can be $\bar{\nu}_e$ candidates but since they are correlated through unlimited distributions, any pair of events can, theoretically, be such a candidate. Of course, given that the distributions are mostly Gaussians and exponentials, they fall quickly, so ignoring the "coincidences" separated by, say, 10 ms or more in time gives a negligible hit on the selection efficiency while reducing accidentals. Generally speaking, selection criteria is a tradeoff between detection efficiency and sample purity.

There is an element of arbitrariness in the choice of selection criteria but if the resulting backgrounds and efficiencies are correctly taken into account in the LF, all the choices must yield consistent results. Nevertheless, not all selection policies are equal. There is usually some optimum choice. Going for wider selection criteria improves the efficiency but this may be more than negated by the increased background rates. Higher systematic uncertainties and the quality of event reconstruction may also be factors in favor of tighter selection cuts. On the other hand, if the selection cuts are too tight, the low efficiency and smaller number of candidates leads to higher statistical error. Once again, a poor choice of selection criteria itself does not result in a systematically biased parameter estimation (as long as the LF is written correctly) but does decrease the estimation accuracy.

The main problem for the combined analysis effort is the actual disagreement between optimal selection policies for the two different studies. Table 7.2 shows that all three KamLAND antineutrino papers used different selection criteria. At first, the selection cuts were kept conservative because of the limited understanding of the backgrounds, systematic errors and insufficient quality of reconstruction tools at that early stage of KamLAND experiment. Later, as KamLAND achieved substantial improvements in those areas, the usage of wider selection criteria became justifiable. This allowed for a more precise estimation of the oscillation parameters, mostly due to the smaller statistical error. However, for the geo-neutrino paper [48], KamLAND "returned" to the selection criteria very similar to those used in the first oscillation result, although that paper was written later than the [52] and used the same reconstruction tools.

It is not difficult to understand the reason why the optimal selection criteria are different. In fact there are two separate reasons and, unfortunately, both work in the same direction. First, the expected rate of geo-neutrino events is substantially less than that of reactor events, so it takes less backgrounds to compromise the accuracy of terrestrial $\bar{\nu}_e$ parameter estimation to the same degree. Second, some backgrounds are much more intensive in the lower part of the spectrum, so, given the same selection criteria, there are actually much more background events in the geo-neutrino analysis event window.

An attempt to use "reactor-like" selection criteria for terrestrial studies will give approximately 1.8 times more expected geo-neutrino events but, at the same time, the number of background events will explode to exceed the geo-neutrino signal by almost a factor of 20 instead of 6 for the selection criteria used in [48]. The potential gain in accuracy roughly $\propto \sqrt{1.8}$ is smaller than the expected accuracy loss due to sample contamination $\propto \sqrt{(20+1)/(6+1)}$, and real numerical experiments confirm this expectation.

At the same time, the geo-neutrino selection cuts are unnecessarily tight for reactor $\bar{\nu}_e$ studies, especially when the 2.6 MeV analysis threshold is used. In that case, no matter whether the "reactor" or "terrestrial" criteria are used, the background event rate is substantially smaller than the signal but the tighter selection criteria simply yield 1.8 times smaller statistics and, consequently, almost $\sqrt{1.8} = 1.34$ higher statistical uncertainty.

However this contradiction is not unavoidable. A hint to this can be found in the selection criteria themselves. The radial fiducial cut is tighter for terrestrial (i.e. more background-sensitive) studies because some backgrounds (primarily accidentals but also alpha-n) are more intensive in the outer areas of the detector, so ignoring them keeps "signal to noise" ratio of the sample at lower levels. Similarly, the events with greater time or space separations have relatively lower probability to be real antineutrinos rather than accidental coincidences, so going for tighter separation cuts effectively cleans up the sample.

Selection criteria variation makes use of this information about relative statistical significance of the events with different observed parameters. This use is rather

Table 7.2: KamLAND $\bar{\nu}_e$ selection criteria used in different publications

Parameter	Reactor-1 [51]	Reactor-2 [52]	Geo $\bar{\nu}_e$ [48]
Radial cut, prompt, cm	$R_p < 500$	$R_p < 550$	$R_p < 500$
Radial cut, delayed, cm	$R_d < 500$	$R_d < 550$	$R_d < 500$
Cylinder cut 120 cm	yes	no	yes
Prompt Energy, MeV	$2.6 < E_p < 8.5$	$2.6 < E_p < 8.5$	$0.9 < E_p < 2.6$
Delayed Energy, MeV	$1.8 < E_d < 2.6$	$1.8 < E_d < 2.6$	$1.8 < E_d < 2.6$
Time Separation, μs	$0.5 < \Delta T < 660$	$0.5 < \Delta T < 1000$	$0.5 < \Delta T < 660$
Space Separation, cm	$\Delta R < 160$	$\Delta R < 200$	$\Delta R < 160$

crude, however, and reflects neither the true amount of information we already have or can get from the detector, nor the physics behind this information. Indeed, all potential candidates are simply grouped into two categories, "good", that pass the chosen selection criteria, and "bad", that don't. After that the "good" events are treated absolutely equally. This would be an optimal strategy if the real physical distributions were step-functions, which is, certainly, not the case.

7.7 Differential Likelihood

Qualitatively, the candidates that "easily" pass the selection cuts (i.e. have short time and space separations and are not close to the totally excluded outer areas of the detector) are relatively more likely to be antineutrinos rather than background events, compared to their counterparts that have barely passed one or more selection criteria. This knowledge can be accommodated by giving them higher statistical weights. Two questions had to be answered before this concept could yield any practical result:

- What is the strict quantitative correspondence between such "statistical weights" or their analogs, and the real distributions of $\bar{\nu}_e$ and background events?
- Is it possible to get all the necessary distributions from the experimental data?

Answering those questions lead to the fully differential likelihood analysis that allows to use the same criteria for terrestrial and $\bar{\nu}_e$ studies without compromising the quality of either and, additionally, offers a higher parameter estimation accuracy. Instead of adjusting the selection cuts, differential likelihood approach rather adjusts the statistical weights of antineutrino candidates. Moreover, it does that automatically and *optimally*, as long as the description of the detector's properties is adequate.

Theoretically, a differential analysis does not need any selection cuts at all since its accuracy can only grow when more events are included. In practice, some cuts are still necessary because otherwise the number of candidates will be overwhelming.

In KamLAND, an attempt to abolish only fiducial volume cuts would result in more than 2 million candidates, causing a more than 1000-fold slowdown in the parameter estimation process for moderate potential accuracy gains. Besides, the quality of event reconstruction is harder to monitor at the outer areas of the detector. Moreover, the aforementioned description of the detector's properties can never be absolutely correct, and the error becomes bigger when wider selection cuts are applied. However, unlike the traditional approach that treats all events passing the cuts equally, the differential approach does not have a *theoretical* optimum after which the accuracy of parameter evaluation would decrease. If everything could work perfectly, then more candidates would be always better.

Differential likelihood is based on the comprehensive use of the information that can be collected by KamLAND about individual antineutrino candidates. Each antineutrino candidate conveys the following information available from the data reconstruction: Prompt Energy, Delayed Energy, Prompt Time, Delayed Time, Prompt Vertex (x, y, z), Delayed Vertex (x, y, z): 10 parameters overall.

Traditional Rate+Shape analysis for either reactor or terrestrial antineutrinos uses most of this information just for selection cuts. As was just explained, once the double coincidence has passed the chosen selection criteria, some data that determined the passage is not considered anymore. In particular, the delayed energy, space and time separation and the event times are ignored. The only parameter treated comprehensively is the prompt (essentially, the antineutrino energy). A Rate+Shape+Time study adds prompt time to the analysis to minimize the smearing introduced by the change of the baseline over time. These approaches has an advantage of relative simplicity but do not make the optimal use of all the available information. Out of 10 parameters, 8 are essentially thrown away after the selection cuts.

From the formal point of view, all the necessary information information is contained in the 10-dimensional probability density distribution. Correspondingly, the most detailed likelihood possible is determined as the product of those probability densities of dimensions $Time^{-2} \times Length^{-6} \times Energy^{-2}$. Each factor in the differential likelihood is considered as the probability of detecting a prompt event in a 5-dimensional elementary hypercube made of 3 spatial dimensions, unit energy and unit time, and a delayed event in a similar 5-dimensional elementary hypercube – 10 dimensions total. No integration, explicit or implicit is done at this stage; all probabilities are evaluated with respect to *elementary* (hyper)volumes. This the distinctive feature of the fully differential likelihood. The only integration that needs to be done is the evaluation of the total number of events observed with given selection criteria and "explicit" physical parameters $\vec{\theta}$ (including the ones corresponding to systematic uncertainties).

For comparison, in the Rate+Shape analysis, each factor is the 1-dimensional probability density of dimensions $Energy^{-1}$, normalized to the total expected number of events in the *whole* detector during the *whole* observation period. In addition to those two rather apparent integrations, more integrations are made implicitly: in space and time separation and delayed energy when the efficiency of the cuts is

evaluated. The Rate+Shape analysis is differential with respect to one dimension and integral in the remaining nine. The Rate+Shape+Time analysis is differential in two dimensions (prompt time and energy) and integral in eight. Each factor of Rate+Shape+Time likelihood has a dimensionality of $Energy^{-1} \times Time^{-1}$. Rate-only analysis is fully integral and its elementary likelihood is dimensionless.

If done properly, a differential analysis is guaranteed to deliver the same or better accuracy than integral simply because it makes use of more detailed information. However the gains may not be substantial if any at all. The main advantage of the fully differential likelihood model for KamLAND studies is the much more efficient background suppression and hence the opportunity to include the relatively "dirty" areas which otherwise would be better ignored. Note that this works best if the background is very different from the main signal in the way it's distributed in the 10-dimensional space. If the distributions are similar (as is the case with spallation backgrounds or with terrestrial versus reactor $\bar{\nu}_e$ mutual backgrounding), the differential likelihood offers little advantage.

The differential likelihood is constructed in a rather straightforward way. It can be regarded as just a generalization of the Rate+Shape+Time likelihood. Let's first rewrite the expression (7.15) by denoting $r(E,t;\vec{\theta}) + b(E) \equiv f(E,t;\vec{\theta})$:

$$\log(L) = -\int\int f(E,t;\vec{\theta}) dE dt + \sum_{j=1}^{N} \log(f(E_j,t_j;\vec{\theta})) \tag{7.22}$$

Here, $f(E,t;\vec{\theta})$ stands for cumulative event observation density either from a true antineutrino interaction or from any background source. This density is still in 2-parameter space. A 10-dimensional density can, generally speaking, depend on all 10 measured event parameters:

$$f(E,t;\vec{\theta}) \rightarrow \phi(E_p,t_p,\vec{R}_p,E_d,t_d,\vec{R}_d;\vec{\theta}) \tag{7.23}$$

where p subindex stands for "prompt" and d for "delayed". Note that E in $f(E,t;\vec{\theta})$ is E_p in $\phi(E_p,t_p,\vec{R}_p,E_d,t_d,\vec{R}_d;\vec{\theta})$.

The fully differential likelihood is

$$\begin{aligned} \log(L) &= -\int\int\int\int\int\int \phi(E_p,t_p,\vec{R}_p,E_d,t_d,\vec{R}_d;\vec{\theta}) dE_p dt_p d^3R_d dE_d dt_d d^3R_d \\ &+ \sum_{j=1}^{N} \log(\phi(E_{p_j},t_{p_j},\vec{R}_{p_j},E_{d_j},t_{d_j},\vec{R}_{d_j};\vec{\theta})) \end{aligned} \tag{7.24}$$

The physical meaning of $\phi(E_p,t_p,\vec{R}_p,E_d,t_d,\vec{R}_d;\vec{\theta}) dE_p dt_p d^3R_d dE_d dt_d d^3R_d$ is the following: it's the probability to observe a prompt signal with energy in the elementary range dE_p at time within dt_p in elementary volume d^3R_p **and** a delayed signal with energy in the elementary range dE_d at time within dt_d in elementary volume d^3R_d.

Note also that despite the different look, the value of the integral in (7.24) is exactly the same as that of its counterpart in (7.22) and is just the expected number of events with chosen selection criteria. It's the "observed" parts (i.e. the sums of logarithms) that tell one likelihood from another.

Similar to $f(E,t;\vec{\theta})$ $\phi(E_p,t_p,\vec{R}_p,E_d,t_d,\vec{R}_d;\vec{\theta})$ represent a cumulative event density and is thus a sum of antineutrino event densities and those of all possible backgrounds. Explicitly,

$$\begin{aligned}\phi(E_p,t_p,\vec{R}_p,E_d,t_d,\vec{R}_d;\vec{\theta}) &= \rho(E_p,t_p,\vec{R}_p,E_d,t_d,\vec{R}_d;\vec{\theta}) \\ &+ \gamma(E_p,t_p,\vec{R}_p,E_d,t_d,\vec{R}_d;\vec{\theta}) \\ &+ \mu(E_p,t_p,\vec{R}_p,E_d,t_d,\vec{R}_d;\vec{\theta}) \\ &+ \alpha(E_p,t_p,\vec{R}_p,E_d,t_d,\vec{R}_d;\vec{\theta}) \\ &+ \psi(E_p,t_p,\vec{R}_p,E_d,t_d,\vec{R}_d;\vec{\theta}), \end{aligned} \tag{7.25}$$

where

- $\rho(E_p,t_p,\vec{R}_p,E_d,t_d,\vec{R}_d;\vec{\theta})$ – reactor $\bar{\nu}_e$ event density
- $\gamma(E_p,t_p,\vec{R}_p,E_d,t_d,\vec{R}_d;\vec{\theta})$ – terrestrial $\bar{\nu}_e$ event density
- $\mu(E_p,t_p,\vec{R}_p,E_d,t_d,\vec{R}_d;\vec{\theta})$ – muon-induced spallation background event density
- $\alpha(E_p,t_p,\vec{R}_p,E_d,t_d,\vec{R}_d;\vec{\theta})$ – alpha-n background event density
- $\psi(E_p,t_p,\vec{R}_p,E_d,t_d,\vec{R}_d;\vec{\theta})$ – accidental coincidence background density

The likelihood described in such a general way is practically useless because it is almost impossible to handle 10-dimensional probability densities. Fortunately, the effective dimensionalities of the elements of (7.25) turn out to be much smaller.

Accidentals allow the most straightforward simplification. As long as they are true accidental coincidences of uncorrelated single events and not some kind of unknown correlated background,

$$\psi(E_p,t_p,\vec{R}_p,E_d,t_d,\vec{R}_d;\theta) = \xi(E_p,t_p,\vec{R}_p;\theta) \times \xi(E_d,t_d,\vec{R}_d;\theta), \tag{7.26}$$

where $\xi(E_d,t_d,\vec{R}_d;\theta)$ is a 5-dimensional density of single event rate. Assuming the axial symmetry of the detector, these densities become 4-dimensional. Now, given billions of single events that KamLAND has, and the relatively slow change of this density with time, it becomes quite possible to restore this distribution from the real experimental data, which was done as described in Section 6.1. Note that no modeling was used for this background's description. It is essentially a direct measurement.

Antineutrino events, regardless of their terrestrial or reactor origin, are correlated in space time, so their distributions cannot be factored out in a way similar to (7.26). However they possess a quality that enables a comparable simplification.

Unlike the accidentals, their distribution within a fiducial volume is uniform, as far as "border effects" (e.g. efficiency loss due to neutron capture gamma leaving the scintillator volume) are negligible. Prompt timing is also uniform for terrestial antineutrinos. For reactor antineutrinos, it's not uniform on the scale of days but still can be considered uniform on the scale of prompt-to-delayed time separation, which is on the order of hundreds of microseconds. This uniformity gives rise to a translational symmetry:

$$\gamma(E_p, t_p, \vec{R}_p, E_d, t_d, \vec{R}_d; \vec{\theta}) = \gamma(E_p, t_p + \delta t, \vec{R}_p + \delta\vec{R}, E_d, t_d + \delta t, \vec{R}_d + \delta\vec{R}; \vec{\theta}) \quad (7.27)$$

and similarly for reactor $\bar{\nu}_e$, as long as δt is small compared to the characteristic time of reactor flux change:

$$\rho(E_p, t_p, \vec{R}_p, E_d, t_d, \vec{R}_d; \vec{\theta}) = \rho(E_p, t_p + \delta t, \vec{R}_p + \delta\vec{R}, E_d, t_d + \delta t, \vec{R}_d + \delta\vec{R}; \vec{\theta}) \quad (7.28)$$

It's the difference between the prompt and delayed vertices ($\Delta R \equiv |\vec{R}_p - \vec{R}_d|$) and times ($\Delta T \equiv t_d - t_p$) that actually determine the probability denstity to observe a coincidence.

Next, E_d, ΔR and ΔT are uncorrelated (in fact there is a weak correlation between ΔR and ΔT but Monte-Carlo simulations suggest that it is negligible). E_p is correlated with ΔR because higher energy $\bar{\nu}_e$ gives a more concentrated energy deposition in the scintillator and, besides, a higher energy event has a smaller vertex reconstruction smearing. The probability distributions for terrestrial antineutrinos then splits into much distributions:

$$\gamma(E_p, t_p, \vec{R}_p, E_d, t_d, \vec{R}_d; \vec{\theta}) = \gamma_0(E_p) \times s_{\bar{\nu}_e}(E_p, \Delta R) \times \tau_c(\Delta T) \times \kappa(E_d) \quad (7.29)$$

where

- $\gamma_0(E_p)$ – visible energy spectrum of geo-neutrinos normalized to the geo-neutrino detection rate per unit volume
- $s_{\bar{\nu}_e}(E_p, \Delta R)$ – space separation distribution for $\bar{\nu}_e$ coincidences
- $\tau_c(\Delta T)$ – time separation distribution for all physical coincidences with neutron capture delayed events (including $\bar{\nu}_e$)
- $\kappa(E_d)$ – neutron capture event visible spectrum

Reactor antineutrinos are different only in that their energy spectrum energy is time dependent:

$$\rho(E_p, t_p, \vec{R}_p, E_d, t_d, \vec{R}_d; \vec{\theta}) = \rho_0(E_p, t_p) \times s_{\bar{\nu}_e}(E_p, \Delta R) \times \tau_c(\Delta T) \times \kappa(E_d) \quad (7.30)$$

where

- $\rho_0(E_p, t_p)$ – instantaneous visible energy spectrum of reactor antineutrinos normalized to detection rate per unit volume

All the distributions in the right hand sides of (7.29) and (7.30) are calculable and need to be known anyway to determine the efficiency of selection cuts, no matter whether the differential likelihood is used or not. So the fully differential analysis adds no complexity here.

Muon-induced spallation background is very similar to terrestrial antineutrinos in its distribution. It is physically uniform in both space and time (muon flux is constant). The delayed event is neutron capture, physically equivalent to that after an inverse beta decay, so time separation distribution is the same. Space separation is slightly different since the prompt event is made not by a positron signal but by an electron with a small addition of neutron elastic scattering on protons. The explicit decomposition for the muon-induced spallation background has the form:

$$\mu(E_p, t_p, \vec{R}_p, E_d, t_d, \vec{R}_d; \vec{\theta}) = \mu_0(E_p) \times s_\beta(E_p, \Delta R) \times \tau_c(\Delta T) \times \kappa(E_d) \tag{7.31}$$

where

- $\mu_0(E_p)$ – visible energy spectrum of the spallation background normalized to the background's rate per unit volume
- $s_\beta(E_p, \Delta R)$ – the distribution of beta-n coincidences in space separation and energy

Alpha-n background is the most complex case. On one hand, it is correlated similarly to antineutrino events due to the same neutron capture delayed signal, so no decomposition like (7.26) is possible. On the other hand, it is not uniform within the fiducial volume, being considerably more intensive in the areas close to the balloon. Strictly speaking, it is not constant in time either, although this change can be neglected because of the relatively long life time (22.3 years) of ^{210}Pb which is the source of ^{210}Po, the main generator of alphas in KamLAND. The best possible general decomposition for its distribution, assuming time uniformity, is:

$$\alpha(E_p, t_p, \vec{R}_p, E_d, t_d, \vec{R}_d; \vec{\theta}) = \alpha_0(E_p, \vec{R}_p, \vec{R}_d) \times \tau_c(\Delta T) \times \kappa(E_d) \tag{7.32}$$

where

- $\alpha_0(E_p, \vec{R}_p, \vec{R}_d)$ – the distribution of the background's rate in the 7-dimensional parameter space

Assuming also the axial symmetry of the detector, it is possible to decrease the effective dimensionality of $\alpha_0(E_p, \vec{R}_p, \vec{R}_d)$ by one. Due to the lack of spatial translational symmetry for this background, $\alpha_0(E_p, \vec{R}_p, \vec{R}_d)$ can not, generally speaking, be written as $\alpha'(E_p) \times \eta(\vec{R}_p) \times s_\alpha(E_p, \Delta R)$. Yet, this remains an acceptable approximation, as long as the dependence of $\alpha_0(E_p, \vec{R}_p, \vec{R}_d)$ on the space separation $|\vec{R}_p - \vec{R}_d|$

is much stronger than on prompt or delayed positions themselves, which is true unless areas too close to the balloon are included in the analysis. This work uses the approximation:

$$\alpha(E_p, t_p, \vec{R}_p, E_d, t_d, \vec{R}_d; \vec{\theta}) = \alpha'(E_p) \times \eta(\vec{R}_p) \times s_\alpha(E_p, \Delta R) \times \tau_c(\Delta T) \times \kappa(E_d) \quad (7.33)$$

where

- $\alpha'(E_p)$ – the prompt visible spectrum of alpha-n background
- $\eta(\vec{R}_p)$ – spatial distribution the background's rate per unit volume in R_p
- $s_\alpha(E_p, \Delta R)$ – space separation distribution for alpha-n coincidences, calculated for the uniform distribution of the alpha-n events

7.8 Delayed Spectrum for Correlated Events

The delayed signal energy spectrum introduced in Section 7.7 as $\kappa(E_d)$ is caused by a monoenergetic gamma line of neutron capture on a hydrogen nucleus. It has the fixed energy of 2.223 MeV but due to final energy resolution of the detector is reconstructed as a nearly Gaussian distribution centered around that value. The spread of this distribution depends on the properties of the detector itself and on the quality of the energy reconstruction algorithm. As was mentioned above, this work uses the standard energy reconstruction procedure developed at the Tohoku University which is measured to provide the absolute energy resolution of $6.2\% \times \sqrt{E_{vis}[MeV]}$ with both 17" and 20" PMT's and $7.25\% \times \sqrt{E_{vis}[MeV]}$ with 17" PMT's only. So, omitting the energy scale errors here, the delayed energy spectrum can be written explicitly:

$$\kappa(E_d) = \frac{1}{0.0725\sqrt{2\pi}\sqrt{E_d}} e^{-\frac{(E_d - 2.223)^2}{2(0.0725)^2 E_d}} \quad (7.34)$$

for the early runs taken without 20" PMTs and

$$\kappa(E_d) = \frac{1}{0.062\sqrt{2\pi}\sqrt{E_d}} e^{-\frac{(E_d - 2.223)^2}{2(0.062)^2 E_d}} \quad (7.35)$$

for the newer runs taken after 20" PMTs were turned on. The energy is assumed to be expressed in MeV.

7.9 Time Separation

Time separation distribution referred to as $\tau_c(\Delta T)$ in Section 7.7 is, physically, an exponential with some parameter constant for a given scintillator. Several studies

have been performed by KamLAND to determine this constant based on different techniques: neutron source calibration, measurement of muon-induced neutron capture time and a Monte-Carlo simulation with GEANT package. These techniques are described in more detail in [53]. All gave consistent results with the central value of $211.2\mu s$ which is used in this work. The explicit form for the separation distribution factor is thus:

$$\tau_c(\Delta T) = \frac{1}{211.2\mu s} e^{-\frac{\Delta T}{212.2\mu s}} \tag{7.36}$$

7.10 Space Separation

Unlike time separation, space separation distribution does not have a simple analytical form. The actual shape of the distribution needs to be found through simulation. Moreover, regardless of the source it depends on the prompt signal energy in a non-trivial way, so the whole family of such distributions have to be generated for a set of prompt energies. Finally, space separation distributions are not the same for antineutrinos and background events and must be treated separately.

Since not all information on these distributions required by the differential analysis was available from the earlier KamLAND studies, a new study had been done, which is described in this section.

As was described in Section 1.7, the prompt signal is made mostly by the positron (through ionization and Cherenkov radiation) and by the two gammas from its annihilation afterwards. The delayed signal in KamLAND scintillator is produced by a single 2.223 MeV neutron capture gamma. The gammas have no charge and thus do not cause scintillation themselves but they pass their energy to electrons. The electrons then produce scintillation. The path of gammas in scintillator depends on their energy and is on the scale of tens of centimeters, which can not be neglected.

Physically, both prompt and delayed signals in LS from $\bar{\nu}_e$ events are finite areas of energy deposition by charged particles and hence scintillation. Full reconstruction of those areas would be very desirable but, due to the limited number of photoelectrons obtainable in existing liquid scintillators, is practically impossible. Instead, some reference point in space can be found for prompt and delayed signals. Normally, this point is associated with the three-dimensional center of light emission and is referred to as the "reconstructed vertex". Note that it, generally, does not coincide with the physical event that has caused it but this center is actually found by a vertex fitter. Additionally, vertex fitter can not be perfect and always introduces reconstruction error.

KamLAND experiment has only prompt and delayed reconstructed vertices available for analysis and both are displaced from the original point where the inverse beta decay took place. The position of the latter is unknown, so the absolute displacement of either prompt or delayed signals relative to its origin is useless. What can be compared with experimental data is the prompt-to-delayed displacement, i.e. the space separation $s_{\bar{\nu}_e}(E_p, \Delta R)$ in (7.30) and (7.29).

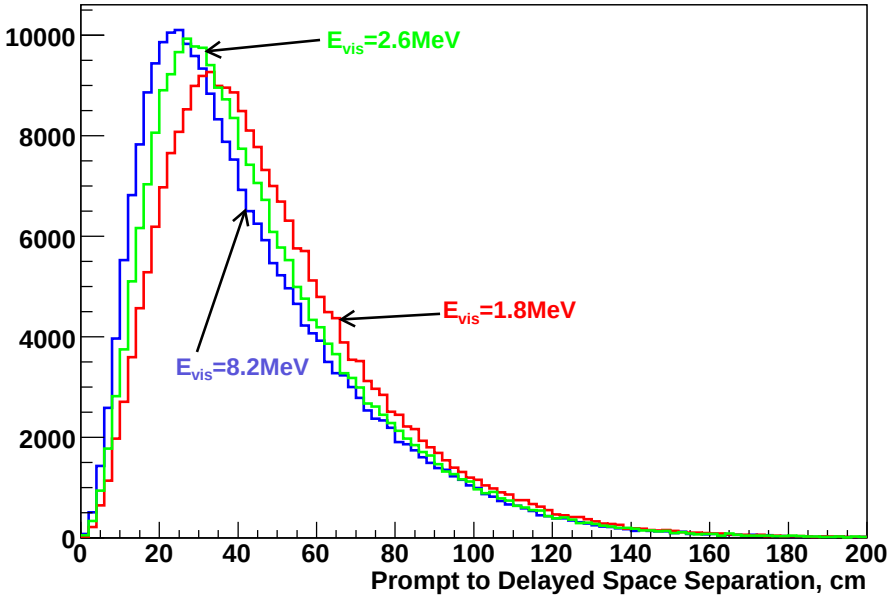

Figure 7.1: Space separation distributions for $\bar{\nu}_e$ coincidences. Shown for prompt visible energies 1.8 MeV, 2.6 MeV and 8,2 MeV.

This separation was simulated by tracking the particles involved in the process through the scintillator. The simulation employed GEANT4-07-01 Monte-Carlo package freely available from CERN. To track the neutrons, the G4NDL3.7 neutron scattering cross section database was used. More than 200,000 events were generated. The coordinates and magnitudes of energy depositions were stored and later averaged to provide the estimations for reconstructed vertices.

The additional smearing by the vertex reconstruction has been included in the simulation using the known performance of "V2" vertex fitter. The resulting space separation distributions are shown in Figure 7.1 for three visible energies in the reactor antineutrino range.

Space separation distributions for alpha-n events $s_\alpha(E_p, \Delta R)$ in (7.33) are different because of the different physics of the prompt event but can be obtained in a similar way. This work used the distributions obtained earlier with the use of GEANT3 package.

Chapter 8

Analysis Resutls

8.1 Rate+Shape Oscillation Analysis

To test the operation of the newly written parameter fitter and, additionally to evaluate the effect of the longer exposition available for this study compared to the KamLAND Second Oscillation Result [52], a study has been carried out with exactly the same selection criteria and analysis methods as used in [52].

The coincidences conforming to the following requirements were used:

- Fiducial cut: $R_{prompt} < 550cm$, $R_{delayed} < 550cm$
- Space Separation cut: $\Delta R < 200cm$
- Time Separation cut: $0.5\mu s < \Delta T < 1000\mu s$
- Prompt Energy: $2.6MeV < E_{prompt} < 8.5MeV$
- Delayed Energy: $1.8MeV < E_{prompt} < 2.6MeV$

Besides, the following muon veto policy was applied:

- 2 ms veto for the whole detector after a muon
- 2 second veto for the whole detector after a showering or badly reconstructed muon
- 2 second veto for a 3-meter cylinder with the axis along the reconstructed muon track

Instead of 515.1 days of effective live time (after muon cuts) available in 2004, this study used 944.4 days of exposition. To compare with the published results, the best fit point for $(\sin^2 2\theta_{12}, \Delta m^2_{12})$ was evaluated along with the confidence region for Δm^2_{12}, and two-parameter allowed region plot was made.

Δm^2_{12} is estimated to be $7.57^{+0.30}_{-0.26} eV^2$; the best fit for $\sin^2(2\theta) = 0.83$. For comparison, the KamLAND result obtained with the same analysis method but on 515.1 days of exposition gave Δm^2_{12} is estimated to be $7.9^{+0.4}_{-0.3} eV^2$; the best fit for $\sin^2(2\theta) = 0.86$.

The allowed parameter plot is presented in Figure 8.1.

These results are quite expected: more statistics allows to obtain a consistent result with higher accuracy. The 1.25-fold improvement is close to theoretically possible 1.35 which would have been achievable only if there were no systematic uncertainties and if the baseline pattern did not change during the period of observation. This improvement was achieved solely by the smaller statistical error due to the larger number of observed events with no enhancements in the analysis procedure.

The following sections describe the effect of more sophisticated analysis methods when applied to the data collected in the same observation period.

8.2 Rate+Shape+Time Oscillation Analysis

This study is exactly the same as the previous one, except that newly developed Rate+Shape+Time analysis was used instead of Rate+Shape. The result is shown in Figure 8.2.

This analysis provides $7.59^{+0.29}_{-0.25} eV^2$ for Δm^2_{12}; the best estimation for $\sin^2(2\theta) = 0.86$.

A higher accuracy is achieved but the accuracy gain is quite small. The discrimination of LMA0 and LMA2 is considerably better than for Rate+Shape only. Both are excluded at CL 2σ (95.4%) now but both are still present for CL 3σ (99.73%).

8.3 Rate+Shape+Time Oscillation Analysis with no 2.6 MeV threshold

For that analysis, the prompt energy selection has been changed to: $0.9MeV < E_{prompt} < 8.9MeV$. Other selection rules are the same as in the two previous studies. Rate+Shape+Time fit was used. Terrestrial antineutrino fluxes were released in the fit, so, technically, this analysis can be considered "combined". However the resulting accuracy of geo-neutrino parameter estimation is so low that this study makes sense only for reactor $\bar{\nu}_e$ oscillation studies.

The result is shown in Figure 8.3.

A radical improvement is achieved by the expansion of the prompt energy area and performing the combined analysis. First, both LMA0 and LMA2 are gone at 99.73% CL. Second, the allowed regions are much narrower in LMA1.

This analysis gives $7.64^{+0.21}_{-0.20} eV^2$ for Δm^2_{12} and 0.84 for $\sin^2(2\theta)$.

Since only the LMA1 is relevant now, its plot at bigger scale is provided in Figure 8.4.

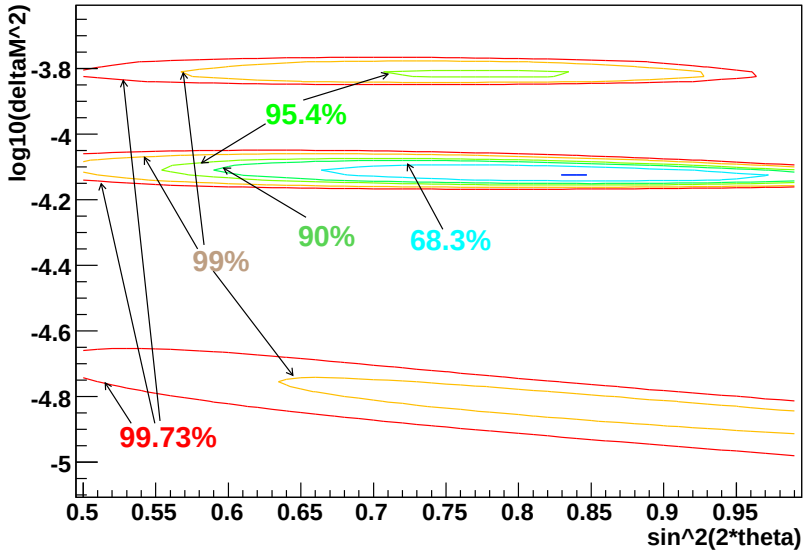

Figure 8.1: Oscillation parameters by Rate+Shape analysis with 2.6 MeV energy threshold. LMA0 (lower), LMA1 (center), LMA2 (top) are present at 99% CL.

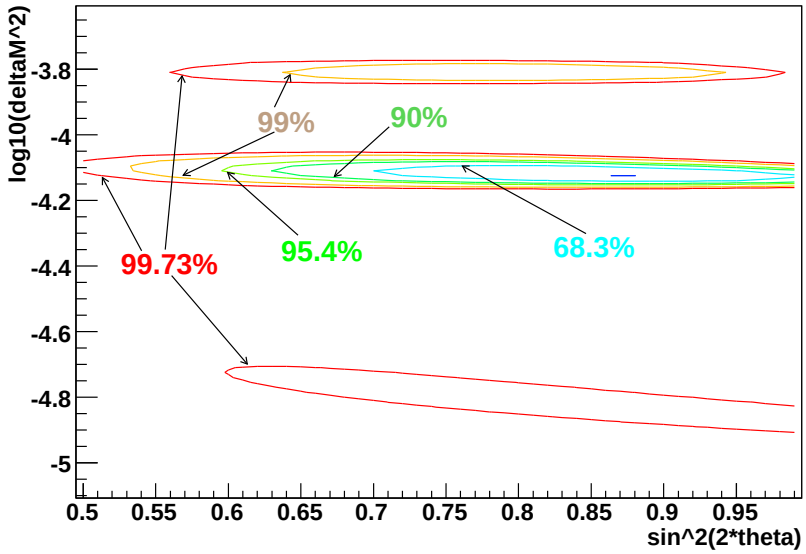

Figure 8.2: Oscillation parameters by Rate+Shape+Time analysis with 2.6 MeV energy threshold. LMA0,2 are relatively disfavored but still present at 99-99.73% CL.

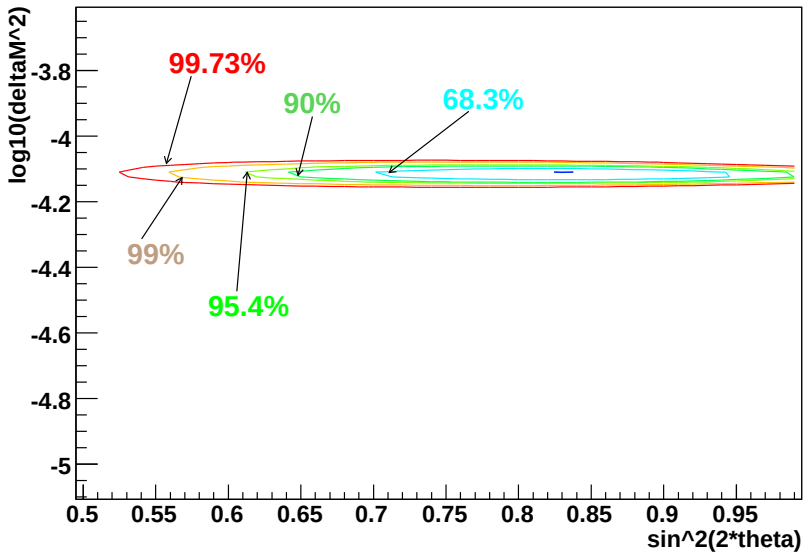

Figure 8.3: Oscillation parameters by Rate+Shape+Time analysis with 0.9 MeV energy threshold. LMA0,2 are excluded at 99.73% (3σ) CL.

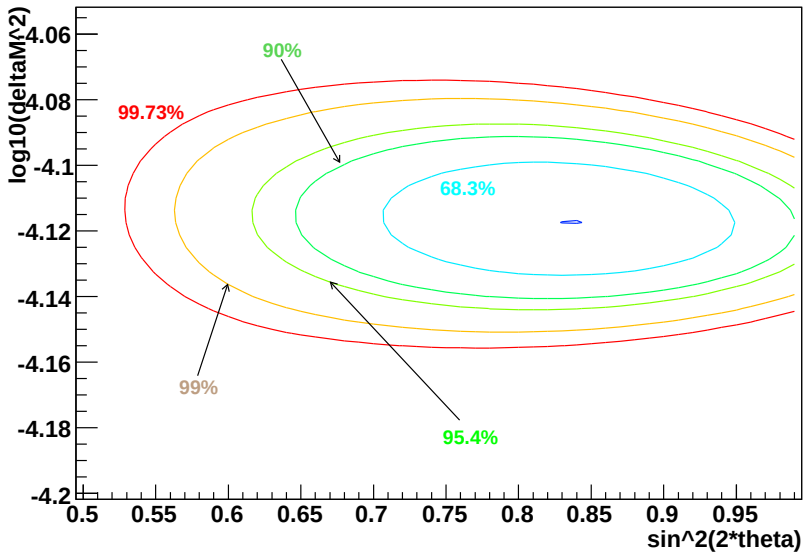

Figure 8.4: Oscillation parameters by Rate+Shape+Time analysis with 0.9 MeV energy threshold, LMA1 area.

However the simple Rate+Shape+Time combined analysis with 550 cm or wider fiducial cut does not allow to obtain an equally good result for terrestrial antineutrinos because they are completely overwhelmed by accidentals which can not be discriminated well within this likelihood model. That's where differential analysis becomes really necessary.

8.4 Differential Combined Analysis Oscillation and Terrestrial Results

Differential likelihood approach developed in Chapter 7 allowed to expand fiducial volume without the loss of accuracy due to the dramatically increased number of accidental coincidences, resulting in further improvement for the oscillation parameter study. Additionally, it allowed an improved geo-neutrino study for the following criteria which otherwise would have been impractical:

- Fiducial cut: $R_{prompt} < 575cm$, $R_{delayed} < 575cm$
- Space Separation cut: $\Delta R < 200cm$
- Time Separation cut: $0.5\mu s < \Delta T < 1000\mu s$
- Prompt Energy: $0.9MeV < E_{prompt} < 8.9MeV$
- Delayed Energy: $1.8MeV < E_{prompt} < 2.6MeV$

The muon veto policy was the same as in the previous analysis. The oscillation result is presented in Figures 8.5 and 8.6.

Because it has involved the most sophisticated and accurate analysis procedure used in this work, this result is considered the final antineutrino oscillation result of this thesis.

The best fit point is: $\sin^2 2\theta = 0.916$ and $\Delta m^2 = 7.52 \times 10^{-5} eV^2$. The 1σ CL allowed region for Δm^2 is $7.52^{+0.19}_{-0.18} \times 10^{-5} eV^2$; for CL of 3σ, it is $7.52^{+0.61}_{-0.53} \times 10^{-5} eV^2$. The result is consistent with the one presented in KamLAND Second Oscillation Result [52] but has much higher accuracy (about 1.9 times). Note that the longer exposure time used in this work could have statistically resulted in only 1.35-time improvement at best. The rest of the improvement has been obtained through a more sophisticated analysis used in this thesis.

The result of terrestrial antineutrino analysis are presented in Figure 8.7. The best estimation for the total terrestrial $\bar{\nu}_e$ flux is $46.6^{+19.9}_{-19.2}$ TNU for the unconstrained ratio of $\bar{\nu}_e$ fluxes from Radium to Thorium decay series. If the ratio is constrained to the 3.9 suggested by the geochemical data, the estimation of the total flux becomes $53.8^{+17.9}_{-16.8}$. Both are consistent with the earlier KamLAND publication [48] but the limits are narrower. The statistical significance of the geo-neutrino signal is above

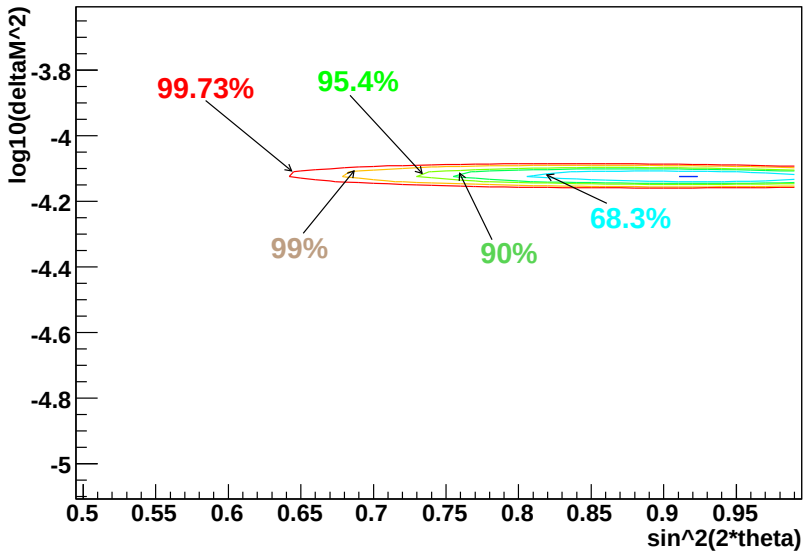

Figure 8.5: Oscillation parameters by differential likelihood analysis. LMA0,2 are excluded at 99.73% (3σ) CL.

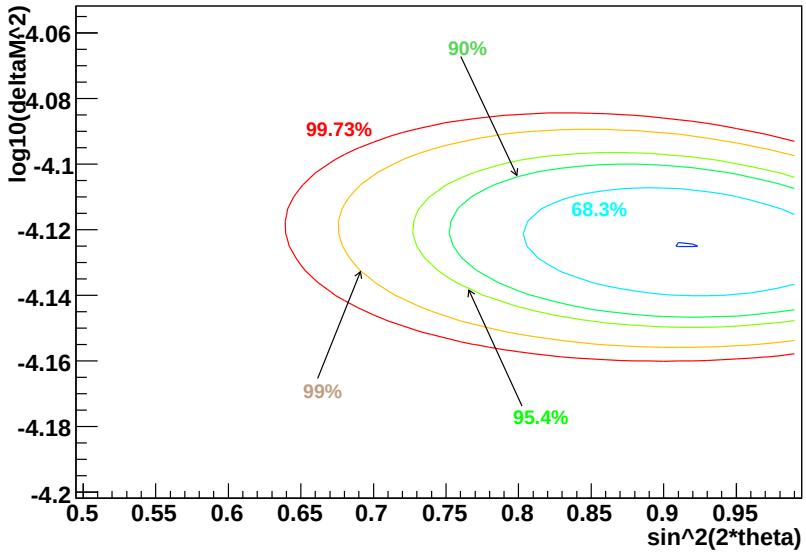

Figure 8.6: Oscillation parameters by differential likelihood analysis, LMA1 area.

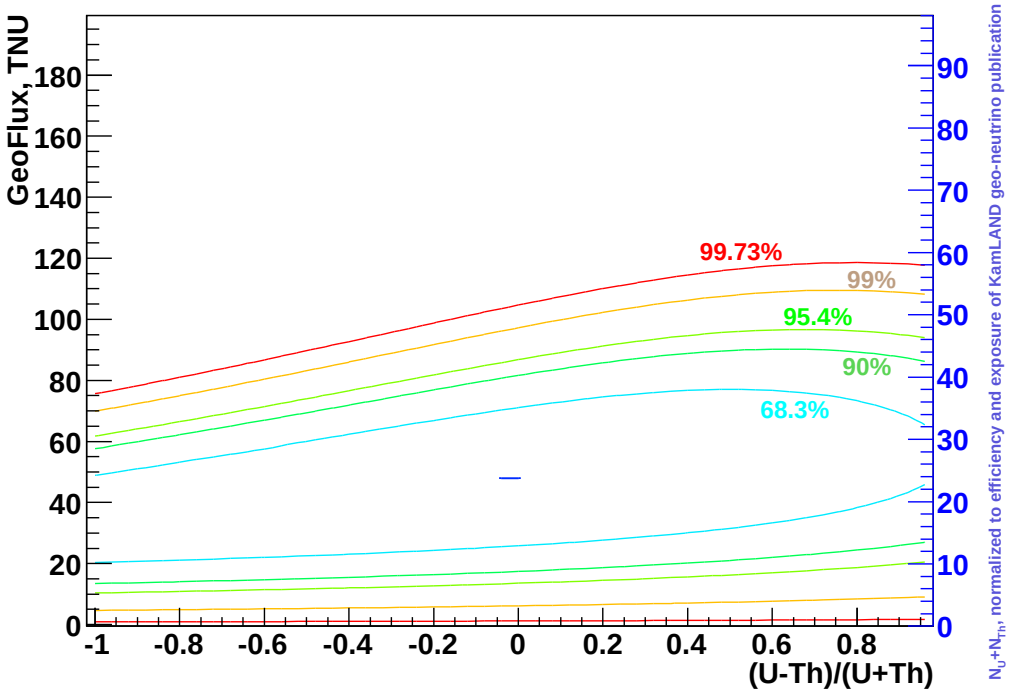

Figure 8.7: Terrestrial antineutrino parameters obtained by combined differential analysis. The right axis represents the number of geoneutrinos that would have been observed with the exposition and detection efficiency of [48] and provided for the direct comparison with the published result. The actual estimated number of terrestrial antineutrinos in this study is more than twice as high.

99.73% (3σ CL), so no geo-neutrino hypothesis can be considered experimentally excluded.

Although this improved accuracy is still not enough to exclude the fully radiogenic model, this is a significant improvement over [48] achieved at a moderately longer exposition (944.4 vs 749.1 days). At 3σ CL, the upper limit for total radiogenic heat (assuming the model developed in [53]) is now approximately 45.5 TW. This is still larger than the measured total heat produced by the Earth.

Chapter 9

Conclusions

Last years have been marked with a remarkable progress in neutrino physics. Not only the phenomenon of neutrino oscillation has been conclusively proven in atmospheric, solar, reactor and accelerator neutrino experiments, but also first estimations for oscillation parameters were obtained. The KamLAND experiment played one of most prominent roles in this development. It was first to observe the oscillations of reactor antineutrinos (and any man-made source of $\bar{\nu}_e$ in general), the paper reporting this result becoming one of the most cited publications in particle physics [51]. Later KamLAND provided a far better accuracy for the Δm_{12} [52] than any existing experiment could provide, starting an era of precision neutrino physics. KamLAND was also first to detect geologically produced antineutrinos [48], pioneering neutrino geophysics.

The work described in this thesis is representative of an advanced stage of data analysis performed by KamLAND collaboration. It is based on longer exposition and enhanced analysis tools and methods, leading to the substantially higher accuracy of parameter estimation. In particular, new values for Δm^2_{12} and for the geo-neutrino flux have been obtained which are consistent with but more precise than the previously published by KamLAND collaboration. The longer observation period was an important but not the main factor that contributed to the improvement. As has been shown in Chapter 8, the analysis performed in the same way as KamLAND reactor oscillation result [52] but using 944.4 instead of 515.1 days of pure live time yields only 1.25-1.3 times better accuracy. It was the new methods of analysis that provided the rest of the improvement towards the 1.9 times more precise estimation of Δm^2_{12}.

The main results of this work for reactor antineutrino studies are the following: both "satellite" LMA regions, namely LMA0 and LMA2 are now excluded at over 3σ CL, effectively limiting the area of allowable solutions to the LMA1 sub-region only. Within the LMA1 region a more precise estimation for Δm^2_{12} is obtained, which is $7.52^{+0.19}_{-0.18} \times 10^{-5} eV^2$. For reference, the traditional Rate+Shape analysis performed on the same data gives $7.57^{+0.30}_{-0.26} \times 10^{-5} eV^2$ and no exclusion of either LMA0 or LMA2 at 3σ CL.

It has been shown that the major improvement for the oscillation study came from the inclusion of the low energy area from 0.9 to 2.6 MeV of E_{vis} which contains important information about the oscillations. The fiducial volume enlargement made possible by the differential likelihood method described in this thesis and Rate+Shape+Time analysis provided a smaller but quite adequate enhancement.

For the geo-neutrino part of the study, there was no energy range expansion option but relatively more improvements were facilitated by the differential likelihood approach. The larger fiducial volume and higher selection efficiency enabled to decrease statistical error and obtain a much more accurate estimation for the geo-neutrino flux than previously reported. In particular, this work provides a narrower confidence range for CL 99% than [48] does for 90% and excludes the no "geo-neutrino" hypothesis at CL 3σ (99.73%), regardless of whether the ratio of "Uranium" to "Thorium" geo-neutrinos is constrained according to geochemical data or not. The current best estimation for terrestrial $\bar{\nu}_e$ flux from Thorium and Radium decay series is $53.8^{+17.9}_{-16.8}$ TNU (Terrestrial Neutrino Units, i.e. $\bar{\nu}_e$ interactions per 10^{32} protons per year) if "Uranium/Thorium" ratio is constrained at geochemically predicted 3.9, and $46.6^{+19.9}_{-19.2}$ TNU if the ratio is considered unknown and is released.

It has been also demonstrated that even with extremely heavy backgrounds, comparable or exceeding the main signal, it still may be possible to make precise parameter evaluations. In particular, accidental coincidence rate alone is estimated to be comparable to the reactor $\bar{\nu}_e$ signal and exceeding the terrestrial $\bar{\nu}_e$ event by more than an order of magnitude, which didn't prevent from making the precise measurement of the parameters.

The considerable improvement for the Δm^2_{12} over the KamLAND result of 2005 which has been by far most accurate estimation for this value is yet another demonstration of the great potential of KamLAND. At the moment of writing, KamLAND detector is undergoing purification, which will dramatically decrease accidental and alpha-n backgrounds. This will open new possibilities, including the observation of solar ^7Be neutrinos and more precise geo-neutrino studies.

Bibliography

Bibliography

[1] W. Pauli. Letter to L. Meitner and her colleagues (letter open to the participants of the conference in Tubingen) (1930).

[2] F. Reines and C. L. Cowan, Jr., Phys. Rev. **92**, 830 (1953).

[3] G. Danby *et al.*, Phys. Rev. Lett. **9**, 36 (1962).

[4] R. Davis, Jr., *et al.*, Phys. Rev. Lett. 20, 1205 (1968).

[5] K. Kodama *et al.* [DONUT Collaboration], Phys. Lett. B **504**, 218 (2001).

[6] Particle Data Group 2006, http://pdg.lbl.gov

[7] V. M. Lobashev *et al.*, Phys. Lett. B **460**, 227 (1999).

[8] Ch. Kraus *et al.*, Eur. Phys. J. **40** (2005) 447.

[9] B. Pontecorvo, Sov. Phys. JETP **6**, 429 (1958).

[10] B. Pontecorvo, Sov. Phys. JETP **7**, 172 (1959).

[11] Z. Maki, M. Nakagawa and S. Sakata, Prog. Theor. Phys. **28**, 870 (1962).

[12] M Kobayashi and T. Masukawa, Prog. Theor. Phys. **16**, 870 (1973).

[13] Particle Data Group 2002, http://pdg.lbl.gov

[14] L. Wolfenstein, Phys. Rev. D **17**, 2369 (1978).

[15] S. P. Mikheev and A. Yu. Smirnov, Sov. J. Nucl. Phys. **42**, 913 (1985).

[16] J. N. Bahcall, S. Basu, M. H. Pinsonneault, Phys. Lett. B **433**, 1 (1998).

[17] J. N. Bahcall, A. M. Serenelli, S. Basu, ApJ, **621**, L85 (2005).

[18] W. Hampel *et al.*, Phys. Rev. Lett. B **447**, 127 (1999).

[19] M. Altmann *et al.*, Phys. Lett. B **490**, 16 (2000).

[20] J. N. Abdurashitov *et al.*, JETP **95**, 181(2002).

[21] Y. Fukuda *et al.*, Phys. Rev. Lett. **77**, 1683 (1996).

[22] S. Fukuda *et al.*, Phys. Lett. B **539**, 179 (2002).

[23] Ahmad, Q. R. *et al.*, Phys. Rev. Lett. **89** 011301 (2002).

[24] S. N. Ahmed *et al.*, Phys. Rev. Lett. **92**, 181301 (2004).

[25] B. Aharmim *et al.*, Phys. Rev. **C72** 055502 (2005).

[26] K. S. Hirata *et al.*, Phys. Lett. B **280**, 146 (1992).

[27] R. A. Becker-Szendy *et al.*, Phys. Rev. D **46**, 3720 (1992).

[28] W. W. M. Allison *et al.*, Phys. Lett. B **449**, 137 (1999).

[29] M. Aglietta *et al.*, Europhys. Lett. **8**, 611 (1989).

[30] K. Daum *et al.*, Z. Phys. **C66**, 417 (1995).

[31] M.Ishitsuka, for the Super-Kamiokande Collaboration, hep-ex/0406076 (2004).

[32] M. H. Ahn *et al*, Phys. Rev. Lett. **90**, 041801 (2003).

[33] A. O. Bazarko, hep-ex/0210020.

[34] C. Athanassopoulos *et al.*, Phys. Rev. **C58**, 2489 (1998).

[35] B. Armbruster *et al.*, Phys. Rev. **D65**, 112001 (2002).

[36] P. Adamson *et al. (MINOS)*, Phys. Rev. **D73** (2006) 072002.

[37] M. H. Ahn *et al*, hep-ex/0606032 (2006).

[38] H. Kwon *et al.*, Phys. Rev. **D24**, 1097 (1981).

[39] Z. D. Greenwood *et al.*, Phys. Rev. **D53**, 6054 (1996).

[40] Y. Declais *et al.* (Bugey), Nucl. Phys. **B434**, 503 (1995).

[41] A. I. Afonin *et al.*, JETP Lett. **45**, 247 (1987).

[42] G. Zacek *et al.* (CalTech-SIN-TUM), Phys. Rev. **D34**, 262 (1986).

[43] G. S. Vidyakin *et al.*, JETP Lett. **59**, 390 (1994).

[44] F. Boehm *et al.* (Palo Verde), Phys. Rev. **D64**, 112001 (2001)

[45] M. Apollonio *et al.*, Eur. Phys. J. C **27**, 331 (2003).

[46] J. M. Herndon, Proc. Nat. Acad. Sci. **93**, 646 (1996).

[47] D. F. Hollenbach and J. M. Herndon, Proc. Nat. Acad. Sci. **98**, 11085 (2001).

[48] T. Araki *et al.*, "Experimental investigation of geologically produced antineutrinos with KamLAND", Nature **436**, 499 (2005).

[49] H. Murayama, http://hitoshi.berkeley.edu/neutrino, based on M. B. Smy, hep-ex/0208004

[50] International Nuclear Safety Center Web Page, http://www.insc.anl.gov (2006).

[51] K. Eguchi *et al.*, Phys. Rev. Lett. **90**, 021802 (2003).

[52] T. Araki *et al.*, Phys. Rev. Lett. **94**, 081801 (2005).

[53] S. Enomoto. "Neutrino Geophysics and Observation of Geo-neutrinos at KamLAND". Thesis, Tohoku Univ. (2005), http://www.awa.tohoku.ac.jp/KamLAND/publications/Sanshiro_thesis.pdf

[54] K. Shreckenbach *et al.*, Phys. Lett. **B160** 325 (1985).

[55] P. Vogel *et al.*, Phys. Rev. **C24** 1543 (1981).

[56] A.A.Hahn *et al.*, Phys. Lett. **B218** 365 (1989).

[57] V. I. Kopeikin *et al.*, Physics of Atomic Nuclei **64**, 849-854 (2001).

[58] P. Vogel, J. F. Beacom "Angular distribution of neutron inverese beta decay $\bar{\nu}_e + p \to e^+ + n$", Phys. Rev. D **60**, 053003 (1999).

[59] LBNL Isotopes Project, http://ie.lbl.gov/toi

[60] N. R. Tolich. "Experimental Study of Terrestrial Electron Anti-Neutrinos with KamLAND", Thesis, Stanford Univ. (2005), available at http://www.awa.tohoku.ac.jp/KamLAND/publications/Nikolai_thesis.pdf

[61] G. Eder, Nucl. Phys. **78**, 657 (1966).

[62] G. Marx, Czech. J. Phys. **B19**, 1471 (1969).

[63] W. F. McDonough and S.-s. Sun, "The Composition of the Earth", Chemical Geology **120**, 223 (1995).

[64] S. R. Taylor and S. M. McLennan., "The Continental Crust: its Composition and Evolution", Blackwell Oxford (1985).

[65] G. Schubert, D. L. Turcotte, and P. Olson, "Mantle Convection in the Earth and Planets", Cambridge University Press, Cambridge (2001).

[66] H. N. Pollack, *et al.*, Rev. Geophys. **31**, 267 (1993).

[67] A. M. Hofmeister *et al.*, Tectonophysics **395**, 159 (2005).

[68] T. Iwamoto. "Measurement of Reactor Anti-Neutrino Disappearance in KamLAND". Thesis, Tohoku Univ. (2003). http://www.awa.tohoku.ac.jp/KamLAND/articles/PhD/PhD-iwamoto.pdf

[69] JENDL (α, n) Reaction Data File, 2003, JAERI.

[70] A. Stuart *et al.*, "Kendall's Advanced Theory of Statistics", Oxford University Press (1999).

[71] G. Cowan, "Statistical Data Analysis", Oxford Science Publications (1998).

[72] R. S. Raghavan 2002, arXiv:hep-ex/0208038 (Aug 2002).

[73] M. Apollonio *et al.*, Phys. Rev. D **61** 012001 (2000).

[74] M. Batygov, "On the Possibility of Directional Analysis for Geo-neutrinos ", Proceedings of 2005 Neutrino Sciences Conference, to be published.

Appendix

Appendix A

V2 Vertex Fitter

V2 is a time-based vertex fitter developed for KamLAND in order to improve vertex resolution and systematic biases in the whole range of relevant energies, including the sub-1MeV range that is currently used mostly for background studies but will be critical in the next solar stage of KamLAND experiment.

V2 applies maximum likelihood approach to the timing information available from KamLAND TQ algorithms (Section 3.1). PMT hit pattern is also used for the "pre-fit" to find the starting point from which the iterative process of likelihood maximization starts. However the hit pattern doesn't enter the likelihood expression, explicitly or implicitly and doesn't affect the accuracy of the vertex finding, so V2 can be considered a "pure" time-based fitter. Charge information is not used in V2.

Time-based vertex finding uses the fact that the speed of light propagation is in the scintillator is finite. The PMTs close to the source of light get the signal earlier than the ones far from it. If there were no signal arrival time spread, four PMTs would have been enough for an absolutely accurate vertex reconstruction in (3+1)-dimensional space (3 spatial coordinates + time). In reality, the time arrival is a rather wide distribution, with characteristic spread on the order of several nanoseconds (which directly translates to meters of positional error). Part of it is introduced by the TTS (Transition Time Spread) of the PMT and the TQ algorithms but most is due to the properties of the liquid scintillator which has a long "tail" in the time distribution of its light deposition.

The resulting distribution of TQ-reconstructed hit time is called "pulse shape" and generally depends on the PMT type, distance from the source to PMT, the intensity of the signal, the origin of the signal (gamma, beta, neutron, positron) and the distance traveled through the scintillator. Source calibrations allow to collect those pulse shapes for different combinations of the aforementioned parameters, which can be used for the high precision vertex reconstruction. The distinctive feature of V2 which enabled superior resolution and low biases is the use actual experimental pulse shapes obtained with KamLAND data. Earlier vertex fitters either relied on models or implicitly assumed Gaussian pulse shapes.

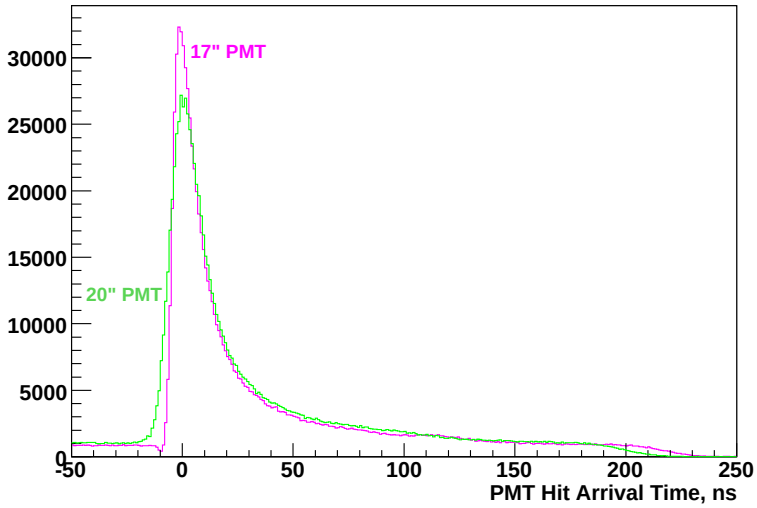

Figure A.1: Typical pulse shapes. Obtained with a gamma source (^{203}Hg) calibration for 17" and 20" PMTs. Note the much sharper rise of the 17" shape determined by the shorter TTS of those PMTs. The tails are determined mostly by the properties of the scintillator and are more alike.

Typical pulse shapes collected with a source calibration are shown if Figure A.1. The shapes are clearly not Gaussian, which explains why some earlier vertex fitter assuming a normally distributed hit arrival time had to apply tight cuts to the area near the peak in order to achieve good accuracy. There is a considerable shape difference between 17" and 20" PMT explained by different transition time spreads (TTS) of those tubes and by different afterpulsing properties. The V2 fitter takes this fact into account and treats 17" and 20" PMTs separately, according to their respective pulse shapes.

It is worth mentioning that pulse shapes depend on the position of the source, the distance from the source to the PMT, the intensity of the signal and its physical origin. Alpha events give different pulse shapes from betas and gammas. The dependence on the distance and the intensity is dominant. The V2 fitter uses the "averaged" pulse shapes but introduces special time shift corrections to compensate for the possible mismatch. Those corrections have been obtained through source calibrations as well.

V2 uses the maximum likelihood (ML) approach described in Chapter 7 but applies it to the more "local" problem of locating the signal source. This fitting procedure for a time based vertex fitter actually evaluates 4 parameters: 3 spatial coordinates and the origin time.

The values that connect the experimentally observable PMT hit timings with the pulse shapes used in the likelihood are τ_i that represent the delays of the signal timings

compared to the expectations calculated for some x, y, z, t:

$$\tau_i = t_i - t - TOF_i \tag{A.1}$$

where t_i is the observed timing in the i-th PMT and TOF_i (for Time Of Flight) is the distance from the point (x, y, z) to the i-th PMT divided by the speed of light in the scintillator.

The likelihood that takes into account only the signal timing and ignores charge and hit pattern information can be written as:

$$L = \prod_{i=hit} \varphi(\tau_i(x, y, z, t)) \tag{A.2}$$

where the multiplication is made only over the PMTs that were hit and had a signal, τ_i is the signal's delay according to the current values of x, y, z, t under inspection and $\varphi(\tau_i)$ is a pulse shape evaluated at τ_i calculated as in (A.1).

As usual, the logarithm of the likelihood is more convenient for computations than its actual value:

$$\log(L) = \sum_{i=hit} \log(\varphi(\tau_i(x, y, z, t))) \tag{A.3}$$

Starting from this point, it's possible simply to call MINUIT or any other standard minimization routine and fine the combination of x, y, z, t that deliver the maximum to (A.3). However, the severe requirements for the speed of operation on one hand and relatively simple form of the likelihood on the other made it practical to develop a custom minimization/maximization procedure.

The maximum of the (A.3) is achieved at a point where its 4-dimensional gradient turns into zero, i.e. partial derivatives with respect to x, y, z and t all vanish:

$$\begin{cases} \frac{\partial(log(L))}{\partial x} = 0 \\ \frac{\partial(log(L))}{\partial y} = 0 \\ \frac{\partial(log(L))}{\partial z} = 0 \\ \frac{\partial(log(L))}{\partial t} = 0 \end{cases} \tag{A.4}$$

or, more explicitly,

$$\begin{cases} \sum_{i=hit} \frac{d(log(\varphi(\tau_i)))}{d\tau_i} \frac{\partial \tau_i}{\partial x} = 0 \\ \sum_{i=hit} \frac{d(log(\varphi(\tau_i)))}{d\tau_i} \frac{\partial \tau_i}{\partial y} = 0 \\ \sum_{i=hit} \frac{d(log(\varphi(\tau_i)))}{d\tau_i} \frac{\partial \tau_i}{\partial z} = 0 \\ \sum_{i=hit} \frac{d(log(\varphi(\tau_i)))}{d\tau_i} \frac{\partial \tau_i}{\partial t} = 0 \end{cases} \tag{A.5}$$

Since $\frac{d\log(f(\xi))}{d\xi} = \frac{1}{f(\xi)}\frac{df(\xi)}{d\xi}$, (A.5) can be rewritten as:

$$\begin{cases} \sum_{i=hit} \frac{1}{\varphi(\tau_i)} \frac{d\varphi(\tau_i)}{d\tau_i} \frac{\partial \tau_i}{\partial x} = 0 \\ \sum_{i=hit} \frac{1}{\varphi(\tau_i)} \frac{d\varphi(\tau_i)}{d\tau_i} \frac{\partial \tau_i}{\partial y} = 0 \\ \sum_{i=hit} \frac{1}{\varphi(\tau_i)} \frac{d\varphi(\tau_i)}{d\tau_i} \frac{\partial \tau_i}{\partial z} = 0 \\ \sum_{i=hit} \frac{1}{\varphi(\tau_i)} \frac{d\varphi(\tau_i)}{d\tau_i} \frac{\partial \tau_i}{\partial t} = 0 \end{cases} \tag{A.6}$$

The system (A.6) can be solved efficiently by an iterative procedure. The V2 fitter uses the steepest descent approach to find the solution. The direction of the fastest change of the likelihood logarithm (i.e. its gradient) is taken for every new step. The length of the step is chosen according to a modified Newton-Raphson method, which involves the calculation of the second partial derivatives of the likelihood as well. However since this differentiation involves only the pulse shape function which is a function of only one argument, τ, its first and second derivatives are pre-calculated and stored in the tables. So the likelihood differentiation largely reduces to little more than a table lookup, interpolation and summation, which are fast operations on modern computers. In fact the most expensive part involved the vertex fitting is associated with the partial derivatives of τ_i with respect to spatial coordinates. This part involves the calculation of the square root that is more than 1 order of magnitude slower than multiplications and additions.

The iterative procedures stops when the next step is smaller than some predefined value or if the maximum number of iterations is reached.

The performance of the V2 fitter has been extensively studied at both the University of Tennessee and RCNS of the Tohoku University. The results of some of the bias and resolution tests involving source calibrations along the Z-axis are shown in Figures A.2, A.3.

For visible energies above 1 MeV, the V2 fitter has the maximum Z-axis bias not more than 3 cm. The "raw" vertex reconstruction resolution is estimated to be $12.1cm/\sqrt{E_{vis}[MeV]}$ in this energy range, which is used in the likelihood analysis for space separation distribution.

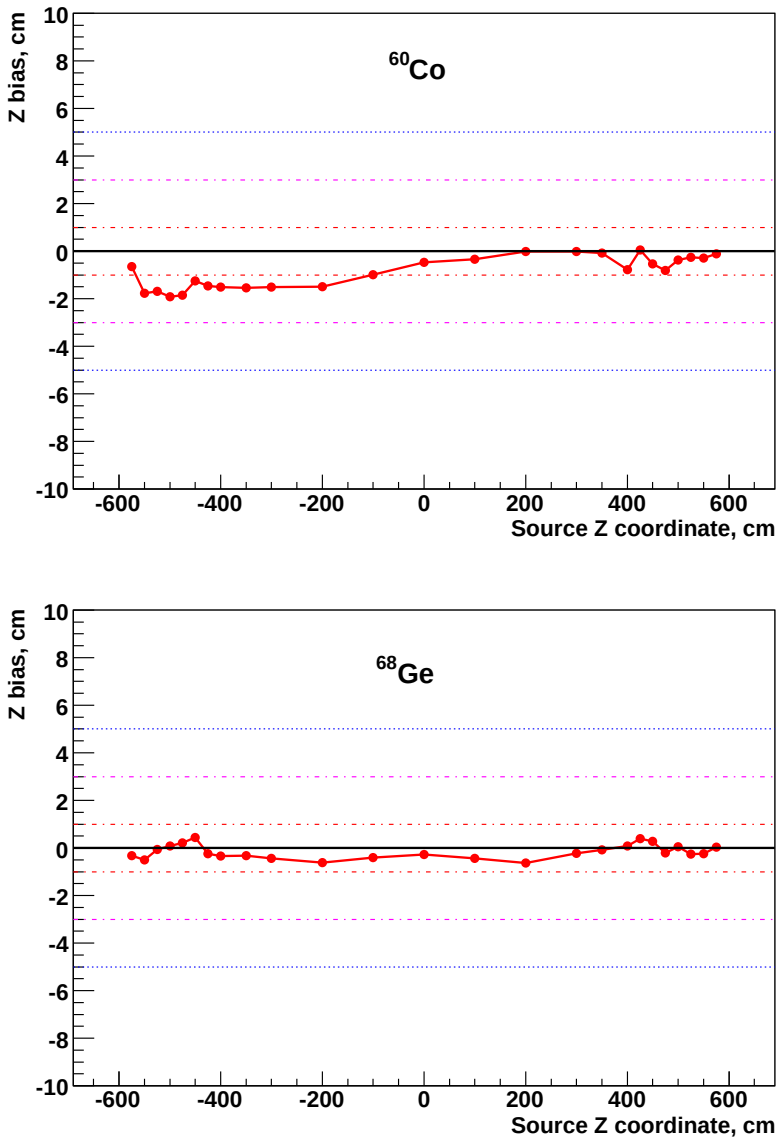

Figure A.2: V2 fitter bias tests. ^{60}Co and ^{68}Ge calibrations along the Z-axis.

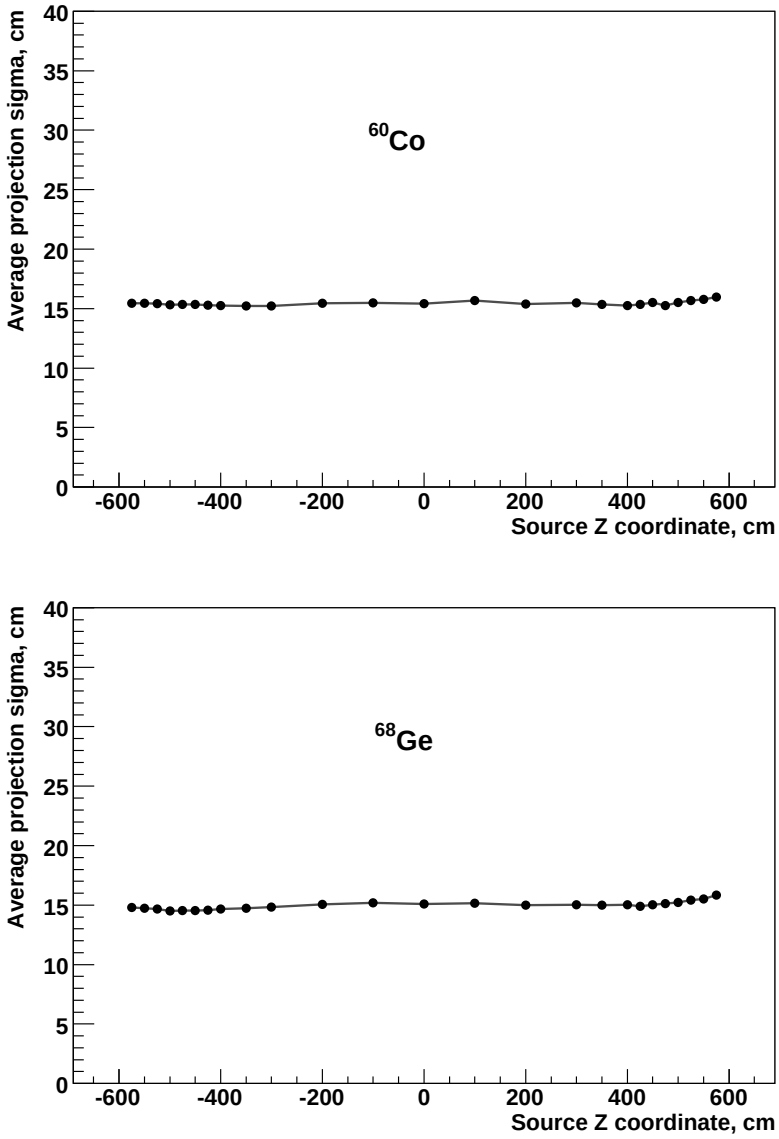

Figure A.3: The V2 fitter resolution tests. ^{60}Co and ^{68}Ge calibrations along the Z-axis.

Appendix B

Possibility of Antineutrino Direction Reconstruction in LS $\bar{\nu}_e$ Detectors

The measurement of the incident antineutrino direction distribution in addition to their energy spectrum would have been an important enhancement. The biggest gains can be achieved for terrestrial antineutrino studies. Directionality can help to distinguish between different geological models which predict different distribution of radioactive isotopes in the Earth. Additionally, the geo-reactor hypothesis can be tested in a very direct way, which was noted in [72].

While the gains of directionality measurement were quite obvious, its practical possibility with KamLAND has been unclear. To answer this question, a special study had to be done.

A successful directionality measurement with a liquid scintillator antineutrino detector had been performed by CHOOZ collaboration [73]. However, a different composition of LS (Gadolinium loaded) was used, which gave different energy deposition distributions from what one could expect from KamLAND. Besides, CHOOZ experiment had thousands of events from the rather closely located reactors, which is much more than KamLAND has from terrestrial sources, so the results of that experiment can not be directly applied to KamLAND.

The goal was to determine whether a practical directionality study of geo-neutrinos was possible with KamLAND and if not, what the requirements the future similar detectors must satisfy to be capable of such measurements. This study has been performed for the 2005 Neutrino Sciences conference and can be found in its proceedings [74]. An abridged account of that study is presented below.

The possibility for directionality measurement follows from the properties of the inverse beta decay reaction (1.1). The direction from the prompt signal coordinate to the delayed one is correlated with the direction of the incident antineutrino. This correlation is quite weak, though, so the detection of antineutrino directions on the event-by-event basis is impossible. However, given enough events for the distribution

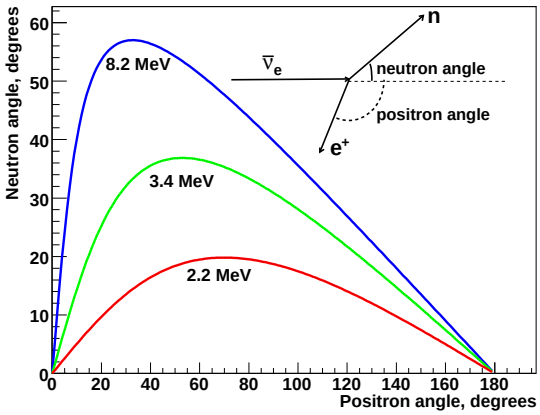

Figure B.1: Neutron direction as a function of positron direction for $\bar{\nu}_e$ energies 2.2, 3.4, 8.2 MeV.

unfolding, it may still be feasible to extract the antineutrino direction distribution function statistically.

The origin of this directional correlation lies in the kinematics of the inverse β-decay. The relativistic 4-vector momentum conservation equations:

$$p^{\mu}_{\bar{\nu}_e} + p^{\mu}_{p} = p^{\mu}_{e^+} + p^{\mu}_{n}, \tag{B.1}$$

where $\mu = 0, 1, 2, 3$ can be satisfied for any positron scattering angle, from 0 to 180 degrees. Given the initial $\bar{\nu}_e$ energy and this angle, the kinetic energies of both neutron and positron, as well as the neutron angle, are determined from (B.1). The relationship between the positron and the neutron scattering angles is shown in Figure B.1. Note that the component of neutron momentum in the direction of the incident $\bar{\nu}_e$ is always positive. In other words, neutrons cannot "backscatter" in the inverse-beta reaction. This property is the key to the directionality measurement.

The distribution of positron angles can be calculated [58]. It is almost uniform with a slight preference for "backscattering". This study uses the approximation:

$$\frac{d\sigma}{d\cos\xi} \propto 1 - 0.102\beta\cos\xi, \tag{B.2}$$

where σ is the cross section of the reaction, β is the positron velocity in terms of the speed of light and ξ is the scattering angle.

Starting with this distribution, a Monte-Carlo simulation can be used to generate and track positrons and neutrons according to given $\bar{\nu}_e$ energies, exactly like it has been done to find the space separation distributions in section 7.10.

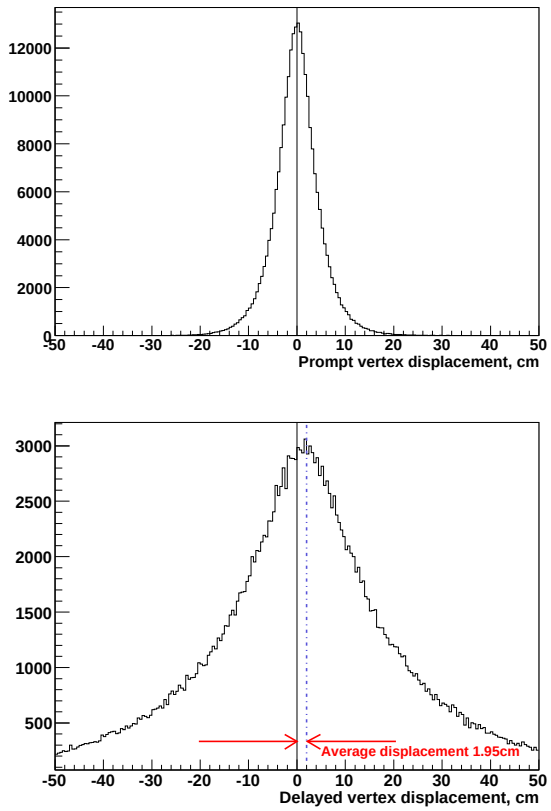

Figure B.2: Displacements of the prompt and delayed signals from the origin. Simulated for $E_{\bar{\nu}_e}$=2.6 MeV. The delayed signal is displaced by 1.95 cm in the direction of the incident $\bar{\nu}_e$. [74]

Upon fairly general assumptions, the vertex reconstruction resolution is inversely proportional to the square root of "Visible Energy" (essentially the number of detectable photons generated in the event): $\sigma = k/\sqrt{E_{vis}}$, which has been confirmed in KamLAND. The coefficient "k" characterizes the quality of vertex reconstruction and depends on many factors, including the detector design, the scintillator composition, the quality of photomultiplier tubes and electronics, the size of the detector and the accuracy of the reconstruction algorithms. As was mentioned above, the current KamLAND vertex fitter has the resolution about $12cm/\sqrt{E_{vis}[MeV]}$ but future detectors may be better or worse in this respect, so some simulations were performed for a set of different vertex resolutions to study the influence of this parameter on directionality measurement.

A simulation of absolute displacements for low-energy $\bar{\nu}_e$ signals, without vertex reconstruction smearing (i.e. perfect vertex reconstruction) is shown in Figure B.2. The prompt signal does not show appreciable systematic deviation from the origin.

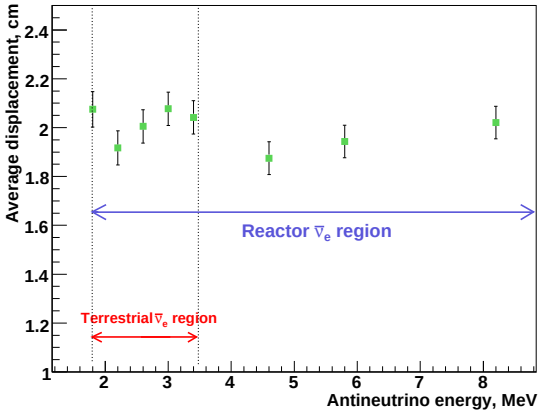

Figure B.3: Prompt-to-Delayed vertex displacement. Simulated for reconstruction resolution $12\text{cm}/\sqrt{E_{vis}[MeV]}$ for each projection as a function of $\bar{\nu}_e$ energy. Error bars shown correspond to $\text{RMS}/\sqrt{240,000}$ to account for the simulation accuracy. [74]

This is due to the fact that the distribution (B.2) is almost flat, while the free path of positrons in scintillator before annihilation is quite short. On the other hand, the delayed signal exhibits a clear bias in the direction of the incident antineutrino as expected. So does the vector between the prompt and delayed signal. Therefore the directionality analysis in an unloaded scintillator is, in principle, possible. When all antineutrinos come from a single source direction, the displacement of about 1.9-2.0 cm is expected. This is close to the 1.7 cm obtained in a similar simulation for the CHOOZ experiment [73]. The difference might be attributable to different scintillator composition.

The simulation of observable displacements smeared with vertex resolution equal to $12\text{cm}/\sqrt{E_{vis}[MeV]}$ in each projection (x, y, z) and is presented in Figure B.3. Long living isotopes emit almost no terrestrial antineutrinos with energies above 3.5 MeV, yet this work includes simulations for up to 8.2 MeV to cover most of the hypothetical geo-reactor spectrum as well. The displacement does not depend substantially on the antineutrino energy. Its spread decreases slightly with energy due to the better absolute resolution of the prompt signal but the effect is quite small.

In the simulation, 240,000 events were generated to achieve a statistically significant result. In a real experiment, this many may not be available. When the statistical error of the average displacement becomes comparable to or exceeds the displacement itself, no conclusion about the direction of incident antineutrinos can be made. In general, the question about the sufficient number of candidates is quite complicated and model dependent. Distinguishing between two geological models with similar directionality patterns would require more statistics than testing a relatively simple hypothesis.

Table B.1: Necessary event counts to test geo-reactor hypothesis for given confidence levels (CL) and different vertex reconstruction resolutions. Calculated in the assumption of the absence of background, the test using only the directionality information but no rate or spectrum shape. [74]

CL	Perfect vertex	12cm/$\sqrt{E_{vis}[MeV]}$	30cm/ $\sqrt{E_{vis}[MeV]}$
0.683	157	236	432
0.900	424	639	1171
0.950	600	905	1659
0.990	1036	1563	2863

Perhaps the easiest and the least demanding case here is a monodirectional $\bar{\nu}_e$ flux, e.g. the geo-reactor hypothesis test. The numbers of events necessary to test the hypothesis at different confidence levels (CL) are estimated according to the generated vertex distributions and presented in Table B.1. The table shows the number of $\bar{\nu}_e$ events necessary to test the geo-reactor hypothesis by means of directionality alone. Of course, from the practical point of view, this hypothesis can be tested by rate and spectrum shape analysis, which would probably require fewer events.

The "Perfect vertex" represents the "raw" signal displacement with no reconstruction smearing, just to show the absolute sensitivity limit of such a study. In real experiments finite smearing is unavoidable but, as was mentioned above, can vary substantially. A resolution of 30cm/$\sqrt{E_{vis}[MeV]}$ is presented in the table to illustrate the significance of reconstruction resolution. If the resolution is compromised to that level by the detector design or by other factors, then almost 2/3 of all statistics can be effectively lost for directionality purposes.

The absolute event numbers required for the directionality measurement are far too high to be practical with KamLAND, especially for geo-neutrino studies. During four years of operation, KamLAND has collected less than 1000 $\bar{\nu}_e$ candidates and more than 90% of them are reactor antineutrinos from nuclear power plants.

Moreover, the values in Table B.1 are obtained for an ideal, no-background scenario. In KamLAND, the biggest background source for terrestrial antineutrino studies is the reactor antineutrinos. Most other sources (uncorrelated accidental coincidences and the alpha-n correlated background) are caused by the presence of radioactive isotopes in the detector. Currently, they are smaller than but comparable to the reactor background. However, KamLAND expects to reduce them by several orders of magnitude through the detector purification. When this is completed those background sources will become negligible. On the other hand, the reactor $\bar{\nu}_e$ background is unavoidable for KamLAND geo-neutrino studies and the only way to minimize its impact in the future is to build new detectors further from working reactors. The effect of the background on the directionality measurement is similar to that of a finite vertex resolution: still more events are necessary for the same confidence level. Table

Table B.2: Necessary event counts to test geo-reactor hypothesis for given confidence levels (CL) and different background rates Calculated for the fixed vertex resolution of 12cm/$\sqrt{E_{vis}[MeV]}$, from the background-free case to the case when background exceed the geo-reactor signal by the factor of four. [74]

	Background to Signal Ratio						
CL	0.0	0.1	0.25	0.5	1.0	2.0	4.0
0.683	236	258	290	350	465	678	938
0.900	639	698	785	947	1260	1836	2542
0.950	905	988	1113	1342	1786	2602	3602
0.990	1563	1706	1921	2317	3083	4491	6219

B.2 provides the quantitative summary of such an effect for the equatorial spatial distribution of a $\bar{\nu}_e$ background.

Testing more sophisticated geological models and, in particular, the attempts to unfold the angular distribution of antineutrino directions would also require more events than can be found in Tables B.1, B.2.

The results of the simulation show that while directionality studies are possible with future antineutrino detectors with unloaded scintillators, KamLAND is too small for that and, additionally, located too close to the working reactors. Collecting a sufficient number of events from geological sources would require centuries of live time, even for the simplest studies and for ideal conditions.

Appendix C

Oscillated Reactor Spectrum Calculation Algorithm

The algorithm of the fast evaluation of spectrum distortion due to oscillations is based on the extensive use of look-up tables and features the complete exclusion of the flux summation over the reactors from the fitting process. Below, two methods representing this approach are described. Both have a promise of accelerating the calculations by at least an order of magnitude.

The first method ("A") has the advantage of being more universal, allowing for arbitrary reactor spectra. Its drawback is rather heavy system demands in terms of operative memory. Apart from limiting the range of applicable hardware, this property conditions somewhat slower operation due to the large fraction of cache misses.

The second one ("B") is more sophisticated and can work well with as little as 128 MB of operative memory, which is modest enough by today's standards. It can not handle arbitrary spectra, though. The rescue comes from the fact that reactor spectra, while being different and varying in time, are in fact not arbitrary. Instead, they can always be represented as a superposition of seven elementary spectra, i.e. the spectra from the fissions of ^{235}U, ^{238}U, ^{239}Pu and ^{241}Pu, and the decays of ^{90}Sr, ^{106}Rb and ^{144}Ce. For the reasons of convenience, this method was used in the antineutrino analysis presented here.

C.1 Method A

An naive attempt to tabulate all the relevant oscillation scenarios suggests a 4D table: RunNumber $\times E_{\bar{\nu}_e} \times \Delta m^2_{12} \times \sin^2(2\theta_{12})$. Such a huge table would be impractical, but there is really no need for 4D table. Looking at the survival probability formula (2-flavor oscillation case),

$$P(\nu_e \to \nu_e) = (1 - \sin^2(2\theta_{12}) \sin^2(\frac{1.27 \times \Delta m^2_{12} \times L}{E_{\bar{\nu}_e}})) \tag{C.1}$$

it's easy to notice that the dependence on the mixing angle is rather trivial.

The method suggests filling a 3D "oscillation loss" table for "all" combinations of run number (or time), $E_{\bar{\nu}_e}$, and Δm^2_{12} and whenever an oscillation loss estimation is needed, just look up in that table and then multiply the value by $\sin^2 2\theta_{12}$.

The memory requirements are quite heavy but not impossible. For $2000 \times 500 \times 500$ binning the 3D "oscillation loss" table takes 8 gigabytes with double precision (8 bytes per value), which is realistic for an entry-level server or a mid-class workstation, provided it's a 64-bit machine running a 64-bit OS (32-bit systems have a 4GB limit on the size of addressable RAM).

The suggested implementation is as follows.

Two tables are prepared beforehand, during the "compilation" phase. The first is a 2D "non-oscillated" table indexed in (RunNumber, $E_{\bar{\nu}_e}$). It is small compared to the second, "maximum oscillation loss" table which is a 3D indexed in (RunNumber, $E_{\bar{\nu}_e}$, Δm^2_{12}).

To recover the expected differential $\bar{\nu}_e$ flux at KamLAND site for a given run during the actual likelihood calculation, one needs to

- read the value indexed by this run and the chosen $E_{\bar{\nu}_e}$ from the "non-oscillated" table;
- read the value indexed by the run, the $E_{\bar{\nu}_e}$ and the current Δm^2_{12} from the "maximum oscillation loss" table;
- multiply the latter by the current $\sin^2 2\theta_{12}$;
- subtract the last result from the first item.

Despite the simple and straightforward nature of the operations involved in the run-time calculations, the method is not without its own weak points, all coming from the three-dimensionality of the "maximum oscillation loss" table and hence its huge size. First, some of the potential performance gains will be lost to high cache miss rates, since main memory access is not "free" and RAM runs many times slower than the CPU. Second, the inability to run on a common desktop and the rather imperative demand for a 64-bit OS can be a serious limitation.

An alternative method offers a way to get around this 3D table demand by taking the advantage of strictly "vertical" nature of oscillation distortions caused by oscillations.

C.2 Method B

The idea of the method comes from the observation that, for a given baseline, the oscillation loss is a function of the ratio of Δm^2_{12} to the $E_{\bar{\nu}_e}$, rather than some general function of the two parameters. This suggests indexing in just one value, $\frac{\Delta m^2_{12}}{E_{\bar{\nu}_e}}$

instead of two, ($E_{\bar{\nu}_e}$, Δm^2_{12}). After adding the dependence on the run number (or, equivalently, time), the "maximum oscillation loss" table becomes 2D.

This optimization comes at a price, however. First, the correctness of the method is not so transparent and it requires some algebra to prove that the method really works. Second, in fact it does not work for arbitrary reactor spectra and it has been believed for a while that this drawback was irrecoverable. The method is actually saved by the fact that the reactor spectra are linear combinations of fixed components and if this weren't the case the whole idea of imploding two dimensions into one would have been probably wasted.

To prove the correctness of the method, let's first consider the unrealistic scenario that we have the same spectrum for all reactors.

Each reactor indexed by k is then characterized only by its $\bar{\nu}_e$ intensity ($I_k(t)$) which is convenient to be expressed in such terms that the expected total $\bar{\nu_e}$ flux at unit (1 meter) distance is $\frac{I_k(t)}{1.0^2}$. The differential flux for given $\bar{\nu_e}$ and distance L_k (in meters) is $\phi(E_{\bar{\nu}_e})\frac{I_k(t)}{L_k^2}$, where $\phi(E_{\bar{\nu}_e})$ is the "universal" antineutrino energy spectrum normalized to 1.

The non-oscillated differential cumulative flux from all reactors is

$$\frac{dF}{dE_{\bar{\nu}_e}} \equiv \sum_k \frac{dF_k}{dE_{\bar{\nu}_e}} = \phi(E_{\bar{\nu}_e}) \sum_k \frac{I_k(t)}{L_k^2} \tag{C.2}$$

Oscillation distorts the spectrum by the non-uniform "suppression" of differential fluxes. For the k-th reactor we have

$$\frac{dF_k}{dE_{\bar{\nu}_e}} = \phi(E_{\bar{\nu}_e})\frac{I_k(t)}{L_k^2}(1 - \sin^2(2\theta_{12})\sin^2(\frac{1.27 \times \Delta m^2_{12} \times L_k}{E_{\bar{\nu}_e}})) \tag{C.3}$$

Let's denote $R \equiv \frac{1.27\Delta m^2_{12}}{E_{\bar{\nu}_e}}$. Then

$$\frac{dF_k}{dE_{\bar{\nu}_e}} = \phi(E_{\bar{\nu}_e})\frac{I_k(t)}{L_k^2}(1 - \sin^2(2\theta_{12})\sin^2(R \times L_k)) \tag{C.4}$$

and the sum:

$$\frac{dF}{dE_{\bar{\nu}_e}} = \phi(E_{\bar{\nu}_e}) \sum_k \frac{I_k(t)}{L_k^2}(1 - \sin^2(2\theta)\sin^2(R \times L_k)) \tag{C.5}$$

(Note how $\phi(E_{\bar{\nu}_e})$ factors out; 4D $\rightarrow$ 3D)
The "oscillation loss" term has the form

$$\sin^2(2\theta_{12}) \sum_k \frac{I_k(t)}{L_k^2} \sin^2(R \times L_k) \tag{C.6}$$

(Now the $\sin^2(2\theta_{12})$ factors out from the sum, same as in Method A; 3D $\rightarrow$ 2D).To calculate the detectable differential flux for given time (or corresponding run number),

$E_{\bar{\nu}_e}$ and oscillation parameters one has to evaluate the non-oscillated differential flux:

$$F_{no-osc}(t, E_{\bar{\nu}_e}) = \phi(E_{\bar{\nu}_e}) \sum_k \frac{I_k(t)}{L_k^2} \tag{C.7}$$

then the maximum oscillation losses:

$$F_{max-osc-loss}(t, E_{\bar{\nu}_e}, \Delta m_{12}^2) = \phi(E_{\bar{\nu}_e}) \sum_k \frac{I_k(t)}{L_k^2} \sin^2(R \times L_k) \tag{C.8}$$

then multiply $F_{max-osc-loss}$ by $\sin^2(2\theta_{12})$ and subtract from F_{no-osc}

There is no need to recalculate the sums during the run time. The first one is a constant for a given time and is pre-calculated into a 1D array indexed by time (or run number). Dropping out $\phi(E_{\bar{\nu}_e})$ and forming the indexed tables out of continuous functions, we have:

$$FluxNoOscillation[i] = \sum_k \frac{I_k(t[i])}{L_k^2} \tag{C.9}$$

Similarly, the second sum can be precalculated into a 2D table, the first index being the same as for the non-oscillated sum and the second corresponding to different values of ratio R:

$$FluxLossToOscillation[i][j] = \sum_k \frac{I_k(t[i])}{L_k^2} \sin^2(R[j] \times L_k) \tag{C.10}$$

The multiplication by $\phi(E_{\bar{\nu}_e})$ can be performed in the last place.

Since the biggest table is now only two-dimensional, one can fill it in rather fine bins (e.g. several thousand values of R) without overwhelming the memory of a common PC.

Things get worse if we consider individual spectra for every reactor. In this case, $\phi(E_{\bar{\nu}_e})I_k(t)$ turns into $\Phi_k(E_{\bar{\nu}_e}, t)$ and the whole method breaks. As soon as a non-trivial dependence on both reactor index and energy is introduced into the sum, the ratio R alone isn't enough to describe the oscillation pattern anymore. We end up with a 3D table again.

However the description in terms of $\Phi_k(E_{\bar{\nu}_e}, t)$ is unnecessarily general. Physically, the reactor antineutrino spectra are linear combinations of 7 fixed spectra: $\bar{\nu}_e$ produced by fissions of ^{238}U, ^{235}U, ^{239}Pu and ^{241}Pu, respectively.

Instead of having only one spectrum and only one "neutrino brightness" as a function of time and reactor number, we now have seven of them but we can still handle them separately and sum up the isotope components at the last stage only. Instead of one 1D table for non-oscillated intensity and one 2D table for maximum oscillation losses, plus one 1D array for the "common spectrum" we now have seven of each. Besides, we have to cope with some speed loss to the summation over the

7 isotope components but the advantage in memory efficiency and/or in accuracy achievable with the same amount of memory is still decisive.

The suggested implementation for the Method B is as follows.

As in Method A, there are two separate phases: first "compilation" (i.e. preparation of the tables from the reactor data), second – actual parameter fit or scatter plot using the pre-calculated tables.

During the "compilation" phase, the integral non-oscillated $\bar{\nu}_e$ flux is evaluated for every run by summing up the corresponding inputs from individual reactors. The process is repeated for every isotope separately (for KamLAND calculations, seven isotopes, 4 fissions and 3 long-lived decays). This way four 1D tables are produced. The 2D "maximum oscillation loss" tables are indexed in terms of run number and oscillation length ratio R as described above. The values in these 2D tables don't have a transparent physical meaning and should be understood as "the expected maximum deficit in the spectral bin, **absolute** in terms of overall non-oscillated flux from the current isotope but **relative** to the occupancy of this bin according to the unity-normalized non-oscillated isotope's spectrum". And "maximum" simply means "for $\sin^2 2\theta_{12} = 1$". Seven 2D "maximum oscillation loss" tables are filled and dumped into a file along with the four "non-oscillated" tables.

The "parameter fit" phase for this method needs also 7 raw antineutrino spectra for the main fission isotopes but this information has nothing to do with the reactor data; it can be generated once and read separately from the reactor information "compiled" file.

To recover the expected differential oscillated flux for given run number, Δm^2_{12}, $\sin^2 2\theta_{12}$ and $E_{\bar{\nu}_e}$, one does the following:

- evaluate the oscillation length ratio R from Δm^2_{12} and $E_{\bar{\nu}_e}$
- look up the values corresponding to the run from the "non-oscillated" tables for all 7 isotope components
- look up the values corresponding to the run and calculated R from the "maximum oscillation loss tables" for all 7 isotope components
- multiply the latter by $\sin^2 2\theta_{12}$ for all 7 isotope components
- subtract the results from the corresponding non-oscillated values
- multiply the resulting isotope intensities by the the factors looked up from the corresponding spectra according to the chosen $E_{\bar{\nu}_e}$ (note that $E_{\bar{\nu}_e}$ is used twice, first to calculate R, then here)
- finally add the 7 isotope components together

Lengthy as it appears, the procedure can be written in an efficient way, since most of the operations here are simple ones like loads, additions, subtractions and multiplications.

Vita

Mikhail Batygov was born on June 1, 1969 in Moscow, USSR. From 1986 to 1992 he attended the Moscow Engineering Physics Institute which he graduated from with a M.S. degree in Applied Mathematical Physics. He worked as an engineer in the General Physics Institute of Russian Academy of Sciences in 1992-1993 and in the All Union Institute for Nuclear Power Plant Operations (VNIIAES) in 1993-1994. From 1994 till 1999 he worked as a junior researcher at the Nuclear Physics Institute of the Moscow State University. In 1999 he entered the University of Tennessee as a doctoral graduate student in Elementary Particle Physics. He completed his Doctor of Philosophy degree in 2006.